Extreme Microgap Based Hotspot Thermal Management with Convective Boiling of Refrigerant

A Thesis

Presented to

The Academic Faculty

By

Mohamed Nasr

In Partial fulfillment

of the Requirements for the Degree

Master of Science in the school of

Mechanical Engineering

Georgia Institute of Technology

August 2016

Extreme Microgap Based Hotspot Thermal Management with Convective Boiling of Refrigerant

Approved by:

Dr. Andrei Fedorov, Advisor

School of Mechanical Engineering

Georgia Institute of Technology

Dr. Yogendra Joshi

School of Mechanical Engineering

Georgia Institute of Technology

Dr. Peter Kottke

School of Mechanical Engineering

Georgia Institute of Technology

Date Approved: May 31,2016

To my loving mom (first and foremost), dad, and baby (not anymore) brother.

Acknowledgments

I wish to thank my advisor Dr. Andrei Fedorov for a great educational experience and his guidance throughout this program. His enthusiasm and passion for research are inspiring and have constantly been a source of motivation. I also wish to thank Dr. Peter Kottke and Dr.Craig Green for their mentorship and contribution to a great research dynamic. I hope to work with this incredible team once more for a PhD.

I wish to thank Dr. Yogendra Joshi for his guidance and role as a member of my committee. I would also like to thank all members of the DARPA IceCool Fundamentals team in Georgia Tech including Dr. Suresh Sitaraman and Dr. Muhannad Bakir. I am very grateful to Dr. Bakir's research group for their outstanding fabrication work and Dr. Sitaraman's group for mechanical reliability support. It was a great pleasure to collaborate and work with all students involved in this project.

I would like to thank the MITf lab group for friendship and support in research and classes. Special thanks to Jungyun lee and Mason Chilmonczyk for helping me push through my courses and Jeff Fisher for helping me learn COMSOL.

Table of Contents

List of Tables

List of Figures

Page

Summary

Performance of the next generation microprocessors is rapidly reaching its limits due to inability to remove heat, especially at high power density from so-called local "hotspots". Convective boiling heat transfer in microgap heat sinks has the potential to dissipate ultra-high heat fluxes. This thesis presents an experimental investigation of heat transfer performance of three dedicated microgap coolers for hotspot thermal management. In this study, a rectangular microgap, batch micromachined in silicon and instrumented with thin-film resistive thermometry, is employed to assess its capability of dissipating extreme heat fluxes of multiple kW/cm^2 while keeping the wall temperature within the limits dictated by electronics reliability. Convective boiling in microgap with heights of 5 μm and 10 μm was tested with and without pin fins in the microgap. The test section was heated from the bottom using resistive heaters and capped with glass to enable visual observation of two-phase flow regimes. Microgap pressure drop and wall temperature measurements, mapped into flow regimes, were obtained with R134a as the coolant, for heat fluxes up to 5 kW/cm^2, mass fluxes up to 7,000 kg/m^2s, at maximum pressures up to 1.5 MPa and outlet vapor qualities approaching unity. These experimental parameters constitute extreme values in terms of microgap height (smallest reported to our knowledge), mass fluxes, and heat fluxes. New flow regimes, including vapor plumes, liquid slugs, and ultra-thin wavy liquid film, were observed as a function of increasing heat flux and microgap geometry. Dominant mechanism(s) of two-phase heat transfer responsible for each regime have been postulated based on flow visualization correlated with pressure drop and thermal resistance measurements. A 3D numerical model was used to extract two-phase heat transfer coefficient and quality from experimental data and the results were compared to correlations found in literature.

Chapter 1

Introduction

An experimental investigation of heat transfer performance of three dedicated microgap coolers for hotspot thermal management is presented in this work. The microgap coolers presented utilize two phase convective boiling of refrigerant to dissipate ultra-high heat fluxes targeted for high power density computing application. Experimental parameters investigated constitute extreme values in terms of microgap height, mass fluxes, and heat fluxes. Boiling flow regimes are presented along with dominant mechanism(s) of two-phase heat transfer responsible for each regime.

1.1 Purpose and Motivation

Increases in microprocessor power density have created a demand for new cooling techniques capable of dissipating high heat fluxes. Local sites of ultra-high heat generation (>1 kW/cm^2) known as hotspots limit microprocessor performance and reliability due to the excessively high temperatures they generate, which locally drive the microprocessor above its temperature limits [1].

Single phase cooling has been conventionally used for microprocessor thermal management in the past, utilizing coolant flow over an externally attached heat sink to remove heat. Advancement in fabrication processes have allowed for practical consideration of microgap and microchannel coolant flow on the back side of an active electronic component thereby removing the need for thermal interface materials (TIMs) [2]. Still, studies of single phase forced convective cooling have been limited to dissipating heat fluxes up to $790W/cm^2$ [3-5]which fall short of the high heat fluxes generated by hotspots (> $1000W/cm^2$).

Convective flow boiling is an attractive thermal solution for high heat flux removal with potential application for hotspot mitigation. Two-phase cooling offers the advantage of utilizing both latent and sensible heat absorption to remove heat. Adequate choice of coolant in terms of saturation temperature allows for high heat removal rates at uniform junction temperature below the operating limit of application. By eliminating the need for TIMs, significantly reducing device thermal resistance and exploiting high heat removal rates of convective boiling, two phase microgap heat sinks are a promising technology for hotspot thermal management.

1.2 Two Phase Convective Cooling

Two phase flow in microchannels is an area of active research with two primary fields: adiabatic studies, which emphasize hydrodynamic characteristics of two phase flow, and diabatic studies, which emphasize thermal characteristics of two-phase flow. Adiabatic studies aim to identify dominant flow regimes and develop prediction criteria for flow regime transitions, ignoring thermal interaction between the fluid and environment [4]. A flow regime describes the form that the liquid and vapor phase of a two-phase fluid takes as it travels along a closed channel. Ultimately, the goal of adiabatic studies is to generate flow pattern maps which can accurately predict flow regimes for a wide variety of channel geometry, operating conditions and fluids. Taitel and Dukler have pioneered this effort, identifying dominant flow regimes for a broad range of channel geometries and proposing physics based criteria for transition between regimes in terms of the Froude number, Martinelli number and T parameter, relating liquid pressure drop to buoyancy [6]. Although the work of Taitel and Duckler does not consider thermal interactions between fluid and environment, the Unified Model they developed has been useful in identifying transitions in thermal performance which are inherently linked to flow regime transitions [7].

Diabatic studies investigate the boiling mechanism of fluid flow in a channel from the perspective of thermal performance. In addition to developing flow pattern maps, diabatic studies aim to identify boiling heat transfer coefficient and characterize its dependence on void fraction and vapor quality for a range of operating conditions. The Critical Heat Flux (CHF) is another parameter of great importance to diabatic studies, referring to the heat flux at which a rapid degradation in thermal performance occurs. The degradation in thermal performance is marked by a sharp increase in wall temperature over which coolant flows with increases in applied heat flux and occurs as a continuous liquid layer wetting the microgap surface dries out. A two phase flow pattern map for evaporating flow presented by Thome et al is shown in Fig 1.1. The flow pattern maps categorized the boiling flow regimes in terms of mass flux and quality [8, 9].

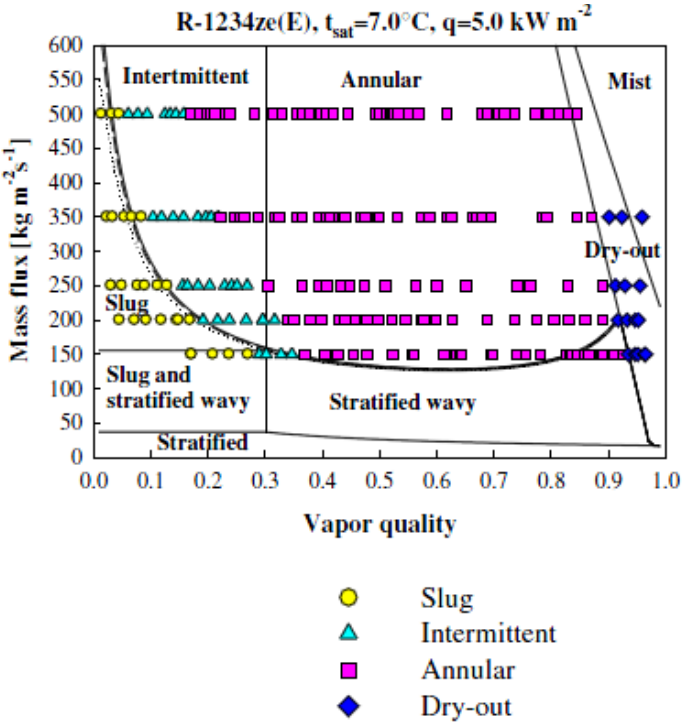

Figure 1.1 Flow Pattern Map for Evaporating Flow Produced from [9].

1.3 Two-Phase Microcooler Development

With the advancement of fabrication technology paving the path for microscale heat sink production there is a need to understand whether the boiling mechanism of previously studied minichannels can be applied in the microscale. Furthermore, the impact of fluidic communication distinguishing microchannel heat sinks from microgap heat sinks needs to be understood to assess the tradeoffs in using one versus the other. Finally, experimental characterization of the boiling process in two phase microcoolers is necessary to determine how to maximize heat dissipation.

1.3.1 Transition to Microscale Two Phase Heat sink

With new fabrication processes allowing development of microgap and microchannel heat sinks of hydraulic diameters <3mm, physical correlations developed for two phase flow in channels of larger diameter, referred to as minichannels, cannot be directly applied at the microscale [10].One main difference between minichannel studies and microchannel studies is the flow condition in the channel. Prior to the availability of advanced microfabrication processes, studies conducted on minichannels primarily investigated turbulent flow (Reynolds number greater than 2300) however microchannel flow for hydraulic diameter less than 200 μm usually falls within the laminar domain (Reynolds number below 2300)[10,11]. Some studies [10-13] propose a channel size classification to distinguish between the application of macroscale and microscale heat transfer models due to the difference in heat transfer theory governing the boiling process. Klandikar [12] recommends the following classification solely based on channel geometry, specifically hydraulic diameter: conventional (D_H>3mm), minichannel (200um<D_H<3mm), and microchannel (10 um<D_H<200um). Thome [11] claims

that geometry based classifications do not adequately capture the impact of channel size on the physical mechanism of boiling and proposes classification based on bubble growth to define the transition from macroscale to microscale heat transfer theory validity. The suggested transition to microscale boiling theory occurs when bubbles become confined by the channel and are forced to grow along the length of the channel rather than the bubble diameter. Others have tried to quantify the transition to microscale theory by defining dimensionless numbers such as the confinement number (Co), defined as the ratio of departing bubble diameter to channel diameter, and Bond number (Bo), relating gap depth to bubble diameter. Transition criteria suggested include $Co > 0.5$ [14] for deviation from conventional macroscale boiling theory and $Bo < 1$ [2] for transition from unconfined flow to confined flow.

Several studies have shown agreement that nucleate boiling is the dominant heat transfer mechanism controlling macroscale evaporation while forced convective boiling is the dominant heat transfer mechanism in microscale evaporation [13,15-17]. High heat removal rates characteristic of forced convective boiling at low flow rates make microscale heat sinks an attractive solution for high heat flux dissipation for high power density electronics.

1.3.2 Microgap Based Heat Sinks

Parallel microchannel heat sinks and microgap heat sinks are heavily researched solutions for thermal management in electronics. Microchannel heat sinks differ from microgap heat sinks in the use of multiple channels for coolant flow rather than a single channel. Microchannel heat sinks have an advantage of large surface area for heat rejection to coolant over microgap heat sinks. However, fluidic communication between channels in microchannel heat sinks makes them susceptible to undesirable flow instabilities including severe pressure oscillations and flow reversal within the channel [19-21]. Microgap heat sinks have shown more stable performance

and are less vulnerable to flow instabilities with lower amplitude wall temperature fluctuations and pressure oscillations [2, 6, 22]. Surface area enhanced microgap heat sinks have been studied as a means to increase heat rejection to the coolant.

Thermal performance of microgap heat sinks has been shown to improve with decreasing gap height as thin film convective boiling dominates the heat removal mechanism. Thin film which has been reported to have the largest boiling heat removal rates due to a low thermal resistance of the liquid film wetting the microgap surface [2,6,7]. Transition to thin film boiling in microgap heat sinks has been shown to occur with decreases in gap height due to increased bubble confinement [2]. Thermal performance of microgap heat sinks is also strongly linked to the flow boiling regime of the fluid. Other parameters such as quality, mass flux and heat flux have also been shown to play an important role in heat transfer performance [2, 4, 6, 7, 23-24].In the absence of proven first principles for two phase flow in microgaps, empirical correlations are generally used to predict heat transfer coefficient, CHF and pressure drop, often for a limited range of operating conditions that cannot be extrapolated to variations in geometry or coolant [24,25]. The heavy reliance on limited-range empirical correlations for predicting two-phase microgap heat sink performance is a major limitation in this field of study.

The primary flow regimes observed in two phase flow through miniature horizontal gaps are: bubble, intermittent, annular and stratified flow [6,7,23-24] and are depicted in Fig.1.2. Bubble flow refers to the flow of spherical vapor bubbles surrounded by liquid. Intermittent flow refers to flow of elongated vapor plugs, formed by the agglomeration of bubbles, surrounded by liquid. Annular flow refers to a thin liquid film which covers the top and bottom surfaces of the channel with a vapor core in between. Annular slow was shown to be the most prevalent flow regime in microgap heat sinks in several studies [2,4,6,7,24]. The stratified flow regime is only

observed in horizontal flow and refers to a stratification of liquid and vapor layers, with the vapor phase flowing on top of the liquid. Formulations used to predict flow regime transition are often linked to the characteristic driving force of the two phase flow. In the bubbly and intermittent flow regimes, surface tension was found to be the dominant driving force. In the annular and stratified flow regimes, shear stress at the vapor-liquid interphase was found to be the main driving force [6,7]. The high heat removal rates achieved in convective thin film boiling regimes such as annular flow are known to occur due to a low thermal resistance of liquid film and acceleration in the film velocity by the vapor phase through shear stresses at the interface.

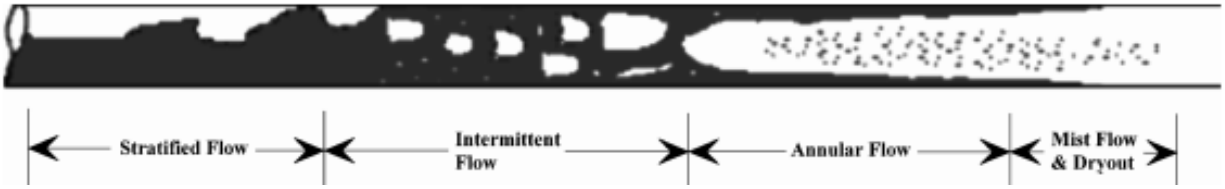

Figure 1.2 Two phase boiling flow regimes in a horizontal tube. The boiling process starts in the stratified flow regime and transitions to intermittent, annular and mist flow with increases in heat flux. Produced from [7].

The high heat removal rates achieved via convective thin film boiling in annular flow have motivated studies of shear driven thin film boiling in microgap heat sinks to better understand thermofluid behavior of ultra-thin liquid films [26-28]. The ultra-thin film boiling regime is similar to the stratified flow regime in the stratification of liquid and vapor layers, however the liquid layer is on the order of micron or sub-micron scale thickness and occurs at the highest heat fluxes close to CHF/dryout. This is a shear driven flow regime where instabilities such as thermocapillary (Marnagoni) effect and Kelvin-Helmholtz contribute to formation of wave perturbations across the liquid film [26-28]. Shear driven thin film boiling has

shown stable performance in horizontal microgap heat sink with ability to dissipate heat fluxes up to 200W/cm^2 [27].

Bar Cohen et al [6,7,24] have described a trend of two-phase heat coefficient over a broad range of quality going from subcooled boiling and approaching unity for two phase microgap heat sinks. The M-shaped trend shown in Fig 1.3 contains inflection points corresponding to flow regime transitions and reflects thermophysical phenomena of two phase flow in microgaps. The initial increase in heat transfer coefficient in the subcooled domain corresponds to an acceleration of two phase flow with onset of nucleate boiling. Bubble agglomeration limits increases in heat removal rates and transition to the intermittent flow regime leads to a reduction in heat transfer performance due to periodic wall dryout from vapor slugs. At moderate qualities (15-40%), the transition to annular flow leads to an increase in heat transfer coefficient as thin film convective boiling dominates the heat transfer mechanism. Heat transfer performance reaches a maximum at high qualities (50-75%) as the liquid layer in annular flow thins and is followed by a decline in heat transfer coefficient as liquid dries out and flow is primarily in vapor phase.

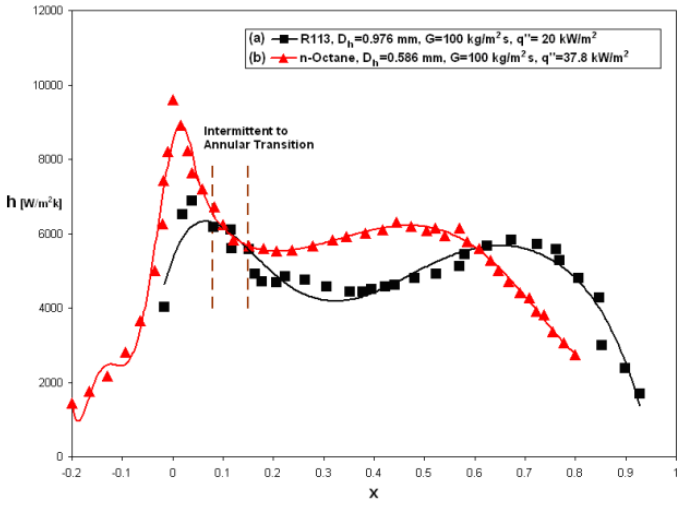

Figure 1.3 Characteristic heat transfer coefficient curve in microgap channel [23].

1.4 Current Methods

In this study, the thermal performances of three microfabricated extreme-microgap coolers for hotspot mitigation are characterized in terms of thermal resistance and pressure drop behavior for varying heat and mass fluxes. The devices tested have gap heights of 5 and 10 μm without and with inline cylindrical micro-pin-fin test section. Heat fluxes up to 5 kW/cm^2 and mass fluxes up to 7,000 kg/m^{2}s are investigated and constitute record high parameters never before observed in literature.

Part of the challenge in quantitative performance characterization of microgaps with small heated footprint is the difficulty in measuring heat losses, as the power input to achieve record high heat fluxes is quite small (<3W), while the domain for conduction spreading in the device is large with respect to the device dimensions. These challenges make it difficult to accurately estimate wall temperatures and quantify heat transfer coefficient, quality, and void fraction; therefore the results are reported in terms of overall thermal resistance based on relevant junction and ambient temperatures, which is a meaningful metric for electronics thermal management applications. A finite element model is developed to estimate quality and two phase heat transfer coefficient in the microgap to provide comprehensive thermal characterization.

Chapter 2 presents the microgap devices that are experimentally investigated and microfabrication processes used to create them. Experimental setup, procedures, and uncertainties are also discussed. Chapter 3 presents the experimental results including behavior of thermal resistance and pressure drop as a function of heat flux for several mass fluxes along with flow visualization and interpretation of dominant boiling regimes. In Chapter 4, limitations in experimentally quantifying heat losses and two phase heat transfer coefficient are discussed. A finite element model built to iteratively obtain two-phase heat transfer coefficient for two

generations of experimentally tested devices is presented. Chapter 5 presents modeling results in terms of two phase heat transfer coefficient trends as a function of heater heat flux and quality. Additionally, flow pattern maps and model validation are presented. Chapter 6 concludes this investigation with a summary of key results and outlines future work.

Chapter 2

Device Overview & Experimental Approach

This chapter is dedicated to presenting the three hotspot mitigation microgap based heat sinks investigated in this work along with the experimental setup and procedure used for thermal characterization. The first device tested, 'Gen 1', contains the smallest gap height of tested heat sinks comprising the most extreme geometry tested, although simplest in terms of features. The second device, 'Gen 2', consists of a microgap test section twice as tall as 'Gen1' device with added features for pressure measurement and heater isolation. The final device tested, 'Gen 3' is identical to the Gen 2 device with the addition of inline cylindrical pin fins to increase heat rejection to the coolant by surface area enhancement. The experimental setup built to perform thermal characterization of these microcooler devices is presented along with test procedures and measurement uncertainty.

2.1 Device Overview

The first device tested, 'Gen 1', contains a bare microgap without pin fins and is shown in Fig 2.1 with inlet and outlet ports that are 200 μm in diameter. Subcooled fluid enters the device through the inlet port and flows through the inlet plenum, which is 50 μm deep to minimize parasitic pressure drops at the fluid entry/exit domains. The microgap test section is 300 μm long x 200 μm wide x 5 μm high and is located in the middle of the device with three platinum resistance heaters deposited on the back side. The heaters generate a controlled heat flux which boils the coolant flowing over the microgap surface and also serve as resistance temperature detectors (RTDs) for temperature measurement. A 2 μm SiO_2 passivation layer is deposited on the heaters to protect against metal oxidation and to reduce heat losses to the

environment through the bottom surface. Pyrex glass seals the top side of the microgap and allows for flow visualization.

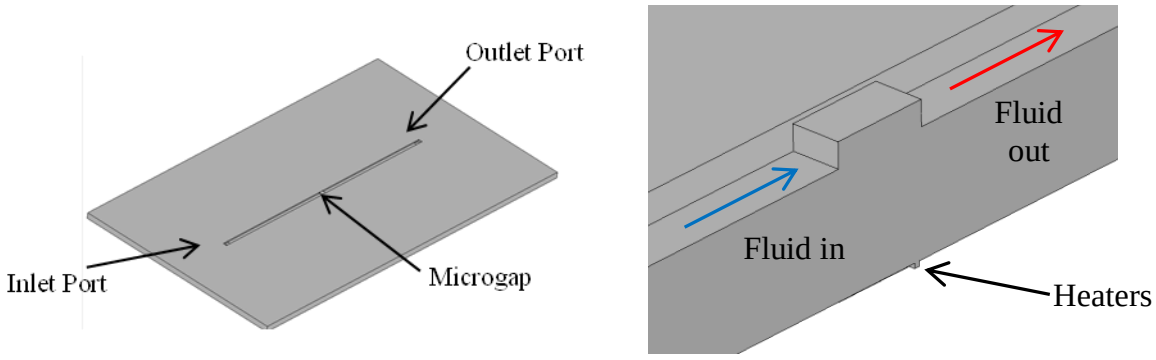

(a) (b)

Fig. 2.1 Gen 1 Device (a) Panoramic view (b) Cross section view at microgap.

The second device, 'Gen 2', is also an empty microgap device similar to Gen 1 and is shown in Fig. 2.2-b. The microgap footprint is the same, but gap height is now doubled to 10 μm. In addition, the Gen 2 device includes air trenches to reduce conduction heat spreading in the bulk silicon. The air trenches are 40 μm wide and 180 μm tall. The Gen 2 device also includes three RTDs on each side of the heater (six total) that are located orthogonal to the coolant flow direction solely for measurement of temperature distribution across the silicon in the vicinity of the heater as shown in Fig 2.3. The RTDS are 80 μm wide and 55 μm long with ~17.5 μm spacing.

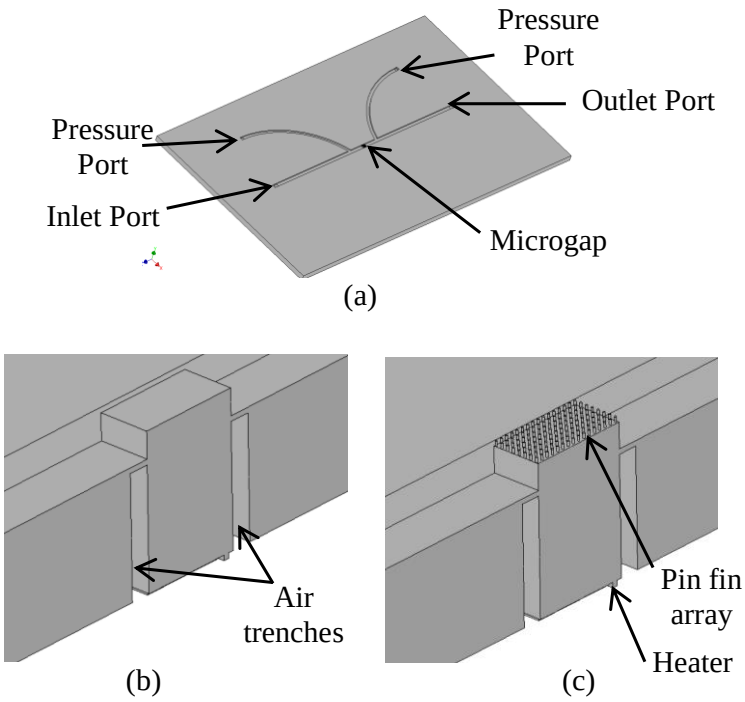

Fig. 2.2 Gen 2 and Gen 3 Devices: (a) Panoramic view; (b) Gen 2 cross section view; (c) Gen 3 cross section view.

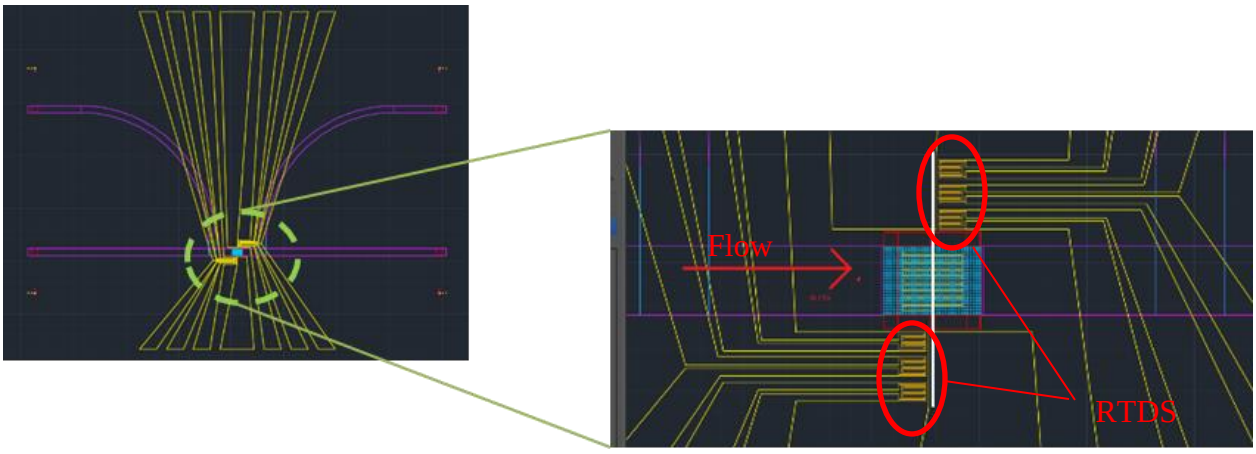

Fig 2.3 CAD drawing showing RTD locations in Gen 2 and Gen 3 devices.

The third device characterized, 'Gen 3', contains the same features as the 'Gen 2 Device' with the addition of inline cylindrical pin fins in the 10 μm high microgap that are 4 μm in

diameter and 10 μm apart. A cross sectional view of the Gen 3 device is shown in Fig. 2.2-c and SEM images of the pin fins and heater are shown in Fig. 2.4. The Gen 3 device contains identical air trenches and heater configuration as the Gen 2 device. Gen 2 and Gen 3 devices employ a single heater protected by 1 μm SiO_2 passivation layer on top. Device features, including air trenches and an array of pin fins are microfabricated using the same Bosch process that was used to create Gen 1 devices.

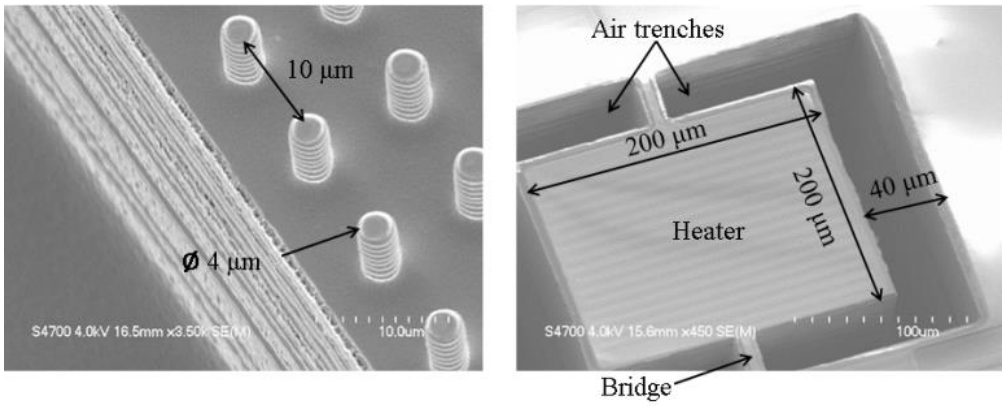

Fig.2.4 Gen 3 Device SEM Images: (a) Inline pin fins within a microgap; (b) Resistance heater on back side of device (identical in Gen 2 and Gen 3), also showing the air-gap isolation to minimize heat spreading between the heater and an actively-cooled microgap

2.2 Device Fabrication

The inlet and outlet ports, plenums as well as the microgap for Gen 1, Gen2 and Gen3 devices are etched in silicon using Bosch process with high precision and accuracy afforded by batch microfabrication. A schematic of the fabrication of Gen3 Devices is shown in Fig 2.5. The general process flow is similar for all microcooler devices with some additional steps for Gen 2

and Gen 3 devices to produce the pressure port, air trench and fin features not included in Gen 1 device.

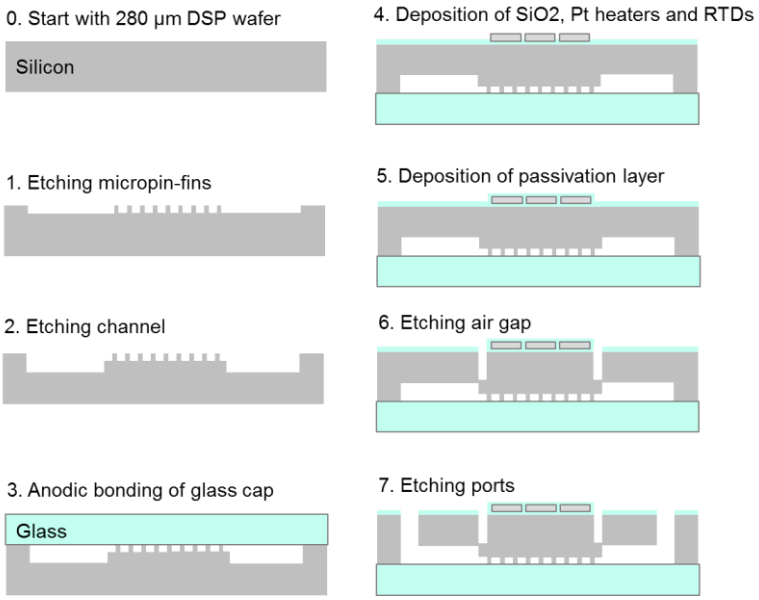

Fig 2.5 Gen 3 Microfabrication Process Flow [29]

The microfabrication process starts with a 280 μm thick double side polished Si wafer. The microgap is created first using Bosch process, which is a technique that alternates etching and deposition cycles to produce high aspect ratio features [30]. SF_6 gas was used for etching and C_4F_8 gas was used for passivation. Gen 1 device microgaps are 5 μm tall, while Gen 2 and Gen3 micrgaps are 10 um tall, all with a tolerance of ±0.5 μm. Note that in Gen 3 devices the micropinfins are created in conjunction to the microgap in this first step.

The next step utilizes the Bosch process to etch the 50 μm (± 3 μm) depth inlet and outlet plenums. The microgap was then sealed with 700 μm thick Pyrex glass using anodic bonding under a voltage of 800 V at 350 ^{o}C. A 2 μm thick insulating silicon dioxide layer was then deposited on the back side of the wafer using low pressure plasma enhanced chemical vapor

deposition (LP-PECVD). 200 nm (±5 nm) thick Platinum heater/RTDs and 500 nm (±10 nm) thick gold pads were then deposited on the SiO_2 layer. A second SiO_2 layer which is only 1 um thick was deposited on the heater/RTDs as a passivation layer again using LP-PECVD. The air trenches isolating the heater were then etched using Bosch process for Gen 2 and Gen 3 devices. Lastly, 200 μm diamter inlet and outlet ports, as well as pressure ports for Gen 2 and Gen3 devices were etched using Bosch process from the same side of the wafer.

2.3 Experimental Setup

The experimental setup used in this study is shown in Fig 2.6. The devices are housed in a machined PEEK package with O-ring seals for the inlet/ outlet ports and pressure taps (in the case of Gen 2 and Gen 3 devices) as shown in Fig 2.7. An Agilent 34970a data acquisition unit was used to record pressure drop, heater resistance, circuit current, inlet/outlet fluid temperatures and reservoir temperature for various flow rates across the devices. A KDS Scientific Legato 270 series syringe pump was used to drive refrigerant through the test section at a prescribed flow rate. Fluid temperature measurements were obtained with Omega K-type thermocouples. Pressure drop was measured with Omega PX 309 series pressure transducers which are connected to the pressure ports of the Gen 2 and Gen 3 devices shown in Fig 2.3. In Gen 1 devices, pressure transducers measure pressure at the inlet and outlet of the device since there are no pressure ports at the inlet and outlet of the microgap. Power was supplied to the device heaters with an Agilent E3641A power source. A fan cooled WBA series thermoelectric was used to condense vapor coming out of the test section. The reservoir tank was heated by electrical wire heaters with an Omega CN4000 PID controller to drive refrigerant into the system. A Keyence VH-Z100R microscope was used to obtain flow visualization images and

videos. Microscope flow visualization images show a top-down view of the microgap test section as shown in Fig 5.

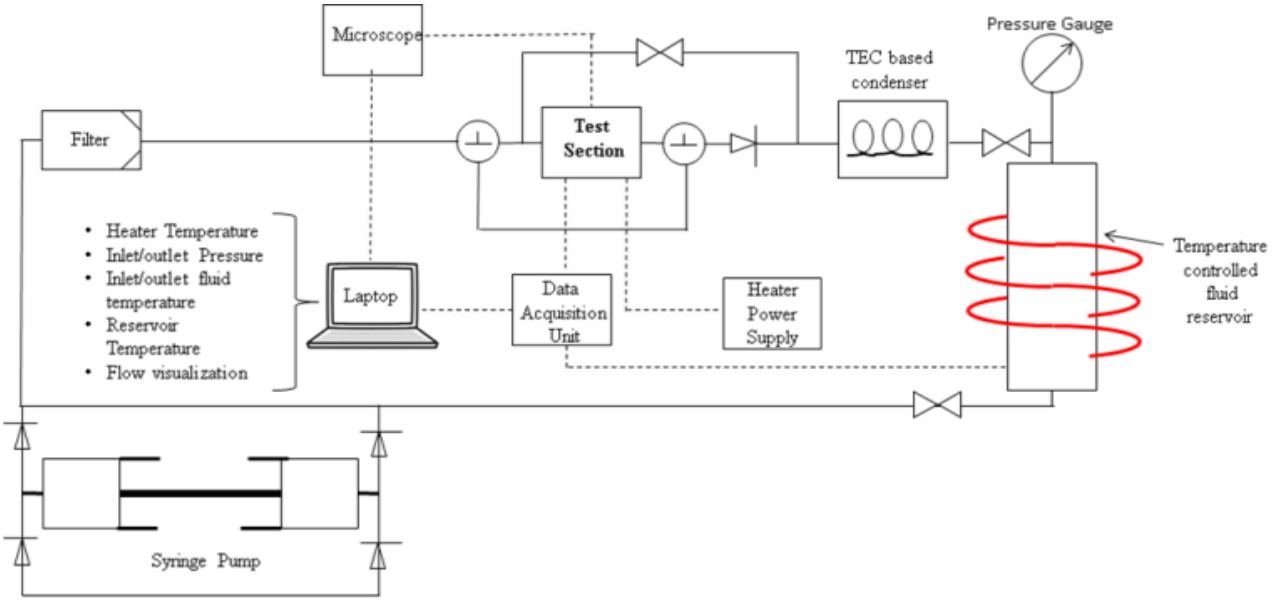

Fig 2.6 Experimental Setup Schematic

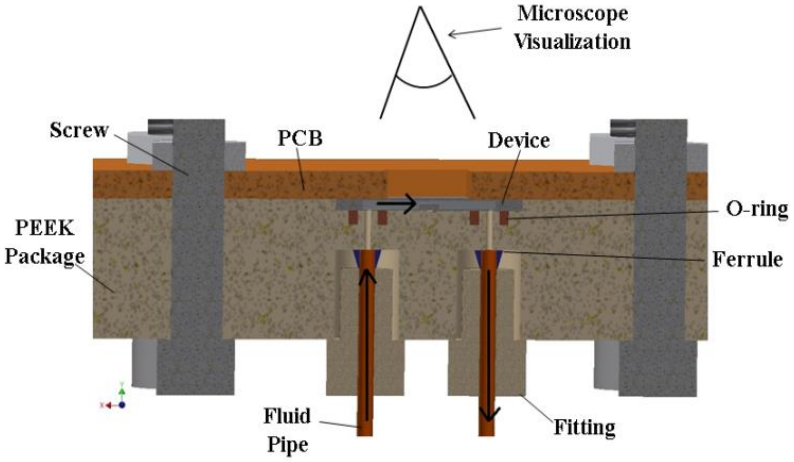

Fig 2.7 Cross Section View of Test Section and Hermetic Package. Flow visualization obtained from a top-down view of the microgap with microscope.

2.4 Experimental Procedure

Before starting experiments, device heaters are calibrated in a temperature controlled vacuum oven, showing excellent linear correlation between the RTD resistance and temperature. Experiments started by evacuating the experimental setup to remove most of residual air in the system and charging with R134a. The reservoir tank, containing refrigerant, was pressurized with wire heaters to ensure complete filling of the experimental loop with liquid. Mass fluxes between 1,000 and 7,000 kg/m^{2}s were tested by setting the syringe pump to the desired flow rate and subcooled R134a was delivered to the test device at 22.4°C inlet temperature for all experiments. Power was applied to the heaters in 0.1-0.25W increments until steady state temperatures and pressures were obtained. Flow visualization was performed by microscope with up to 700X lens magnification and continuous video capture with 0.067s time resolution. Power to the heaters was turned off when local dryout was observed in the microgap or when inlet pressure started to approach glass syringe limits to avoid catastrophic failure.

Note: Detailed procedures for preparing devices for experiments, evacuating the system, charging the system, running experiments and reliability protocol can be found in the Appendix.

2.5 Uncertainties

Error in K-type thermocouple used for heater calibration is +/-0.9°C, error in power applied to heaters from Agilent E3641A power source is +/-0.011W, error in mass flow rate from syringe pump is +/-0.01 mL/s, and error in pressure transducer measurements is +/- 8.62 kPa. Error in microgap height, air trench depth, and pin fin height is within +/- 5% of reported dimensions, and error in heater length and width is within +/- 1% of reported dimensions. Error propagation was applied to assess the uncertainty in mass flux, heat flux and thermal resistance which are found to be +/6.5%, +/- 1.5% and +/-1.7%, respectively.

Chapter 3

Experimental Results & Analysis

An experimental thermal characterization of Gen1, Gen 2 and Gen 3 devices is presented in this chapter. Trends in thermal resistance and pressure drop as a function of heater heat flux are reported for each microgap heat sink device with boiling regime transitions identified. Flow visualizations for dominant boiling regimes are presented in a top-down view with cross section schematic interpretation. The characteristic physical mechanism(s) of the boiling process and observed instabilities are postulated. Difficulty in experimentally quantifying heat transfer coefficient and quality in the extreme microgap geometry are also discussed.

3.1 Gen 1 Device

The average thermal resistance, calculated using Eq. 3.1, of the Gen 1 device as a function of heater heat flux for various mass fluxes is shown in Fig 3.1. Eq. 3. 1is given by,

$$R'' = \Delta T / q''_h \tag{3.1}$$

where R" is the overall device thermal resistance, which includes forced convective boiling of coolant and parallel path of conduction spreading through device silicon, with eventual heat rejection to the environment by radiation and free convection at exposed surfaces of the package. Relevant temperature difference ΔT is between heater/RTD surface and ambient air, and q''_h is the heat flux computed based on supplied power and the area occupied by the resistance heater (200 μm x 200 μm). Total device thermal resistance is used to present thermal performance rather than microgap convective thermal resistance because of the difficulty in quantifying heat flow into the microgap, which will be further discussed at the end of this section. The results on

each plot are grouped based on the dominant flow regime in the microgap from flow visualization. The observed flow regimes for the Gen 1 device are stratified, vapor slug, and ultra-thin liquid film (UTF) boiling. The flow visualization images show a top-down view of the microgap with flow going from left to right. Flow visualization images and cross-section schematic interpretation of the flow regimes are shown in Fig 3.2.

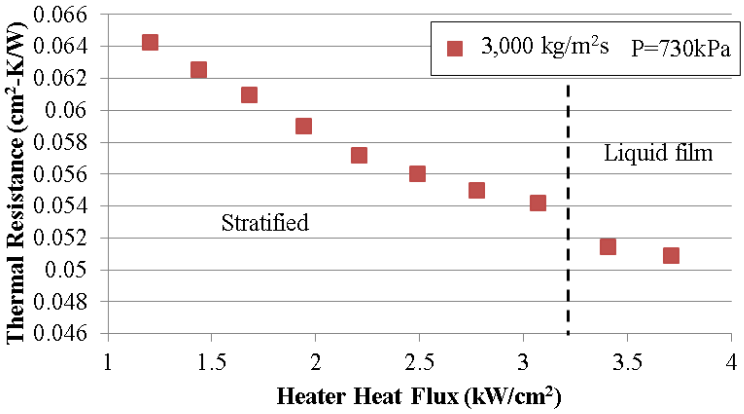

(a)

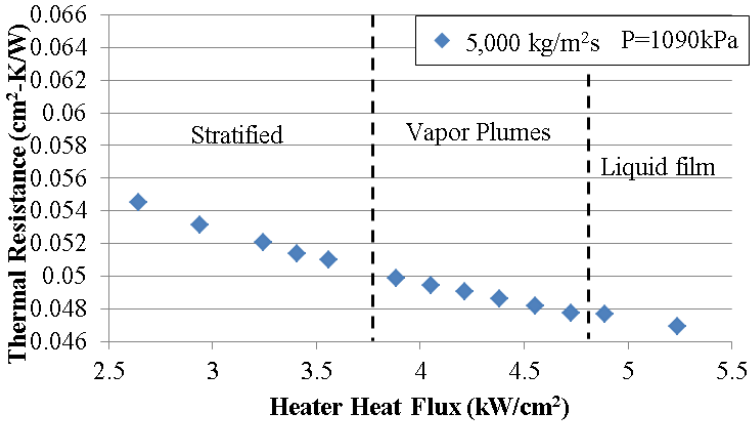

(b)

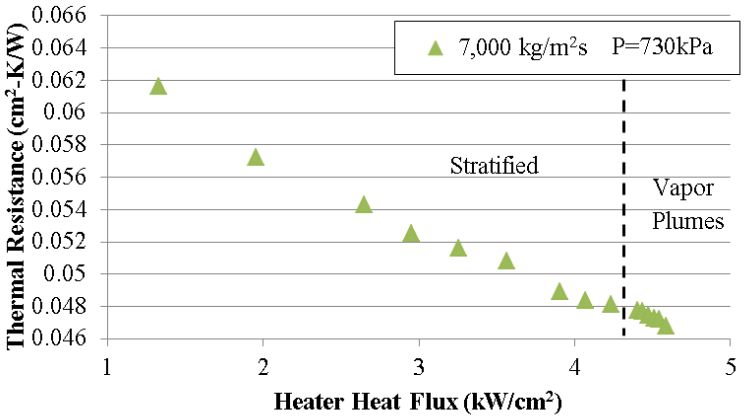

(c)

Fig. 3.1 Thermal Resistance vs Heat Flux for Gen1 Device: (a) G=3,000 kg/m^{2}s (b) G=5,000 kg/m^{2}s (c) G=7,000kg/m^{2}s, mapped into flow regimes described in Fig. 3.2.

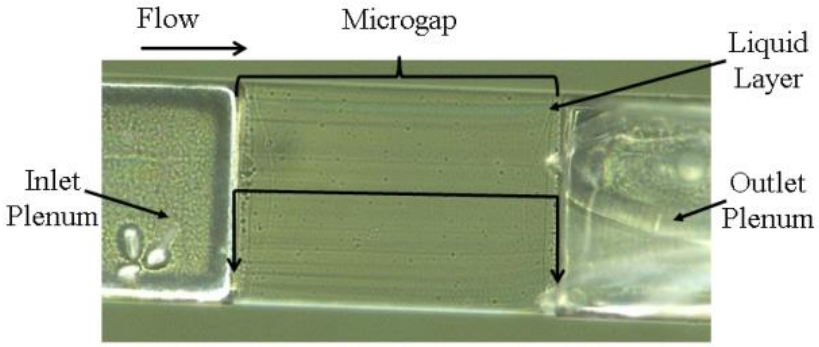

(a-1)

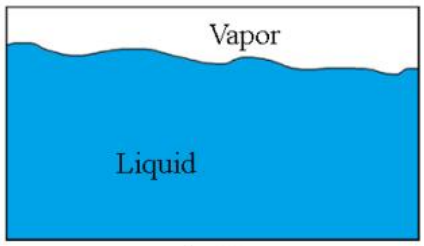

(a-2)

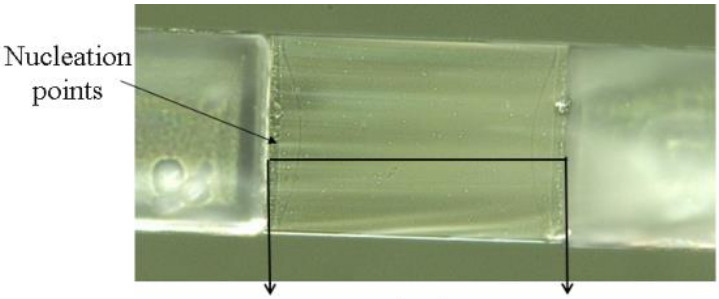

(b-1)

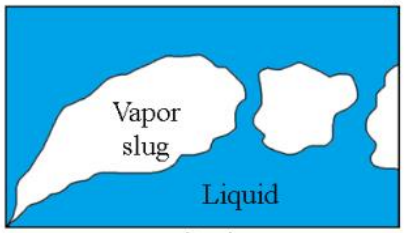

(b-2)

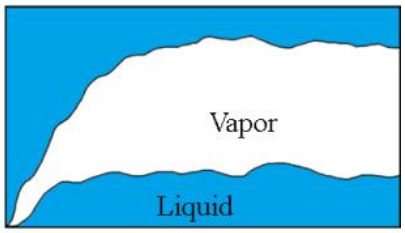

(b-3)

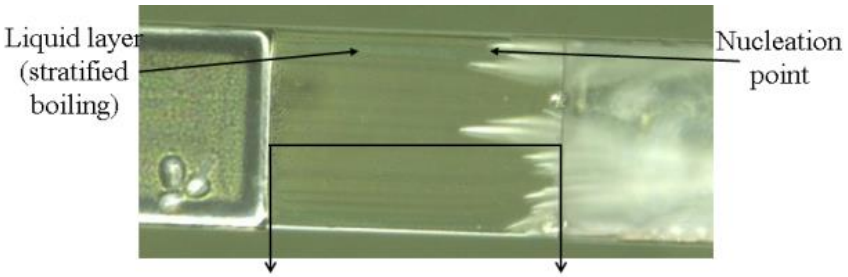

(c-1)

(c-2)

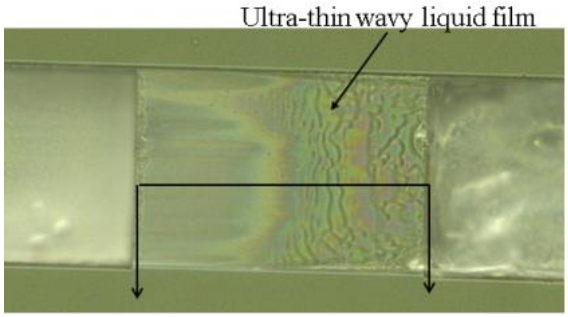

(d-1)

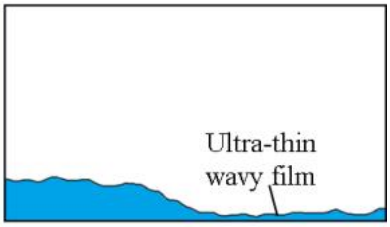

(d-2)

Fig. 3.2 Boiling Flow Regime Visualization in Gen 1 Device with Schematic Interpretation: (a) Stratified flow (b) Vapor slug flow at low mass fluxes (c) Vapor plume flow at high mass fluxes (d) Ultra-thin wavy liquid film flow.

The stratified flow regime shown in Fig. 3.2-a-1 was observed at the lowest heat fluxes and consists of a liquid layer on the bottom surface of the channel with a thin vapor layer above as illustrated in Fig 3.2-a-2. This stratified regime is consistently observed at low heat fluxes for all mass fluxes tested and is initiated at subcooled nucleation sites in the inlet plenum where vapor is formed and advected into the microgap by the liquid flow. The vapor plume flow regime shown in Fig 3.2-b and c forms at nucleation points and consists of elongated plumes or slugs that may either be large enough to span the entire microgap or be shorter in length than the microgap but moving so fast that they appear to span the entire microgap (imaging artifacts due to aliasing). Both possible scenarios are shown in the cross section illustrations, Fig 3.2-b-2 and 3.2-b-3. The latter interpretation is proposed because the vapor velocities for these experiments are on the order of 1000m/s for mass fluxes beyond 4,000 kg/m^2s, as the vapor density of R134a is 4.25 kg/m^3, while microscope frame rate is too low to capture vapor slug boundaries at that speed. The vapor plume flow regime was observed for middle to highest input heat fluxes tested. At mass fluxes up to 5,000 kg/m^2s, the stratified boiling domain transitions directly to UTF boiling regime with an increase in heat flux. Interestingly, if heat flux is incrementally reduced at the UTF boiling regime, vapor plume boiling becomes dominant as shown in Fig 3.2-b. This is an embodiment of boiling hysteresis where at a given heat flux boiling may either be in stratified regime or vapor slug regime depending on the sequence of incremental heat input. In contrast, the transition to vapor slug regime at the highest mass fluxes (> 6,000 kg/m^2s) occurs when nucleation points are observed near the outlet of the microgap as shown in Fig. 3.2-c. As input

heat flux is increased, these nucleation points increase in density and move closer to the microgap inlet until the vapor slug flow covers the entire microgap. The inlet conditions at the entry to microgap where liquid is subcooled corroborate the observation of a nucleation front that starts near the outlet of the microgap and moves towards the inlet with increasing heat flux. Single phase liquid entering the microgap is being heated until it reaches saturation temperature, at which point a nucleation front is observed. The extent of single phase flow in the microgap decreases as the heat flux is increased because the fluid reaches saturation temperature more rapidly; this manifests in gradual movement of the nucleation front upstream with an increase in applied heat flux. The difference in transition behavior is a result of the relative impact of an incremental increase in the applied heat flux. For the case of low mass fluxes, fluid within a microgap boils nearly instantaneously even at modest (single increment) increase in the heat flux thus moving the nucleation front from the exit to the inlet of the test section almost immediately and 'bypassing' the vapor plume regime.

The most intriguing flow regime observed for this device is ultra-thin film (UTF) boiling as shown in Fig 3.2-d. UTF boiling was observed at the highest input heat fluxes and consists of an ultra-thin wavy liquid layer with vapor above. The liquid film is thin enough to reflect light on the order of wavelength equal to its thickness causing an appearance of different colors in flow visualization. A pattern of changing colors in the thin wave region is dynamic and indicative of traveling liquid waves subjected to high velocity vapor flow on top of the layer. There appears to be a reflected color gradient that transition from yellowish/purple to green downstream from the transition point, suggesting a rapid rather than gradual thinning of the liquid layer forming an ultra-thin film with thickness on the order of 400-600 nm. There appears to be no local dryout in this flow regime as indicated by the continuous decrease in the thermal resistance for increased

heat fluxes (Fig. 3.1), whereas thermal resistance can be seen to approach a minimum and begin to increase in Gen 2 and 3 devices upon reaching local dryout (Fig. 3.7).

Gas assisted thin film evaporative cooling studies in miniature channels [26-28] showed physical behavior similar to the observed UTF boiling regime. The underlying driving forces that dominate gas assisted thin film flow dynamics are tangential stresses at the gas-liquid interface and thermocapillary effects resulting from surface temperature gradient along the gas liquid interface [28]. The thermocapillary effect makes heat and mass travel towards areas of high surface tension, which is a function of temperature. Friction between gas and liquid layers accelerates and stabilizes the thin liquid film [27], however thermocapillary effect plays a more significant role in causing wave perturbations [28]. These phenomena are in agreement with qualitative observations in Gen1 device. The liquid film velocity in UTF boiling regime is found to be larger than that of stratified boiling regime, suggesting that there is acceleration in liquid flow by the vapor and thereby enhanced heat transfer properties. The varying ultra-thin film thickness, or wave perturbations, observed as patterns of reflected colors in Fig 3.2-d are consistent with presence of thermocapillary surface waves at the vapor-liquid interface. In addition, the difference in velocity between vapor and liquid phase is expected to contribute to the tangential stresses at the phase interface which cause wave structure formation via pressure differential in fluid vortexes following the Kelvin-Helmholtz instability.

UTF boiling was reported by Ohadi and co-workers to be one of the most effective methods of high heat flux removal because of the unparalleled high heat transfer coefficients, low quantity of fluid required to wet surface, and small temperature rise of surface above saturation temperature of fluid [15]. Similarly, in our experiments thermal resistance plots as a function of heater heat flux in Fig 3.1 show steadily declining thermal resistance with increases

in heat flux suggesting improved heat removal performance. As mass flux was increased, flow regime transitions occurred at higher heat fluxes and thermal resistances decreased as expected with higher heat removal rates.

Thermal resistance trends did not show noticeable change at flow regime transitions because of significant conduction heat spreading that occurs in the Gen1 device, however the general trend of decreasing thermal resistance with increasing heat flux is consistent with observed transitions in boiling regimes of increasing vapor content in the absence of local dryout [2,6]. The 280 μm thick silicon base of the device, surrounding the small heated area of the hotspot, introduces an additional path for heat flow from the heater to the ambient bypassing microgap. The ability for heat flow to bypass the microgap by conduction through silicon does not allow for direct correlation of the thermal data (temperature and heat flux) obtained at the heaters and convective boiling in the microgap to be able to produce meaningful predictions of heat transfer coefficient for convective boiling. Likewise, estimates of quality cannot be performed as they require accurate knowledge of heat losses to compute heat input to the fluid. Void fractions also cannot be accurately estimated from flow visualization because the across-the-gap distribution of liquid and vapor in the microgap cross section is difficult to establish from top-down visualization, particularly with the high vapor velocities which appear as streaks shown in Fig 3.2-b and Fig 3.2-c. Due to a relatively large medium for conduction heat spreading and small heat input needed to achieve highest heater heat fluxes (<3W), traditional methods of experimentally estimating heat losses such as correlating heat losses to heater temperature are ineffective. Furthermore, use of energy balance for single phase flow to assess heat losses is not possible because of challenges in accurate measurements of the coolant temperature increase from inlet and outlet due to impossibility of bringing thermocouples in direct proximity of the

microgap inlet/outlet. Heat losses are reduced in the Gen 2 and Gen 3 devices by etching air trenches around the heaters to direct heat flow to the microgap, as shown in Fig 3.3b. However, there is still non-negligible heat spreading to the silicon bulk through the bridges holding the hotspot domain in place, as shown in Fig 2.4. With large uncertainty in heat loss estimates, quality and void fraction are not reported in this study.

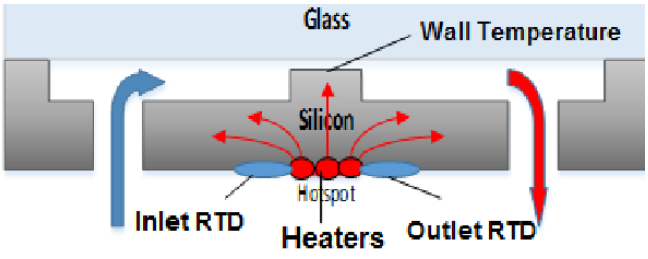

(a)

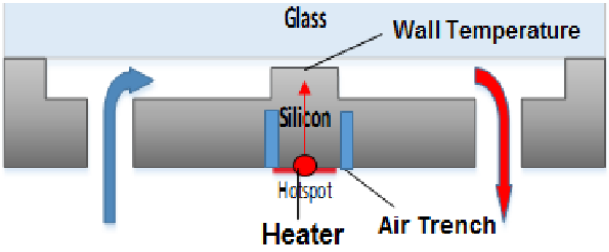

(b)

Fig. 3.3 Air trench isolation effect on conduction heat spreading: (a) Gen 1 device has no air trench and heat supplied at the bottom of the test structure is able to spread throughout silicon; (b) Gen 2 and 3 devices use an air trench to reduce heat conduction spreading and to direct a greater fraction of the heat supply to the microgap.

3.2 Gen 2 Device

Thermal resistance as a function of heat flux at the heater surface in the Gen 2 devices for various mass fluxes is shown in Fig. 3.4. Flow visualizations supplemented by illustrated interpretations of the boiling regimes for high and low mass fluxes are presented in Fig. 3.5 and 3.6, respectively. The dominant flow regimes from flow visualization are vapor plume, liquid slug, and liquid film boiling, which are mapped to domains that show change in trends of thermal resistance variation. The nucleation sites in the microgap inlet plenum that generated the stratified flow regime in Gen1 devices were not observed in Gen 2 devices. Nucleation in the inlet plenum prior to boiling in the microgap may have sensitivity to the surface features of the plenum as it was observed in some Gen1 and Gen 3 devices. Overall, nucleation in the inlet plenum has a negligible impact on thermal resistance of the device and pressure drop as the coolant is primarily in liquid phase. Vapor plume boiling in the Gen 2 devices takes the same form as that observed in the Gen 1 device; at low mass fluxes (<2000 kg/m^2s) boiling transitions from the outlet plenum directly to the inlet plenum with vapor slugs spanning the entire length of the microgap as shown in Fig 3.6-b. At high mass fluxes (≥2000 kg/m^2s) the nucleation points emerge near the outlet of the microgap and move in the direction opposing flow as heat flux is increased. The vapor plume forms a curved front because fluid in the microgap rejects heat to the side walls, which are expected to be at a lower temperature than the saturated fluid because the air trenches provide a significant thermal barrier for heat flow to the side walls as shown in Fig 2.4.

The decrease in single phase thermal resistance in Fig 3.4 is not due to particularities of the microgap flow, but an artifact of heat flow path through the device. Thermal resistance of the device was found to decrease in the absence of coolant at low heat fluxes up to 1.40 kW/cm^2 as the heat transfer by natural convection improved with an increase in the glass surface

temperature. Beyond 1.40 kW/cm^2 device thermal resistance remained constant as the resistance to heat transfer by convection at the glass surface was reduced to the level of being no longer dominant in the total thermal resistance of the device. Thus, at low heat fluxes single phase coolant flow thermal resistance is approximately constant as expected for fully developed flow, and the observed trend of decreasing total resistance is due to higher heat rejection rates through the glass surface. At higher heat fluxes, the transition from liquid to vapor plume regime caused thermal resistance to decrease with increases in vapor void fraction due to enhanced evaporation rate via thinning of the liquid layer on the heated surface of the microgap.

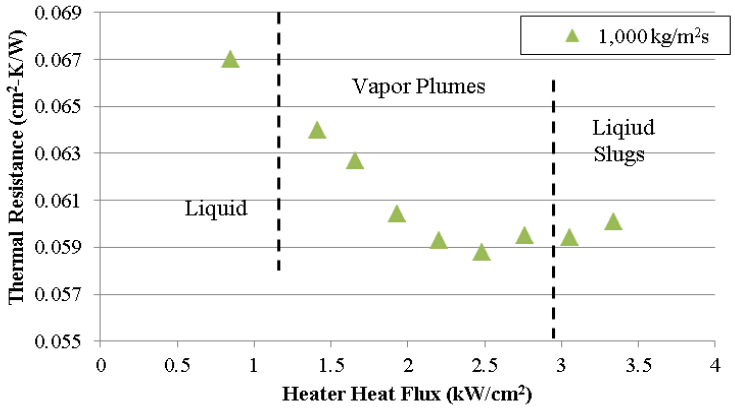

(a)

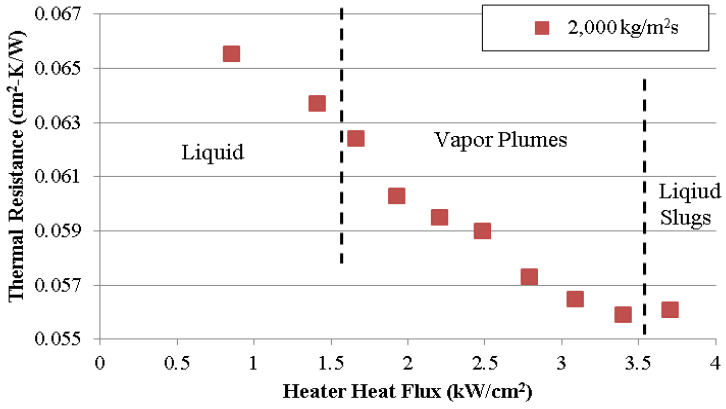

(b)

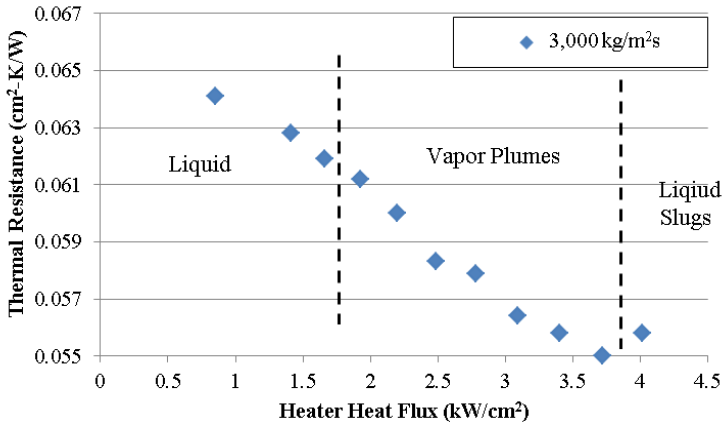

(c)

Fig. 3.4 Thermal Resistance vs applied heat flux for Gen 2 device: (a) G=1,000 kg/m^{2}s (b) G=2,000 kg/m^{2}s (c) G=3,000kg/m^{2}s, mapped into flow regimes described in Fig. 3.5.

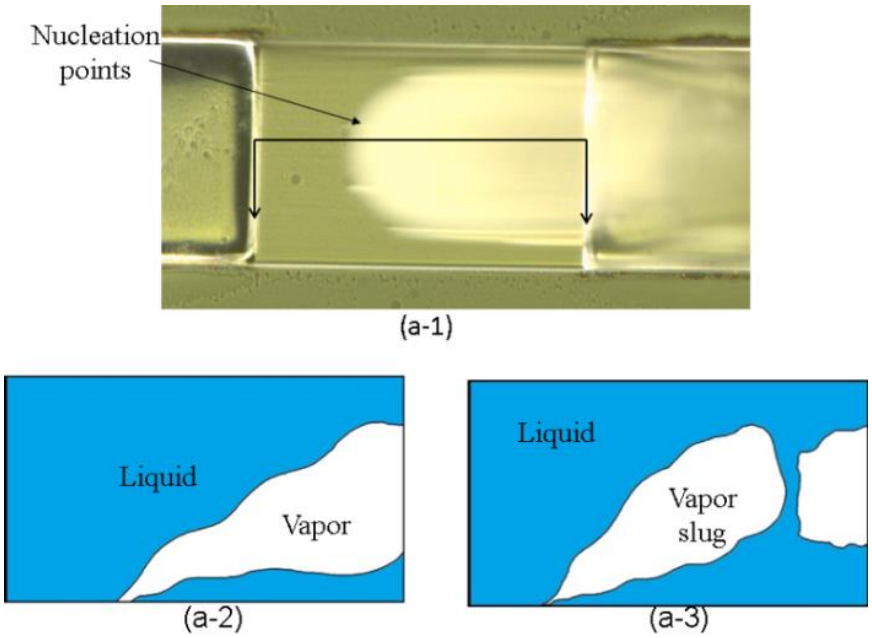

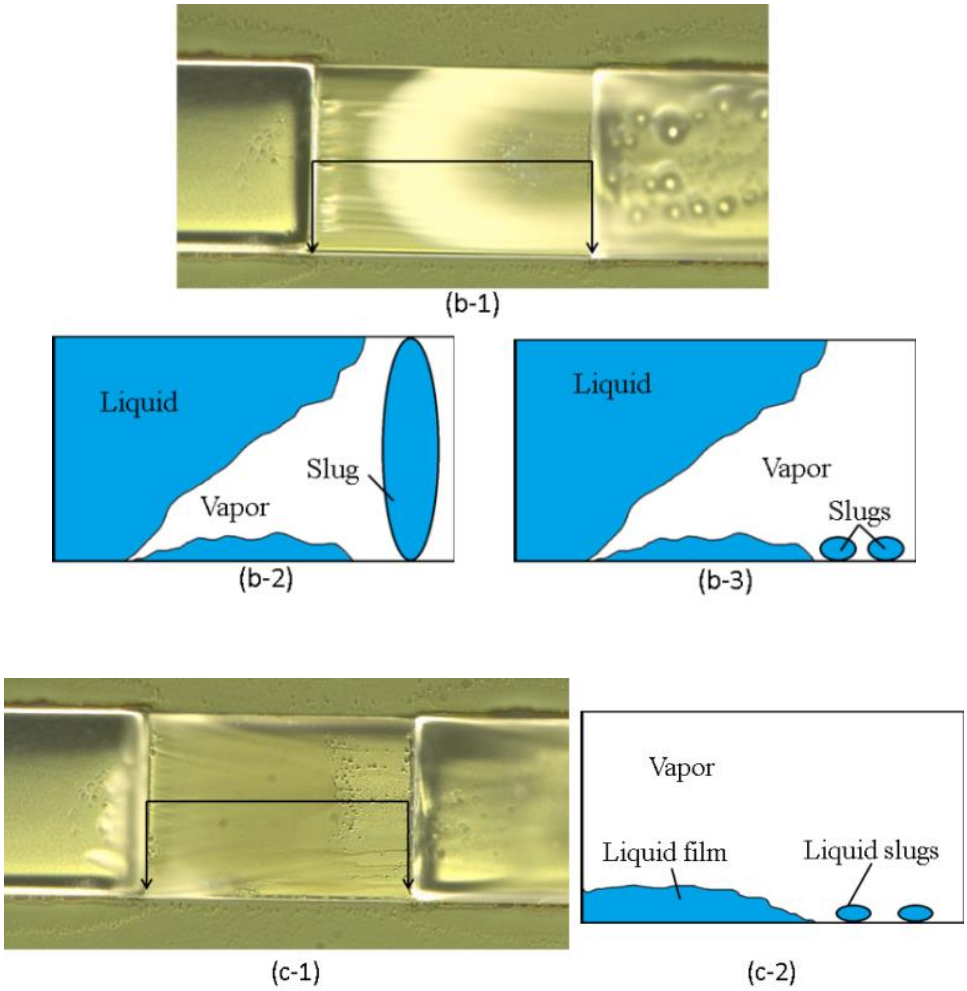

Fig. 3.5 Boiling Flow Visualization in Gen 2 Device at 3,000 kg/m2s with cross sectional schematics of flow regime interpretation: (a) Vapor plume flow; (b) Liquid slugs flow; (c) Liquid film flow

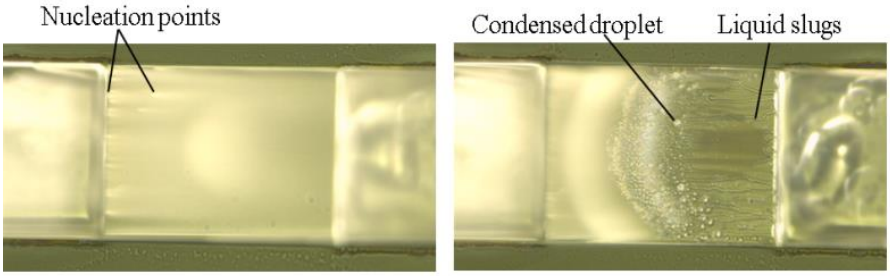

(a) (b)

Fig. 3.6 Boiling Flow Visualization in Gen 2 Device mass fluxes <3000 kg/m^{2}s, showing (a) vapor plume boiling spans the entire microgap as nucleation points emerge in the inlet plenum; (b) transition of vapor slug boiling directly to liquid slugs with condensation on glass surface is observed without an intermediate regime of thin film regime.

As heat flux is increased, the two-phase flow regime transitions to liquid slug boiling for low mass fluxes and liquid film boiling for high mass fluxes. At low mass fluxes the liquid layer beneath the vapor slugs gets thinner until the heated gap surface becomes partially dry and liquid slugs are pushed across as shown in Fig 3.6-b. Since the flow visualization images show a top-down view, the height of the slugs may be as tall as the gap height or smaller; both possibilities are illustrated in Fig 3.5-b-2 and 3.5-b-3. Furthermore, residual (condensed) liquid droplets appear on the glass surface supporting the interpretation that there was a liquid film on the glass side (top surface) of the microgap. At high mass fluxes, a thin liquid film was observed before it broke up into liquid slugs. Capillary cohesion forces are suspected to play the main role in keeping the film intact.

Heat transfer performance degraded at liquid slug/ film boiling as result of the local dryout. Thermal resistance reached a minimum value and gradually started to increase as shown in Fig 3.4. At this transition to local dryout, the device heater started to degrade and higher heat flux data was not collected to maintain an accurate heater calibration. The ability to detect transitions in thermal performance as a function of different boiling regimes suggests that the air trenches do limit conduction spreading in the bulk silicon as Fig. 3.3 suggests. Heat spreading through the heater bridges between the air trenches shown in Fig. 2.4 for Gen 2 and Gen 3 devices may still contribute significant losses due to the low power output of the heaters,

therefore quality and vapor fraction cannot be accurately estimated though energy balance calculations.

3.3 Gen 3 Device

Thermal resistance as a function of heater heat flux for Gen 3 devices at various mass fluxes is presented in Fig 3.7. The dominant boiling regimes follow those of Gen 2 devices and include vapor plume boiling and liquid slug boiling. Representative flow visualization images of these boiling regimes are presented in Fig. 3.8. The illustrated interpretations are similar to those shown for the same regimes observed in the Gen 2 devices. No differences in flow regime transition or behavior between low and high mass fluxes were observed in the Gen 3 device, likely because of the presence of fins which disrupt the flow patterns and homogenize the flow structure regardless of the magnitude of mass flux. Vapor slugs and liquid slugs appear in a parabolic pattern with more boiling near the side walls and less in the middle of the microgap, differing from Gen 2 devices which showed more boiling in the center. Increased hydrodynamic resistance near the side walls resulting from tighter spacing of the pin fins results in locally lower flow rates at the side wall and therefore more boiling. It is difficult to assess whether a liquid film regime exists at high mass fluxes due to the small spacing between the fins, which prevents detailed optical visualization.

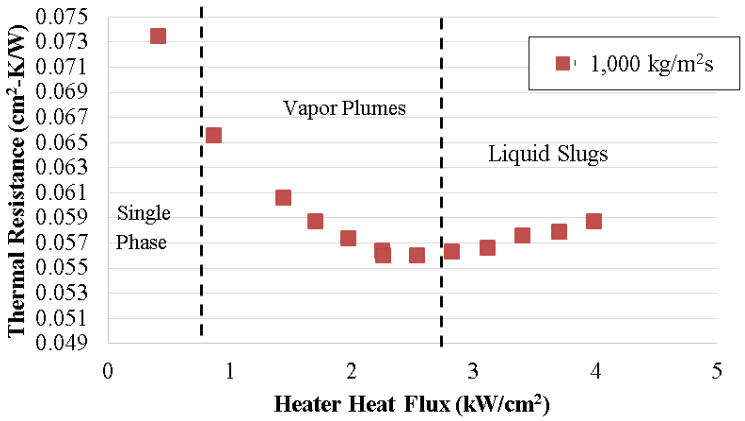
Thermal Resistance (cm²-K/W)
0.075
0.073
0.071
0.069
0.067
0.065
0.063
0.061
0.059
0.057
0.055
0.053
0.051
0.049
0
1
2
3
4
5
Heater Heat Flux (kW/cm²)
1,000 kg/m²s
Vapor Plumes
Liquid Slugs
Single
Phase

(a)

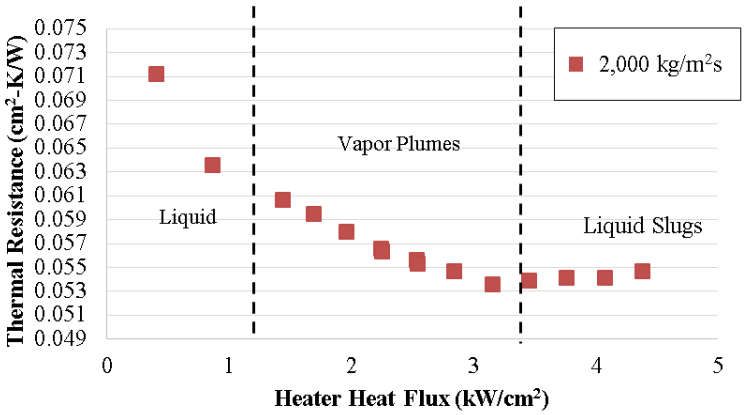
Thermal Resistance (cm²-K/W)
0.075
0.073
0.071
0.069
0.067
0.065
0.063
0.061
0.059
0.057
0.055
0.053
0.051
0.049
0
1
2
3
4
5
Heater Heat Flux (kW/cm²)
2,000 kg/m²s
Vapor Plumes
Liquid
Liquid Slugs

(b)

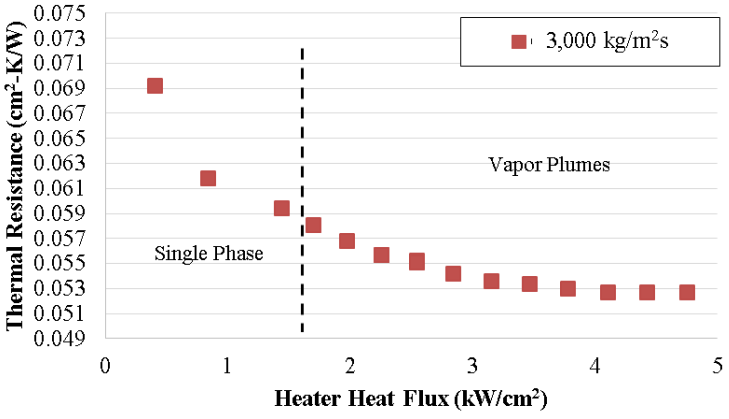
Thermal Resistance (cm²-K/W)
0.075
0.073
0.071
0.069
0.067
0.065
0.063
0.061
0.059
0.057
0.055
0.053
0.051
0.049
0
1
2
3
4
5
Heater Heat Flux (kW/cm²)
3,000 kg/m²s
Vapor Plumes
Single Phase

(c)

Fig. 3.7 Thermal Resistance vs heat flux for Gen 3 device: (a) G=1000 kg/m^{2}s (b) G=2000 kg/m^{2}s (c) G=3000 kg/m^{2}s, mapped into flow regimes described in Fig. 3.8

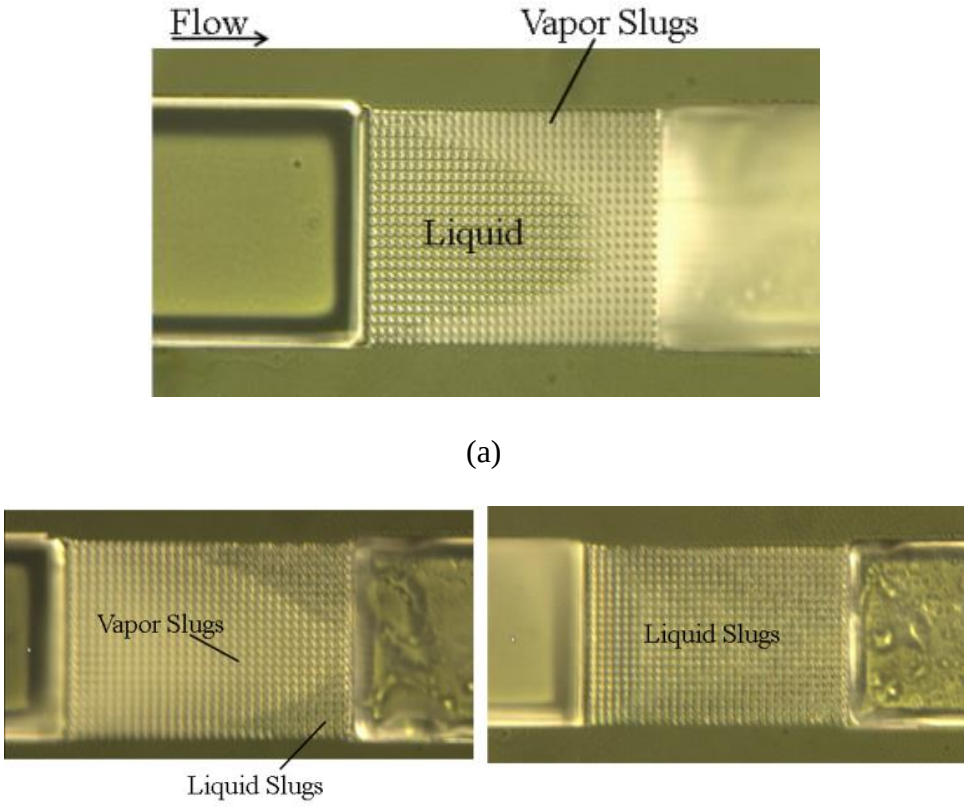

Fig. 3.8 Visualization of Gen 3 device flow regimes: (a) vapor plume flow, (b) transition to liquid slugs flow, (c) liquid slug flow

Thermal resistance trends in the Gen 3 devices follow similar trends as those in the Gen 2 device, with decreasing thermal resistance during vapor plume boiling due to decreasing liquid layer thickness and increasing thermal resistance during liquid slug boiling due to increasing area of dry patches. The pin fins in Gen 3 devices increased surface area contact with the coolant in the microgap by a factor 2.27, which resulted in a reduction of the minimal overall thermal resistance of Gen 3 devices by an average of 3.5% compared to Gen 2 devices. While the pin fins greatly enhanced the contact area for heat rejection to the coolant, they also disrupted the

continuity of the liquid film wetting the microgap surface, which is responsible for the highest heat removal rates in convective boiling [7, 31-32]. With a high pin fin density in Gen 3 devices, recirculation zones behind the fins may cause an increase in thermal resistance if slow moving fluid rapidly evaporates in these zones. This is expected to be the case for tests done at 1,000 kg/m^2s and 2,000 kg/m^2s where flow regime transitions in the microgap occur at similar heat fluxes for Gen 2 and Gen 3 devices. It was expected that the increase in inlet pressure resulting from flow constriction in the presence of pin fins would raise the saturation temperature of the coolant in Gen 3 devices thereby shifting flow regime transitions to higher heat fluxes than Gen 2 devices. This was observed in the $3{,}000kg/m^2s$ test, where the transition to liquid slug regime in Gen 2 devices was observed at $3.71kW/cm^2$ and not in Gen 3 devices even at heat fluxes as high as $4.75kW/cm^2$, where the fluid remained in the vapor plume regime. Although Gen 3 devices did not greatly reduce thermal resistance when compared to Gen 2 devices, they can extend the range of operation at low thermal resistance to substantially higher heat fluxes where the thermal performance of Gen 2 devices would degrade.

Repeated tests at the same heat and mass fluxes on multiple Gen 3 devices showed consistent boiling mechanism and thermal performance; however, there were some outlying observations that are not well understood, but worth mentioning. One device tested showed a bubbly flow regime at low heat fluxes, for which in other Gen 3 devices single phase flow was observed. These bubbles were generated at nucleation sites in the inlet plenum and advected into the microgap by the bulk liquid flow. This behavior was similar to the stratified boiling regime of Gen 1 device shown in Fig 3.2-a. The emergence of stratified flow in Gen 1 devices and bubbly flow in Gen 3 devices may be related to the surface roughness of the inlet plenum, which may contribute to nucleation in some devices and not others. As heat flux was increased in the

bubbly flow regime, the density of bubbles increased resulting in bubble coalescence in the outlet plenum. Rather than transition to a vapor plume regime as typically observed in other devices, the zone of the bubbly flow expanded to a point where the entire microgap dried out momentarily followed by rewetting of the surface and finally stable liquid slug flow. When the heat flux was reduced following the onset of liquid slug boiling, the vapor plume regime was recovered. This boiling hysteresis was repeatable and occurred consistently in several tests of the same device. The boiling hysteresis where bubbly flow regime 'bypassed' the vapor plume regime as heat fluxes were increased occurred after running a few tests in reverse flow. This suggests that there could have been trapped vapor bubbles in the system that were introduced into the device, which would explain the brief dryout in the microgap prior to rewetting.

3.4 Pressure Drop.

Pressure drop as a function of heater heat flux for all devices tested at various mass fluxes is shown in Fig. 3.9. The Gen1 device shows nearly uniform pressure drop in the stratified boiling regime with increases in heat flux across a wide range of mass fluxes. The vapor fractions in stratified boiling regime appear to be very low in flow visualization as shown in Fig. 3.2a with flow being primarily in liquid phase. This is supported by a constant pressure drop at heat fluxes in the stratified flow regime. The transition to vapor slug boiling increased total pressure drop due to the addition of an acceleration pressure drop between vapor and liquid phases. Pressure drop continues to increase with increases in vapor content at higher heat fluxes in the vapor plume regime (Fig. 3.2-b-c); when vapor slugs occupy the entire microgap, the pressure drop is nearly double that of the stratified boiling regime. The large pressure drop particularly occurs when boiling transitions to the inlet plenum, which substantially raises the inlet pressure. This could be due to numerous factors, but most likely due an increased pressure

head loss due to rapid constriction at the inlet when fluid enters a microgap at high velocity as vapor-rich two-phase mixture. The outlet pressure is always fixed at the system pressure due to the presence of a large buffering reservoir filled with a refrigerant's saturated mixture at a fixed temperature, so the change in inlet pressure directly correlates with the pressure drop. The transition to UTF boiling (Fig 3.2-d) showed a small increase in pressure drop from that of vapor slug boiling as vapor content increased.

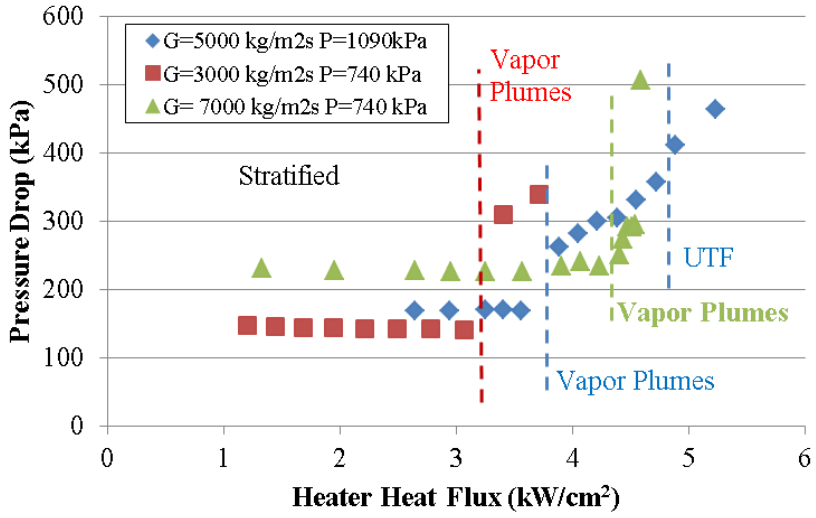

(a)

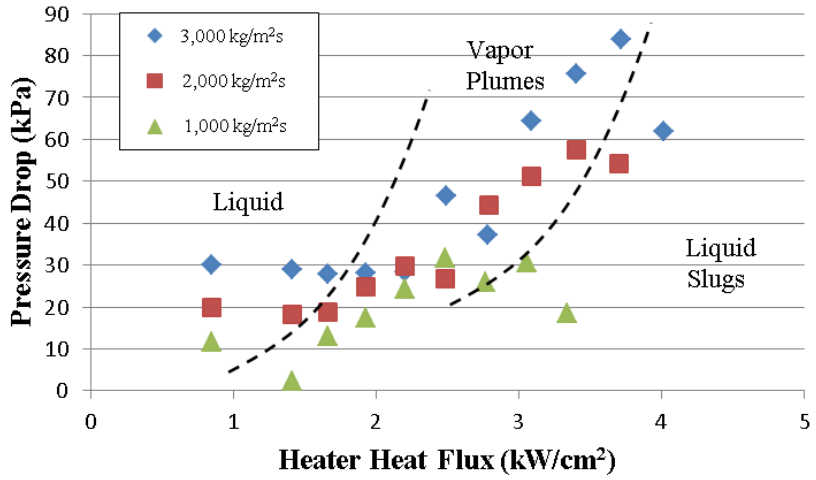

(b)

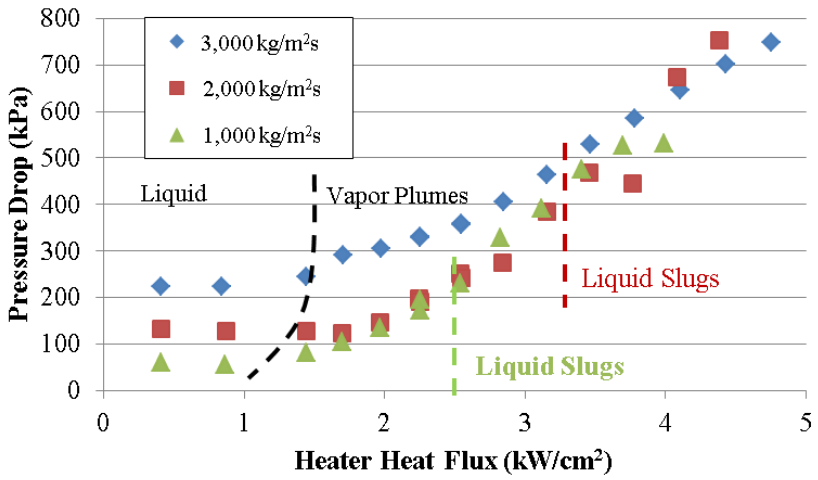

(c)

Fig. 3.9 Pressure Drop vs Heat Flux (a) Gen 1 Device (b) Gen 2 device at 820 kPa system pressure (downstream of microgap) (c) Gen 3 Device at 820 kPa system pressure (downstream of microgap).

Pressure drop in Gen 2 devices is constant for a given mass flux in the single phase flow regime, as expected, and steadily increases with heat addition in the vapor slug boiling domain (Fig 3.5-a) due to an increased acceleration between phases and viscous losses. The pressure drop reaches a maximum at the point where the boiling regime transitions to liquid slugs as shown in Fig 3.9-b. As the liquid slug boiling proceeds, the pressure drop decreases with increasing dryout in the microgap. Since outlet pressure is fixed at system pressure, the decrease in pressure drop is a result of a decrease in inlet pressure. Local dryout in the microgap and subsequent transition to liquid slug regime occur when fluid in the inlet plenum boils. In Gen 2 and Gen3 devices, inlet pressure is recorded in the inlet plenum via pressure tap located in an immediate vicinity of gap entry, as shown in Fig 2.2. As a result, when fluid boils in the inlet plenum, the pressure recorded does not correspond to the actual fluid pressure at the inlet, but is equal to the saturation pressure at the temperature where the pressure transducing element is

located (being further away from the microgap and near the contact with environment, it is always a measure of coolant saturation pressure near ambient temperature). Thus, this has the unintended effect of distorting actual pressure drop when fluid boils in the inlet plenum. The impact of this pressure distortion only affects the data points in the liquid slug/film regimes when the refrigerant vapor is in the inlet plenum. One would expect that the true pressure drop would continue to increase as observed in the Gen 1 device, which had no issues with location of pressure taps.

Boiling pressure drops in Gen 2 devices are significantly smaller in magnitude than those of Gen 1 devices at the same mass fluxes because the microgap height is twice as tall as the Gen 1 device (10 μm vs 5 μm). The pressure drop is higher in the Gen 1 device for the same heat and mass flux because there is a larger vapor content (higher quality) in the smaller gap height than in the larger one due to lower coolant volumetric flow rate in the smaller gap devices at the same mass flux conditions; as a result pressure drop is increased by the acceleration between phases and viscous losses. Alam [2] observed a similar occurrence where microgaps of decreasing height showed substantially larger pressure drop for the same mass fluxes. The Gen 3 device followed the same pressure drop trends as the Gen 2 device in the vapor plume flow regime; however, the pressure drop in the Gen 3 device did not decrease at the transition to liquid slug boiling. The pressure drop never decreased at the liquid slug regime because there was no boiling in the inlet plenum, and therefore the artifact of pressure reading at inlet taps filled with vapor condensed at the environmental temperature was avoided. Note that pressure drop for the 1,000 kg/m^2s case exceeds that of 2,000kg/m^2s case in liquid slug boiling because the transition to the liquid slug regime occurred at a lower heat flux for the lower mass flux, and therefore the vapor

content is higher at the same heat flux, with corresponding increase in the acceleration and viscous pressure drops despite the lower mass flux.

Chapter 4

Model Development

In the previous chapter, an experimental thermal characterization was performed in terms of thermal resistance and pressure drop trends as a function of heater heat fluxes. These are parameters that could be calculated directly from experimentally measured quantities. To complete the thermal characterization of the assessed microgap based hotspot devices, a finite element steady state conjugate heat transfer model was built in COMSOL to determine heat transfer coefficient and quality in the microgap at experimentally tested heat fluxes for Gen 2 and Gen 3 devices. Experimental methods for measuring heat input into the microgap, needed to calculate heat transfer coefficient and quality, are ineffective due to the large silicon medium for heat spreading from the heat generation site (heaters) to the microgap surface over which coolant flows. The developed model was also used to determine wall temperature at the heater surface as a function of the heat flux input into the microgap for the Gen 3 Devices. A dedicated model for the 5 μm tall microgap, Gen 1 device, was not developed due to the absence of pressure ports needed to estimate coolant temperature distribution along the microchannel for reasonable approximation of convective heat transfer.

4.1 Motivation for Numerical Modeling

As mentioned in 3.1, there is a 280 μm thick silicon layer in between the heaters generating the hotspot heat fluxes and the microgap surface where coolant flows. This silicon layer acts as a medium for heat to spread by conduction and bypass the coolant flowing in the microgap as shown in Fig 3.3**.** The large domain for heat spreading, although reduced by the presence of air trenches in Gen2 and Gen3 devices, imposes a limitation on correlating heater

heat fluxes to convective boiling within the microgap in the absence of reliable experimental methods that can be used to quantify the heat losses due to the extremely small features of microgap (more details in section 3.1). A numerical model is used to simulate heat flow through the device to quantify the fraction of heat generated by the heater that is absorbed by the coolant within the microgap; this is needed to determine heat transfer coefficient and quality. In this chapter, the development of a steady state heat transfer model of the experimental test section, applied boundary conditions and model validation approach are presented.

4.2 Model Definition

4.2.1 Geometry & Material Properties

A 3D model was created in COMSOL of the experimentally investigated test section for Gen2 devices consisting of the device, PCB board it is mounted to and package providing fluidic connection to the device. Fig. 4.1 shows a cross section view comparing the actual test section and microgap based heat sink device to the simplified geometry that was modeled. In the developed model, the O-rings screws, nuts and compression fittings were not included in the computational domain because they were not expected to impact temperature distribution of the microgap device as they are located far from it. The package and PCB board needed to be modeled because they are in direct contact with the hotspot device with non-negligible heat spreading through their surfaces. Modeling of the microgap based heat sink device without the PCB and package did not provide sufficient agreement with experimental results thus making them necessary to include in the computational domain as shown in Fig. 4.2. Note that this is a full 3D model and symmetry cannot be utilized because the coolant enters the microgap at a subcooled state and exits the microgap at saturates state with nonzero quality.

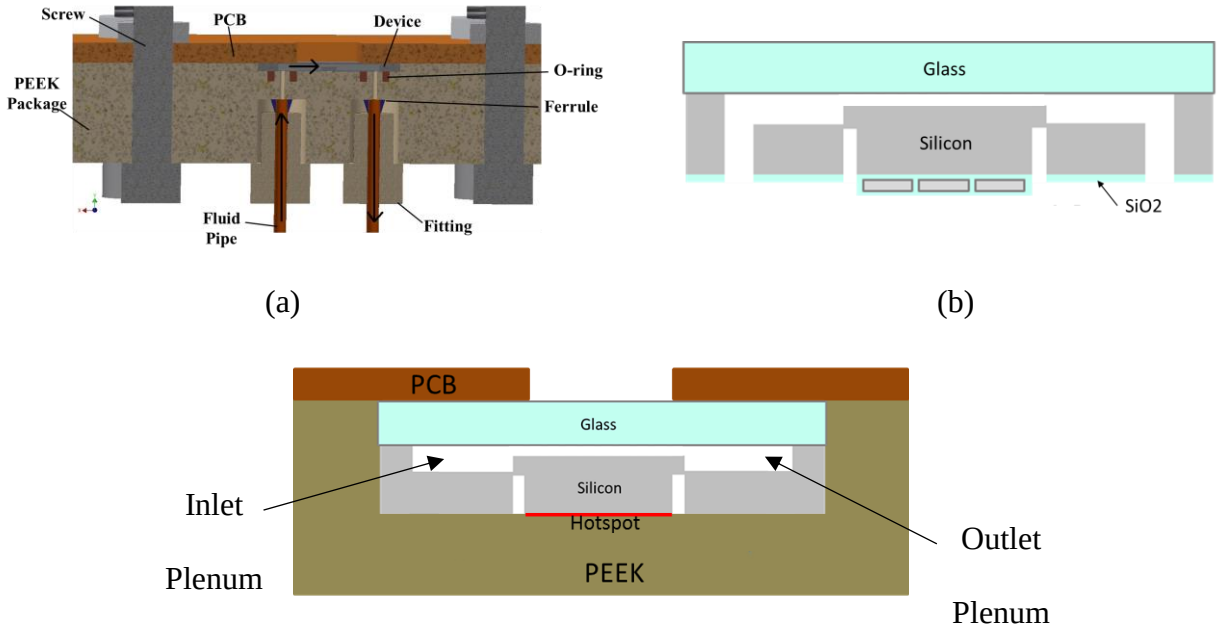

Fig. 4.1 Cross section schematics of: (a) actual experimental test section (b) Gen 2 Device (c) 3D modeled geometry (not to scale). **Fluid flow is always from left to right.**

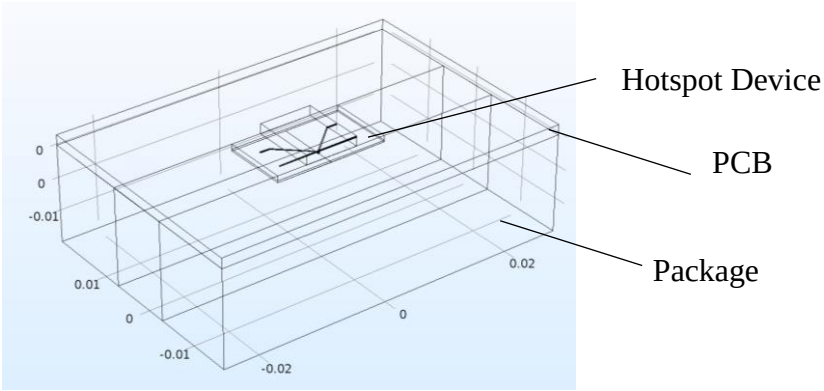

Fig.4.2 Computational domain for hotspot test section in COMSOL

The finite element model developed in this study is a steady state conduction heat transfer model with governing equation given by eq. 4.1 for 3D conduction in a solid,

$$\nabla \cdot (k\nabla T) + \dot{q} = 0 \tag{4.1}$$

Where 'T' is the temperature, '$\dot{q}$' is the heat generated per unit volume, and 'k' is the thermal conductivity, which is assumed to have the same value in all directions as all materials are assumed to be isotropic. This is not true for the FR-4 PCB board which is known to be orthotropic, however the heat flow and temperature distribution within the PCB need not be accurately modeled. Stagnant coolant in the pressure ports and air in the heater isolation trenches are modeled as a solid domain with thermal conductivity of air and R134a. Temperature dependent thermal conductivities are modeled for air in the heater isolation trenches and the silicon substrate according to eq. 4.2 [33] and eq. 4.3 [34] as they are in direct contact with the heaters generating the hotspot heat fluxes and critical to accurate representation of experimental conditions. The thermal conductivity values used in this model are summarized in Table 4.1.

$$k_{air} = 1.5207e^{-11}(T^3) - 4.8574e^{-8}(T^2) + 1.0184e^{-4}(T) - 3.9333e^{-4} \tag{4.2}$$

$$k_{silicon} = 100\left[0.03 + 1.56\left(\frac{T}{10^3}\right) + 1.65\left(\frac{T^2}{10^6}\right)\right]^{-1} \tag{4.3}$$

Table 4.1 Thermal conductivity values used in model

Material	**Thermal Conductivity (W/mK)**
R134a (in pressure taps)	0.08
Air (in heater isolation trenches)	Eq (4.2)
Silicon	Eq (4.3)
Platinum	70
Glass	1.4
Copper	400

Table 4.1 Continued

FR-4	0.5
Silicon Dioxide (SiO_2)	1.2
PEEK (package material)	0.2

4.2.2 Loading Condition

The bottom of the microgap based heat sink was modeled as a single surface with multiple thermal resistances corresponding to the individual layers on the actual device. Specifically, the bottom face of the device, over the area of the hotspot, consists of the following layers: 2 μm thick SiO_2 corresponding to the passivation layer between the heater and the silicon substrate, 700 nm platinum layer corresponding to the heater, and another 1 μm thick SiO_2 layer covering the heater. Additionally, a contact resistance was added on either side of the platinum heater with a value of 2.12e-6 m^2-K/W to provide sufficient agreement with experimental data and is in the range of observed thermal contact resistance between super lattice-metals in thin film thermoelectrics [35]. The thermal resistance of each layer is defined by the thickness of the layer divided by its thermal conductivity (given in table 4.1). The 'Thin Layer' feature in the steady state heat transfer module in COMSOL was used to achieve this representation. The hotspot was thereby modeled as a single surface with two temperatures corresponding to the top and bottom temperatures of a defined resistance network across the bottom surface of the device. The only loading condition applied to this model is a volumetric heat source across the heater layer corresponding to experimentally tested heat fluxes. Figure 4.3 shows a plot of temperature across a cutline in the center of the hotspot to illustrate how the thin layer feature was implemented in COMSOL. Using the thin layer feature makes the model more computationally

efficient by eliminating the need for a very high mesh density in the vicinity of the hotspot with length on the order of single microns.

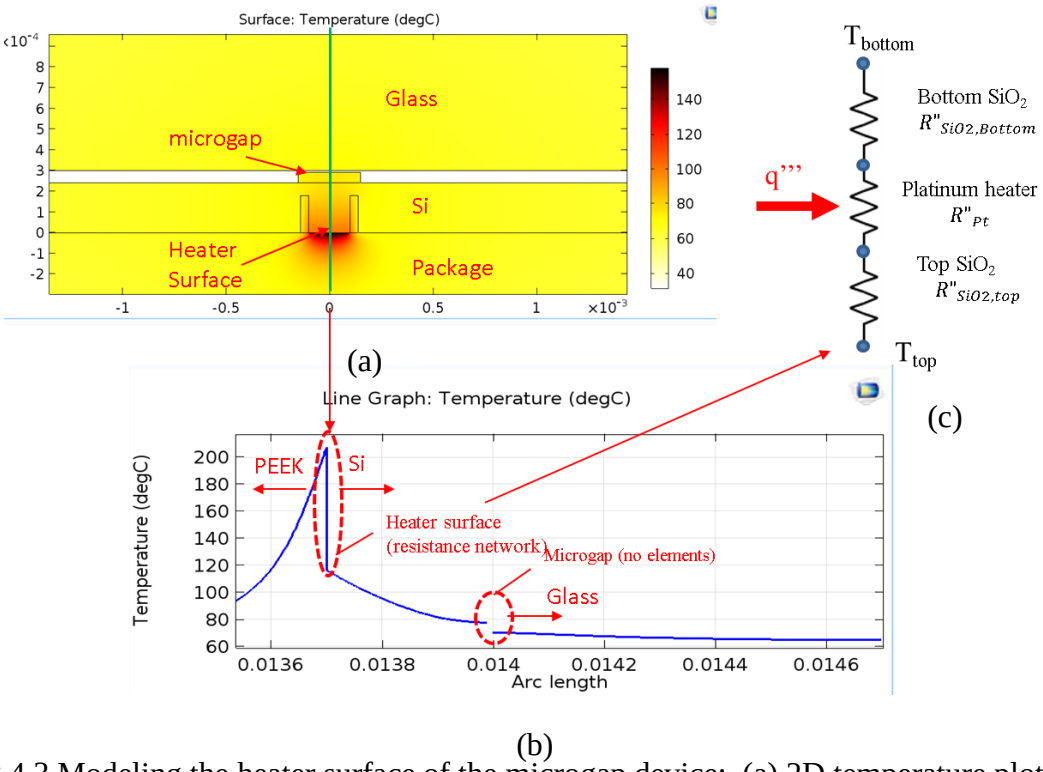

Fig 4.3 Modeling the heater surface of the microgap device: (a) 2D temperature plot of a cut plane in the center of the test section. (b) Temperature vs position plot along the green vertical line in (a). (c) Thermal resistance network defined at the heater, where q''' is the volumetric heat source applied at the platinum heater layer.

4.2.3 Boundary Conditions

Convection in this model was represented through boundary conditions on surfaces where fluid comes in contact with a solid. This is a simple approach which avoids the complexities and computational expense of fluid mechanics modeling within the microchannel while maintaining reasonable accuracy of results. Convective boundary conditions were applied on the outer surfaces of the package, PCB and exposed glass of the hotspot device to model

natural convection with the ambient air using built in natural convection correlations for heat transfer coefficient in COMSOL for flow over horizontal (eq 9.30-9.32 in [36]) and vertical plates (eq.9.26-9.27 in[36]). Within the hotspot device, convective boundary conditions were applied to the microchannel walls where coolant flows. The general convection boundary condition is given by eq. 4.4,

$$-k\frac{dT}{dn} = h(T - T_f) \tag{4.4}$$

Where $\frac{dT}{dn}$ is the temperature gradient in the normal direction to the surface, 'h' is the heat transfer coefficient and 'T_f' is the fluid temperature. Figure 4.4 shows a schematic of the modeled geometry with the walls numbered to identify the heat transfer coefficient applied to each wall. Note that the bottom surface of the glass, in contact with the coolant, and the bottom face of the outlet plenum are broken up to provide more accurate representation of variation of heat transfer coefficient across the channel. Walls 1-4 and 7-12 were assigned a single phase heat transfer coefficient obtained from Nusselt number correlation for fully developed laminar flow in an isothermal channel,

$$Nu = \frac{h_{sp}D_h}{k_{R134a}} = 4 \tag{4.5}$$

Where 'h_{sp}' is the single phase heat transfer coefficient, D_h is the hydraulic diameter, and 'k_{R134a}' is the thermal conductivity of R134a.

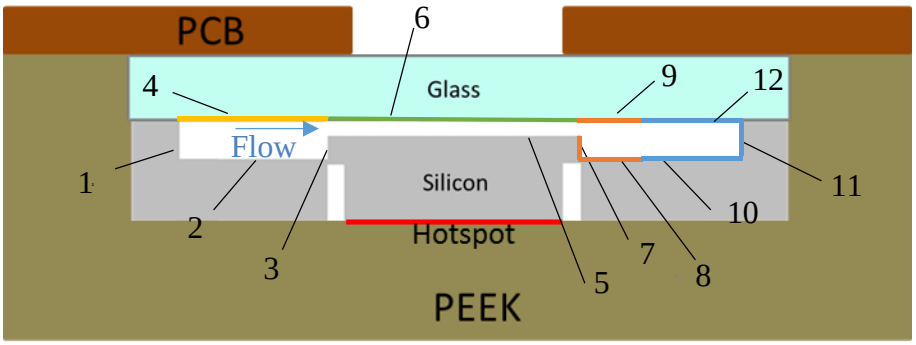

Fig. 4.4 Cross section schematic with walls labeled to identify heat transfer coefficient assignment: walls 1-4 and 10-12 are assigned single phase liquid heat transfer coefficient, walls 5-6 are assigned two phase heat transfer coefficient and walls 7-9 are assigned single phase vapor heat transfer coefficient

The assumption of laminar flow is valid because the Reynolds number does not exceed a value of 500 and is well below the transition to turbulent flow at Re =2300. Although the inlet and outlet plenum walls are not isothermal, the temperature variation along the plenums was within 10°C because the air trenches limit heat spreading to the plenums as shown in Fig 4.5. The sharp decrease in temperature away from the microgap suggests that heat transfer to the plenums becomes insignificant outside the vicinity of the microgap and assumptions made about heat transfer coefficient in the plenums do not significantly impact the accuracy of the model. Within the vicinity of the microgap the coolant was within or close to saturation conditions and the assumption of an isothermal channel is reasonable. Note that walls 7-9 were assigned a heat transfer coefficient based on a thermal conductivity of vapor phase R134a while walls 1-4 and 10-12 were assigned a heat transfer coefficient based on liquid phase R-134a. These assumptions of liquid and vapor phase domains are based on flow boiling observations. The boiling process in the hotspot device began in the region of the outlet plenum assigned a vapor phase heat transfer coefficient. This region boiled until it was primarily in the vapor phase before nucleation in the

microgap was observed. Since all simulations performed modeled boiling conditions within the microgap, it is reasonable to assume that the region at the exit of the microgap within the outlet plenum has dried out and is primarily in vapor phase.

One limitation in single phase heat transfer coefficient definition of this model is assigning a liquid phase heat transfer coefficient in the inlet plenum when nucleation sites and vapor plumes are observed within it. This only occurs at the highest heat fluxes of the Gen 2 (non-pin fin) devices and the lowest mass flux of the Gen 3 (pin fin) device when transition to the liquid slug regime within the microgap was observed. Since there are no correlations available to reliably predict two phase heat transfer coefficient for the inlet plenum geometry, data points simulated for these conditions were recognized to be outside the range of modeling validity and identified as such in the presentation of simulation results. Still, these simulations, although not expected to accurately capture boiling phenomenon within the microgap give an insight on the general trends in heat transfer coefficient with increasing heat flux.

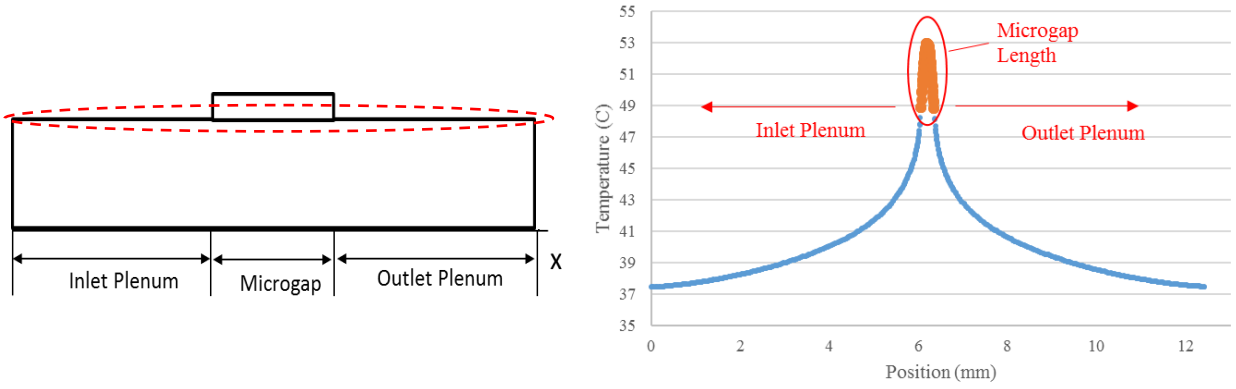

Fig. 4.5 Temperature distribution from model simulation along bottom face of plenums at a heater heat flux of 2.5 kW/cm^2

Walls 5-6 of Figure 4.4 were iteratively assigned guesses of two phase heat transfer coefficient until sufficient agreement with experimental results was obtained. For all experimentally tested heat fluxes, a simulation was performed with a matching volumetric boundary heat source and a guess for two-phase heat transfer coefficient applied to walls 5 and 6. The resulting heater temperature of the model was compared to the experimentally measured value and varied until agreement within a reasonable uncertainty band of heater temperatures was obtained. The method for determining the uncertainty band will be discussed in the next section.

Having discussed the method for selecting heat transfer coefficient for the convective surfaces of the model, all that is left is to define fluid temperature to completely define the convection boundary conditions for each surface. Figure 4.6 illustrates the assumed temperature distribution of the coolant across the microchannel. Note that the glass surface above the microchannel is broken up exactly the same as the silicon surfaces shown in Fig 4.6 with the same fluid temperature assignment to each surface. Coolant temperatures entering the hotspot device and leaving the device were measured by thermocouples while the pressure at the inlet and outlet of the microgap were measured by pressure transducers connected to the pressure ports of Gen 2 and Gen 3 devices as explained in Chapter 2.

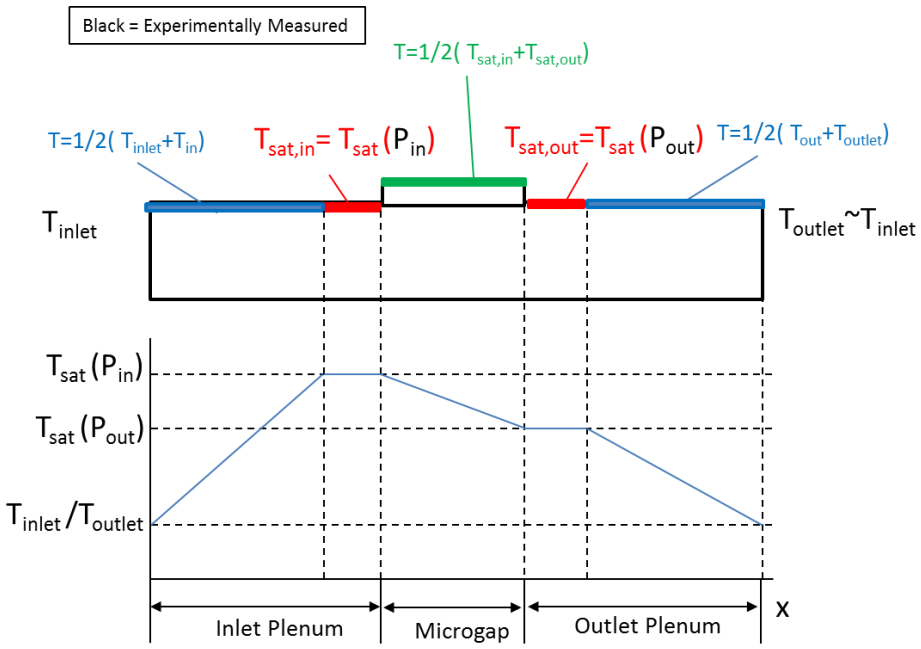

Fig. 4.6 Top: Schematic showing fluid temperature assignment for convection boundary conditions on silicon surfaces of model. Bottom: assumed temperature distribution of R134a coolant along the microchannel within the hotspot device.

As shown in Fig 4.6, coolant temperature was assumed to linearly increase from the recorded temperature at the inlet of the hotspot device to saturation temperature at the recorded inlet pressure in the red segment of the inlet plenum. The blue segment of the inlet plenum was assigned a fluid temperature at an average temperature between inlet temperature and saturation temperature at the pressure of the coolant entering the microgap. Fluid temperature was assumed to be constant at saturation temperature in the red region of the inlet plenum and linearly decrease along the microgap to saturation temperature at the microgap outlet pressure. The fluid temperature assigned to the microgap surface was taken as an average of saturation temperatures at the inlet and outlet pressures. Fluid temperature in the red region of the outlet plenum was assumed to be constant at saturation temperature of the outlet pressure and linearly decrease to

the temperature recorded at the outlet of the hotspot device. Similar to the inlet plenum, the red region of the outlet plenum was assigned a fluid temperature equal to the saturation temperature at outlet pressure and the blue region was assigned an average temperature between saturation temperature and outlet temperature.

The assumptions made about the fluid temperature along the microchannel are based on temperatures measurements, boiling observations and energy balance. Inlet and outlet temperatures are measured by thermocouples. The assumption of saturated fluid at the red segment of the outlet plenum was based on observation of boiling fluid in that region from flow visualization. The assumption of saturated fluid in the red segment of the inlet plenum was verified by an energy balance according to eq 4.6-4.8,

$$\dot{Q} = \dot{m}(h_{out} - h_{in}) \tag{4.6}$$

$$h_{out} = h(x = 0, P = P_{out}) \tag{4.7}$$

$$h_{in} = h(T = T_{in}, P = P_{out}) \tag{4.8}$$

Where $\dot{Q}$ is power, $\dot{m}$ is mass flow rate, h_{out} is the enthalpy at the exit of the inlet plenum, h_{in} is the enthalpy at the inlet of the device, *x* is the quality, T_{in} is the temperature at the inlet of the device and P_{out} is the temperature at the exit of the inlet plenum. Comparing the heat rejected by the inlet plenum walls from simulations with heat needed to raise the fluid temperature to the defined saturation temperature from eq. 4.6-4.8 showed that the assumption of saturation temperature in the red segment of the inlet plenum was valid for the Gen2 devices which do not contain pin fins. The introduction of pin fins in Gen 3 devices raised inlet pressure by an order of magnitude and the assumption of saturation temperature at the red segment of the inlet plenum was no longer valid as plenum walls do not reject enough heat to raise the coolant to the

saturation temperature at the microgap inlet pressure. For Gen 3 device simulation, the fluid temperature in the red segment of the inlet plenum must be iteratively varied until the heat rejected by the plenum walls and the heat needed to increase the temperature by that amount match. For almost all experimental tests the coolant was found to enter the microgap subcooled in Gen 3 devices based on this energy balance.

4.3 Model Validation

Mesh convergence studies were performed to ensure measurements of heater temperature, plenum wall temperature and microgap surface temperature were independent of the mesh grid size used. The parameters tested for mesh independence include the average heater temperature, plenum wall temperature and microgap surface temperature. These parameters were only found to be dependent on the mesh density in the geometry of the silicon substrate and glass. The mesh density in the package and PCB geometries were not found to impact the areas of interest within the microgap device. A total of 515,025 elements were needed to satisfy the mesh grid independence and a tolerance of 0.0001 K was used for simulation convergence.

4.3.1 Evacuated Device Model

In order to verify the developed model reliably captured heat flow through the experimentally investigated microgap devices without introducing uncertainties associated with convective boundary condition definition within the microchannel, an evacuated model is developed where heat transfer coefficient in the microchannel is zero. The boundary conditions for walls 1-12 in Fig 4.4 are given by,

$$\frac{d\mathrm{T}}{\mathrm{dn}} = 0 \tag{4.9}$$

Experimental data was collected to match the evacuated model conditions by evacuating the Gen 2 device with two, in series, vacuum pumps which bring the pressure in the device down to an absolute pressure of 30kPa. Power was applied to the heaters and heater temperature was recorded to provide data points to compare the model with. The data points collected cannot cover the range of heat fluxes tested in boiling experiments in order to avoid heater degradation in the absence of coolant, however, the relationship between heater temperature and heat flux is not expected to deviate from a linear trend in the absence of coolant. Figure 4.7 shows a comparison of the heater temperature predicted by the model and the experimentally measured temperature from an evacuated Gen 2 device. The heater temperature measured by the model is within ±1.6°C of the experimentally measured temperature, resulting in 2.16% error over the range of temperatures tested, showing that the model accurately represents the experimental test section. The uncertainty in model prediction of heater temperatures of ±1.6°C is taken into account when estimating two phase heat transfer coefficients in the microgap to capture an uncertainty band in two phase heat transfer coefficient. This will be discussed in more detail in the next chapter.

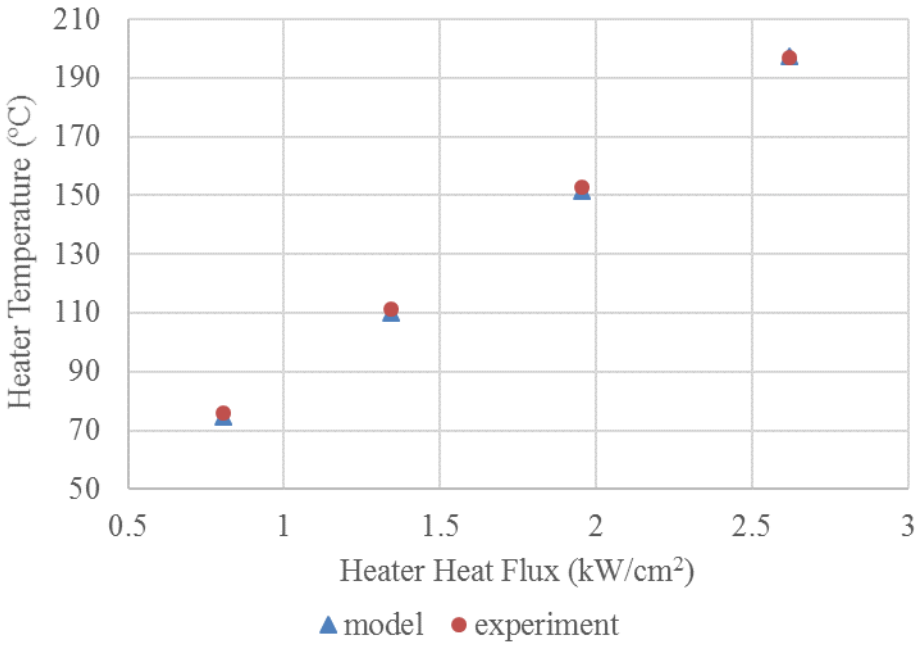

Fig. 4.7 Comparison of heater temperature predicted by model and actual heater temperature for evacuated Gen 2 device.

4.3.2 Convective Boiling Model Validation

Simulations performed to model convective boiling conditions were validated by comparing model temperatures at the location of RTDs located orthogonal to the flow direction in the microchannel to experimentally measured RTD temperatures. A description of the RTD locations on the Gen 2 and Gen 3 devices is shown in Fig.2.3 in Chapter 2. Heater temperature was not used for validation because the model heater temperature is forced to converge on the experimentally measured value by iteratively varying two phase heat transfer coefficient in the microgap for all experimental tests. Comparison of model temperatures with experimentally measured RTD temperatures are provided with the simulation results in the next chapter.

Chapter 5

Modeling Results & Analysis

The development of a finite element steady state heat transfer model of the experimental test section was discussed in the previous chapter. In this chapter, the simulation results of the model are presented to complete the thermal characterization of Gen 2 and Gen 3 devices. The results presented here include two phase heat transfer coefficient as a function of heater heat flux and quality, flow pattern maps and wall temperature as a function of microgap heat flux for all mass fluxes experimentally tested. The impact of pin fin introduction on two phase heat transfer coefficient is also assessed. Since the computational domain did not include pin fins in the microgap, a 1-D fin analysis is introduced to account for pin fin surface area enhancement in the Gen 3 device, making it possible to estimate two phase heat transfer coefficient using the model developed in the previous chapter.

5.1 Gen 2 Device Modeling

5.1.1 Two Phase Heat Transfer Coefficient vs Heater Heat Flux

Two phase heat transfer coefficient as a function of heater heat flux at mass fluxes up to 3,000 kg/m^{2}s for a 10 μm tall micrgoap Gen 2 device (non-pin fin device) are shown in Figure 5.1 with flow boiling visualization. The uncertainty band in the heat transfer coefficients corresponds to the ±1.6ºC, uncertainty in model prediction of actual heater temperatures determined in section 4.3.1. Two phase heat transfer coefficients as a function of heater heat fluxes increased in the vapor plumes regime and decreased in the liquid slugs' regime. This trend in two phase heat transfer coefficient is consistent with the trend in overall device thermal resistance as a function of heater heat flux for Gen 2 Devices shown in Fig 3.4. Thermal

resistance decreased the vapor plumes regime and increased in the liquid slugs regime. As the nucleation front of the vapor plumes moved towards the inlet of the microgap with increasing heat flux, thin film convective boiling with ultra-high heat removal rates dominated the heat transfer mechanism in the microgap causing a gradual increase in heat transfer coefficient. Increases in heater heat flux increased microgap wall superheating which caused nucleation to initiate closer to the microgap inlet. When nucleation sites move toward the microgap inlet, thin film convective boiling extends along a larger fraction of the microgap length thereby raising two phase heat transfer coefficient. This is the characteristic mechanism of the vapor slug regime in the microgap. The boiling flow visualizations images in Figure 5.1 show the movement of the nucleation front towards the microgap inlet with increases in heat flux.

Transition to the liquid slug regime indicates onset of local dryout in the microgap. Liquid slugs are surrounded by vapor and heat transfer coefficient decreases due to the low thermal conductivity of the dominating vapor phase. Two phase heat transfer coefficients within the liquid slug regime are noted to be over predicted because convective boundary conditions in the inlet plenum do not account for observed boiling in the inlet plenum. Lack of available correlations for reliable prediction of two phase heat transfer coefficient in inlet plenum geometry prevented accurate modeling. The general trend of decreasing heat transfer coefficient in the liquid slug regime can be validated by the observation of a increasing device thermal resistance seen experimentally as shown in Fig 3.4. The model is expected to over predict two phase heat transfer coefficient in the liquid slugs regime because heat rejection to the fluid in the inlet plenum is underestimated. A decline in two phase microrgap heat transfer coefficient was captured by the model in the liquid slug regime even though inlet plenum boiling was not modeled correctly because there was a surge in experimental heater temperature at local dryout.

Since the model was forced to converge on experimental heater temperature, a decline in heat transfer coefficient in the microgap was nonetheless predicted.

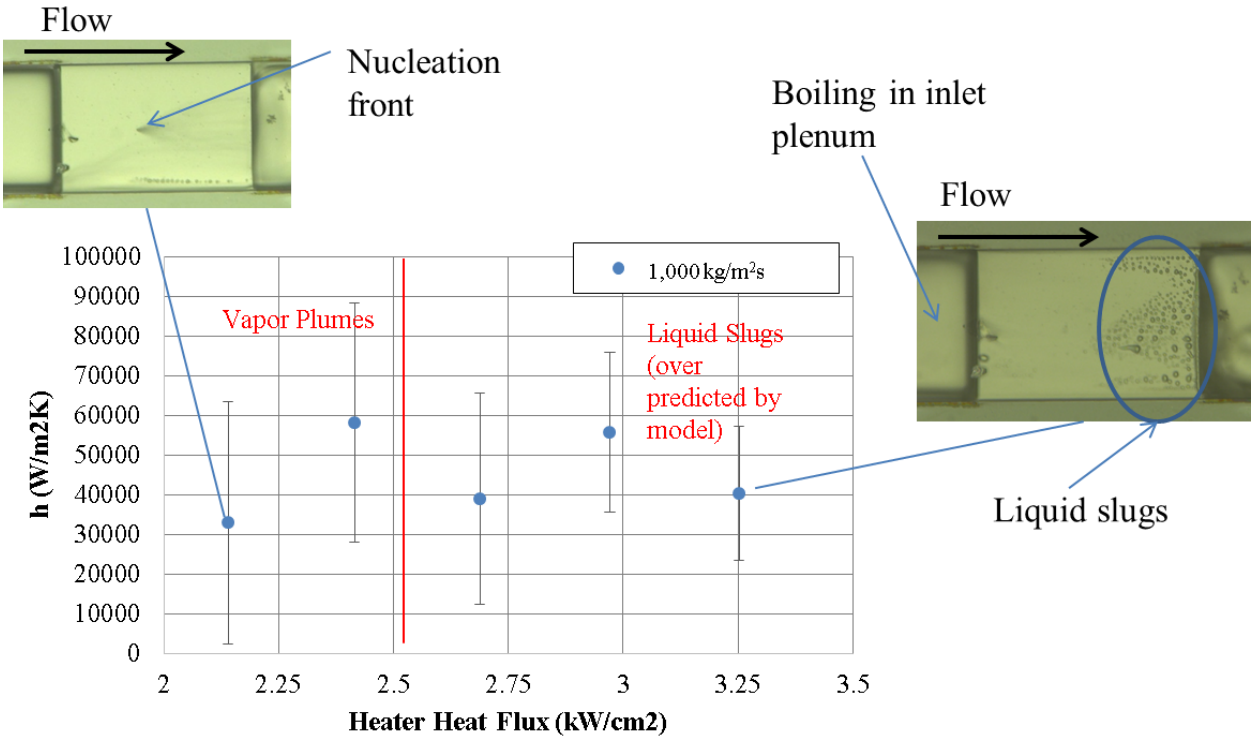

(a)

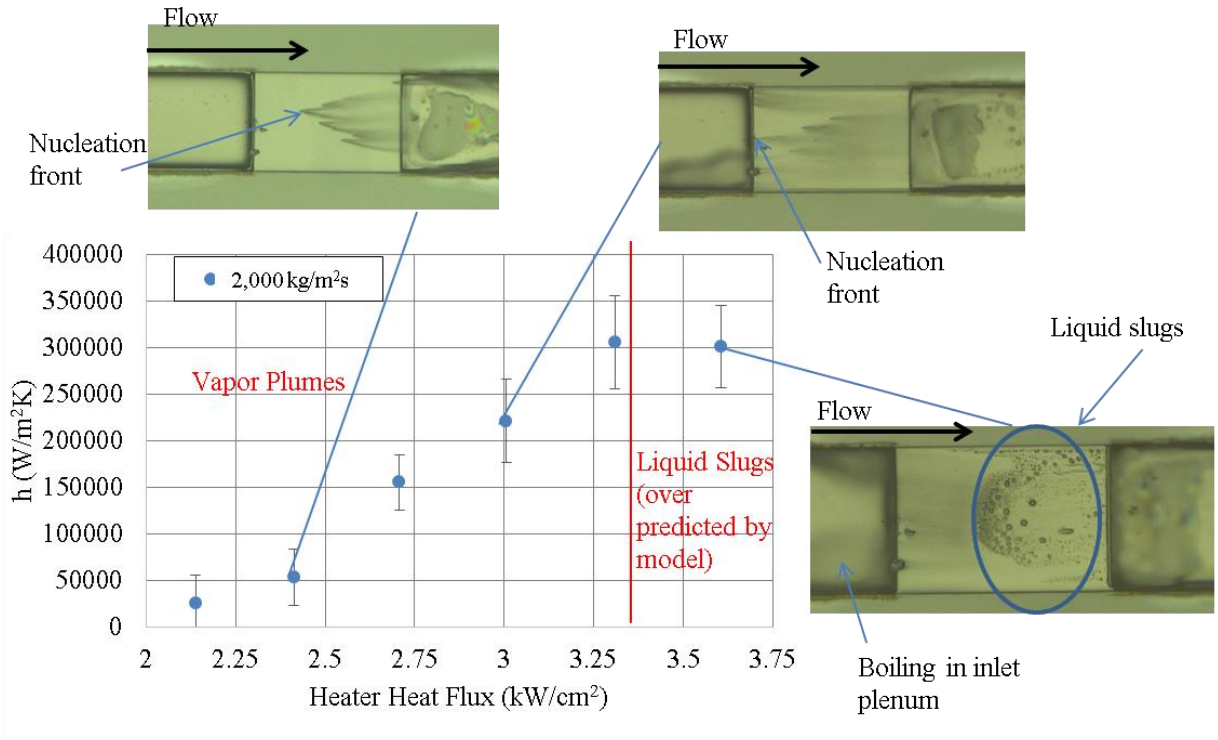
Flow
Nucleation front
Flow
Nucleation front
Liquid slugs
Flow
Boiling in inlet plenum
2,000 kg/m²s
Vapor Plumes
Liquid Slugs (over predicted by model)
h (W/m²K)
Heater Heat Flux (kW/cm²)
400000
350000
300000
250000
200000
150000
100000
50000
0
2
2.25
2.5
2.75
3
3.25
3.5
3.75

(b)

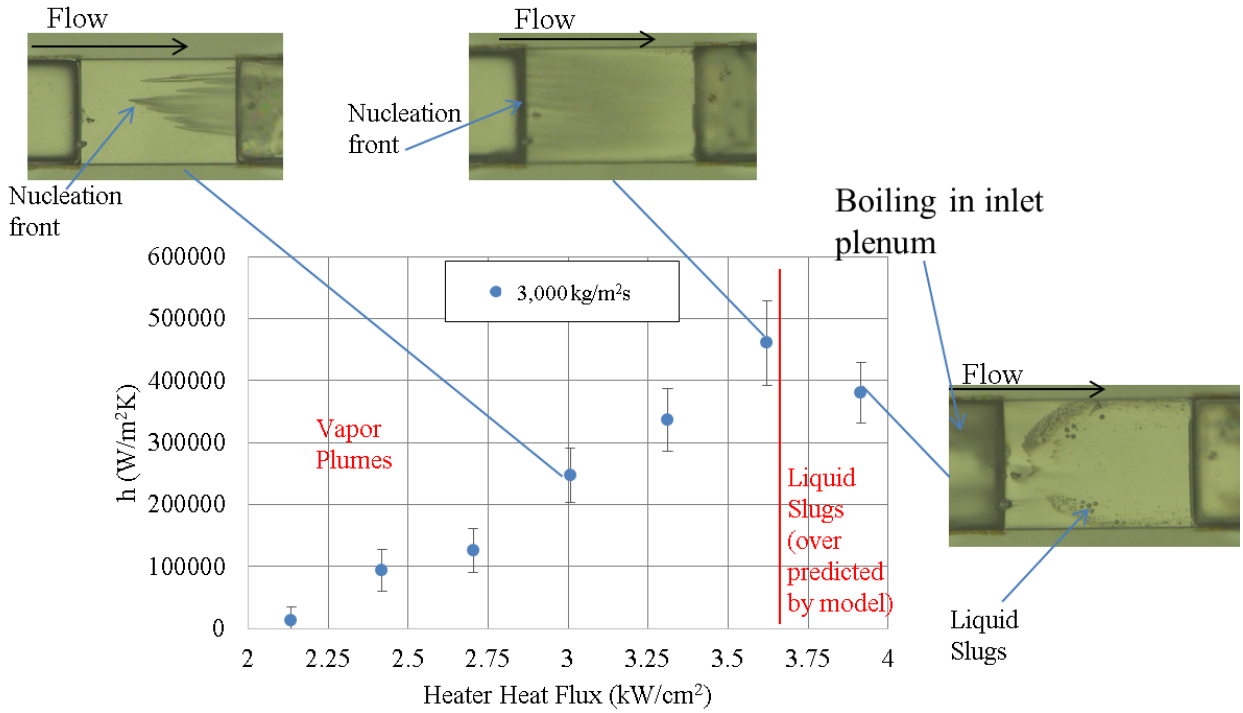
Flow
Nucleation front
Flow
Nucleation front
Boiling in inlet plenum
Flow
3,000 kg/m²s
Vapor Plumes
Liquid Slugs (over predicted by model)
Liquid Slugs
h (W/m²K)
Heater Heat Flux (kW/cm²)
600000
500000
400000
300000
200000
100000
0
2
2.25
2.5
2.75
3
3.25
3.5
3.75
4

(c)

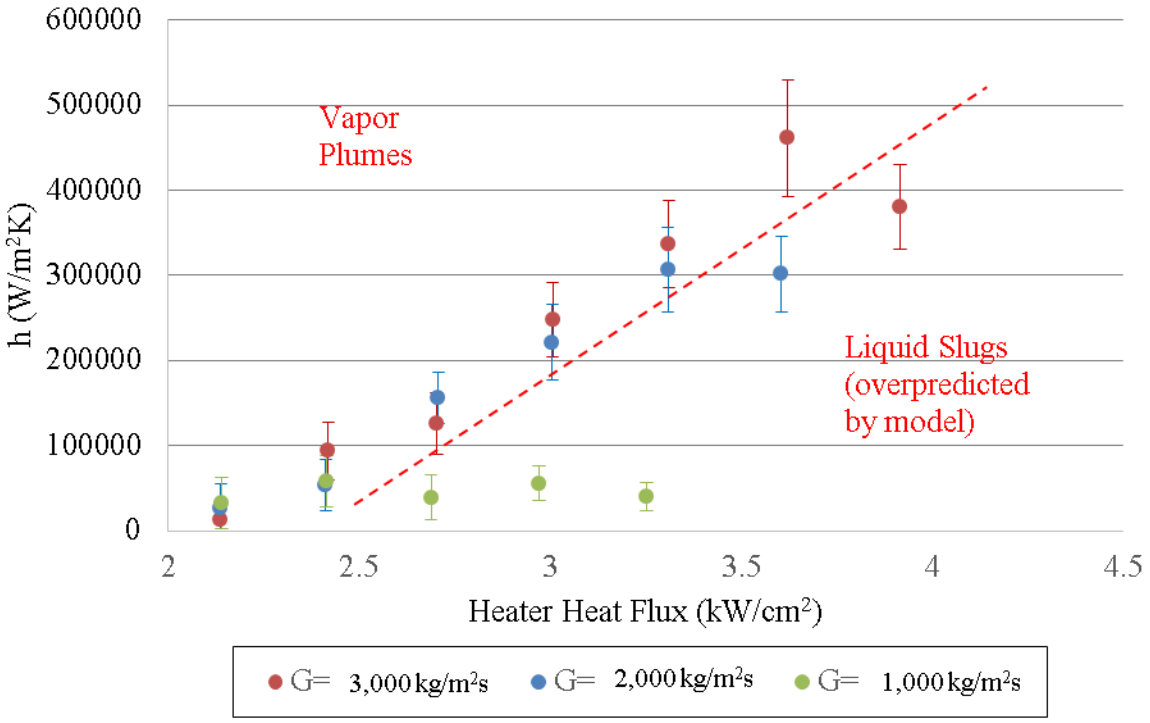

(d)

Fig. 5.1 Two phase heat transfer coefficient vs heater heat flux in 10um non pin fin microgap of Gen2 Device with flow visualization at: (a) 1,000 kg/m^{2}s, (b) 2,000 kg/m^{2}s (c) 3,000 kg/m^{2}s (d) all mass fluxes combined.

From Fig. 5.1-d, it is evident that the Gen 2 device performs best at mass fluxes above 1,000 kg/m^{2}s. Increases in mass flux demonstrate an increase in thermal performance by increasing heat transfer coefficients and enabling higher heater heat flux do be dissipated before transition to local dryout.

Not all experimental microgap boiling data points are plotted in Fig. 5.1. At the lowest heater heat fluxes where boiling was observed in the microgap, the model predicted that the heat

flow completely bypassed the coolant in the microgap by spreading and these data points were omitted from the analysis. This inaccuracy maybe due to an error in quantifying applied heater flux. The heater heat flux applied to the model is calculated by dividing the total power applied to the heaters by the rectangular footprint occupied by the serpentine shaped heater shown in Fig 2.4-b. Since actual heater area is serpentine shaped with gaps in between platinum folding, the calculated heat fluxes used in the model are lower than their experimental value. This is not expected to have a significant impact on data points modeled in Fig 5.1; however it does result in a loss of heat transfer coefficient prediction for the lowest 1-2 heat flux data points at each mass flux.

5.1.2 Two Phase Heat Transfer Coefficient vs Quality

Two phase heat transfer coefficient as a function of quality at mass fluxes up to 3,000 kg/m^{2}s for the Gen 2 device (non-pin fin device) are shown in Fig. 5.2. Quality was calculated according to eq 5.1-5.3,

$$\dot{Q} = \dot{m}\,(h_{out} - h_{in}) \tag{5.1}$$

$$h_{out} = h(x = 0, P = P_{out}) + x h_{fg} \tag{5.2}$$

$$h_{in} = (x = 0, P = P_{in}) \tag{5.3}$$

Where $\dot{Q}$ is power into the microgap, $\dot{m}$ is mass flow rate, h_{out} is the enthalpy at the exit of the microgap, h_{in} is the enthalpy at the inlet of microgap, x is the quality, P_{in} is the pressure at the inlet of the microgap and P_{out} is the temperature at the exit of the microgap. The trend of increasing heat transfer coefficient with increasing quality in the vapor plume regime is expected because quality increased as the vapor plume nucleation front moved towards the microgap inlet resulting in longer regions of thin film liquid boiling on the surface of the microgap with ultra-

high heat removal rates. The decline in two phase heat transfer coefficient in the liquid slug regime is due to the local dryout of the liquid film wetting the microgap surface in the vapor plumes regime. Again, it is noted that the model over predicted heat transfer coefficient and quality in the microgap at the liquid slug regime because convective boiling in the inlet plenum was not modeled. Over predicting the two-phase heat transfer coefficient had a propagated effect of overestimating the heat flow into the microgap and therefor results in an overestimated calculation of quality.

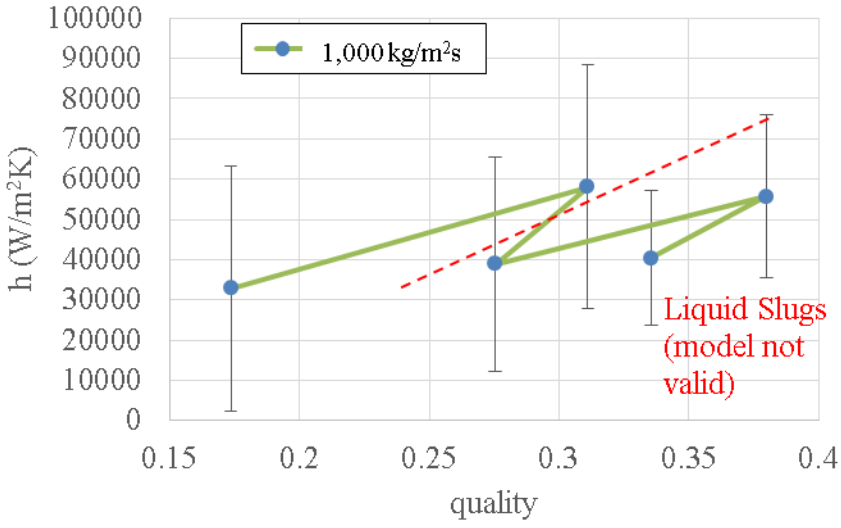

(a)

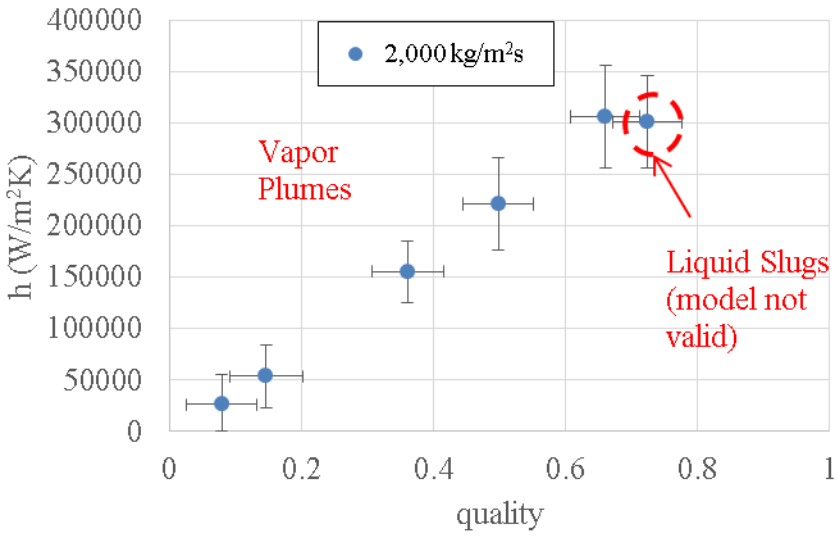
2,000 kg/m²s
Vapor Plumes
Liquid Slugs (model not valid)
h (W/m²K)
quality
400000
350000
300000
250000
200000
150000
100000
50000
0
0
0.2
0.4
0.6
0.8
1

(b)

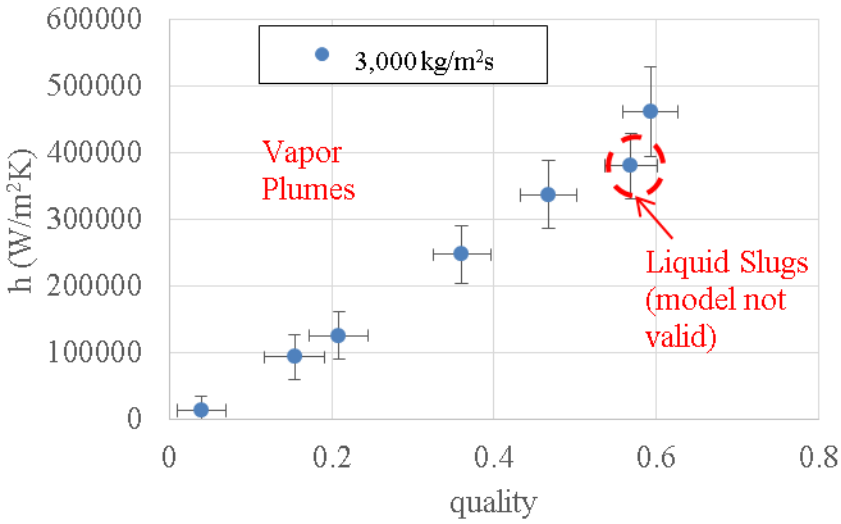
3,000 kg/m²s
Vapor Plumes
Liquid Slugs (model not valid)
h (W/m²K)
quality
600000
500000
400000
300000
200000
100000
0
0
0.2
0.4
0.6
0.8

(c)

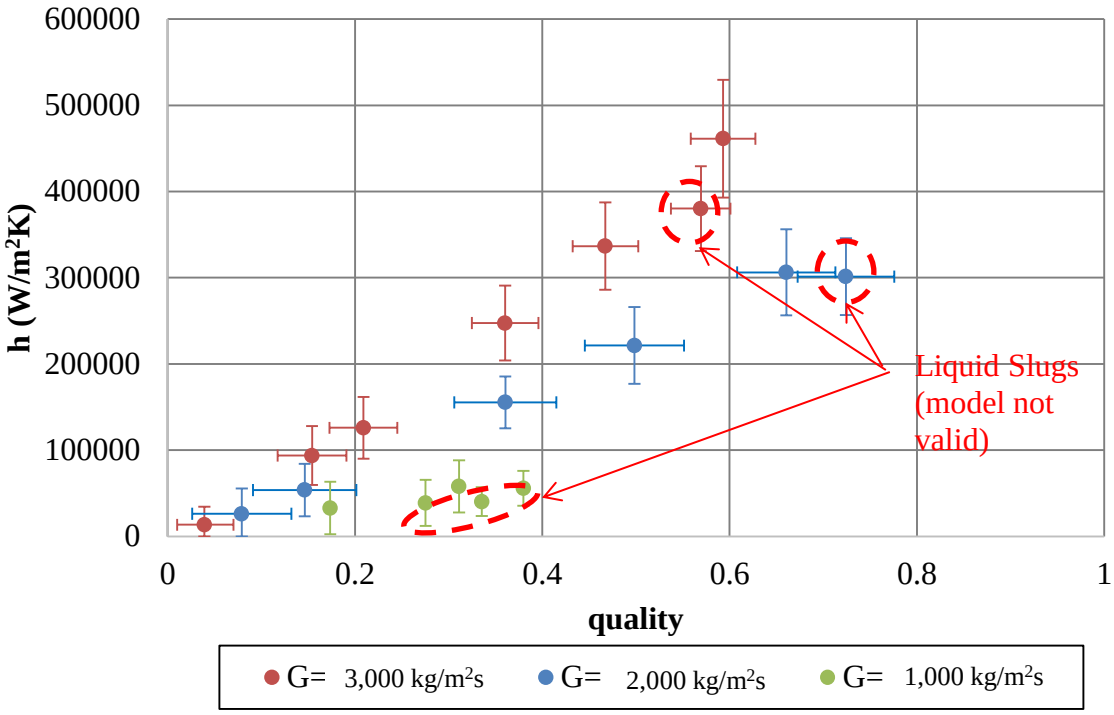

(d)

Fig. 5.2 Two phase heat transfer coefficient vs quality in 10μm non pin fin microgap of Gen2 Device: (a) 1,000 kg/m^{2}s, (b) 2,000 kg/m^{2}s (c) 3,000 kg/m^{2}s (d) all mass fluxes combined. Note: horizontal error bars on quality for 1,000 kg/m^{2}s data points are ±0.1 for each and are removed for ease of visibility of data.

In Chapter 1, a characteristic M-shaped trend of two phase heat transfer coefficient as a function of quality for microgap based heat sinks was introduced by Bar Cohen et al (shown in Fig.1.3) covering a full spectrum of quality. While the modeling results of the Gen 2 devices captured a broad range of quality, the M-shaped trend was not observed. Although the modeling presented for Gen 2 devices is only valid in the vapor plume regime, the bubbly and intermittent flow regimes which produce the first peak of the M-shaped trend proposed by Bar-Cohen et al were not observed in the extreme 10 μm tall microgap geometry investigated in this work.

Several studies [2,4,6-7,24] predict a flow regime transition to annular convective boiling at low quality, in the range of 0.15-0.4, with decreasing microgap height due to increased bubble confinement. The bubbly and intermittent regimes maybe non-existent in the extreme geometry of the Gen 2 device because bubbles are immediately forced to grow in the span wise direction upon boiling incipience in the microgap and forming the observed vapor plumes. The vapor plume regime is similar to the annular regime in the presence of a shear-driven thin film boiling mechanism dominating the heat transfer process and potentially offers the most favorable thermal performance in terms of the highest heat removal rates. In this sense, the extreme microgap geometry maybe more effective than larger scale microgaps in high heat flux dissipation because the first peak in the characteristic M-shaped heat transfer coefficient trend is absent. This is an advantage because the high heat removal rates associated with thin film boiling can be exploited over the full range of quality rather than a partial range.

5.1.3 Flow Pattern Map

A flow pattern map in terms of mass flux as a function of average quality for mass fluxes up to 3,000 kg/m^{2}s for the Gen 2 device is shown in Figure 5.3. The data collected at a mass flux of 1,000 kg/m^{2}s was omitted due to a large uncertainty in quality. With only vapor slug and liquid slug regimes existing as the dominant flow regimes for Gen 2 devices the model being valid in the vapor plume regime, it is not possible to define flow regime transition criteria for the experimentally tested data. It is also not known for certain whether the reduction in quality in the liquid slug regime is an actual phenomenon or just a modeling inaccuracy. It is possible for quality to be reduced in the liquid slug regime if the liquid slugs flowing along the microgap surface are sufficiently accelerated by the surrounding vapor through tangential stresses at the phase interface. The inability to validate quality in the liquid slug regime limits our ability to

draw valid conclusions on flow regime transition between vapor plume and liquid slug flow regimes.

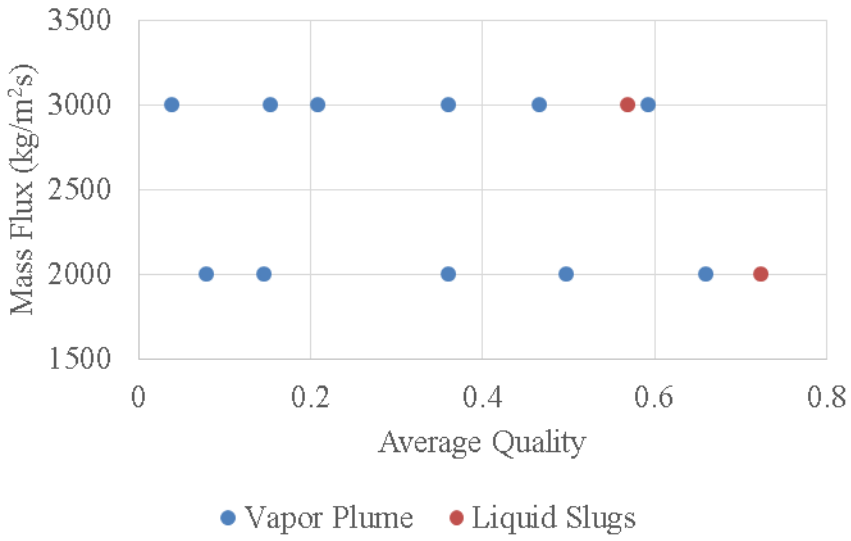

Fig. 5.3 Flow pattern map for Gen 2 Device. Data at 1,000 kg/m^{2}s was omitted due to large uncertainty in quality.

5.1.4 RTD Validation

A comparison between model and experiment RTD temperature located orthogonal to the flow direction with experimental values for all mass fluxes are shown in Fig 5.4. The purpose of this comparison is to interpret the accuracy of the model in capturing heat transfer through the Gen 2 device using the RTD temperature for reference. In the vapor plumes regime, the model is able to provide almost predict the same temperature measured by the RTD. At the liquid slug regime and the highest heat fluxes of the vapor plumes regime, the model under predicted the experimental RTD temperature. One reason for this deviation is the inlet plenum boiling inaccuracy discussed as the main reason for over predicting heat transfer coefficient and quality. In this situation, the inlet plenum inaccuracy would cause the model to under predict RTD

temperature because the heat spreading to the RTD location would be reduced. This inaccuracy could may also have been applied to the highest heat fluxes in the vapor slug domain if there was any nucleation in the inlet plenum that was not observed. Another reason for the discrepancy between model and RTD temperatures is that heat transfer coefficient in the microgap is represented by a single (average) value which neglects lateral variation in heat transfer coefficient in the microgap. The heat transfer coefficient is expected to laterally decrease away from the center of the microgap (in the direction of the RTD) due to the curved profile of the nucleation front shown in Fig. 5.1-b and 5.2-c. Lateral reduction in heat transfer coefficient in the vicinity of the RTD would drive experimental temperatures above the model where heat transfer coefficient is assumed to be uniform in the microgap. Nonetheless, the model still provides good agreement with experiments performed on Gen 2 devices and the conclusions drawn about heat transfer coefficient in the vapor plumes regime are valid.

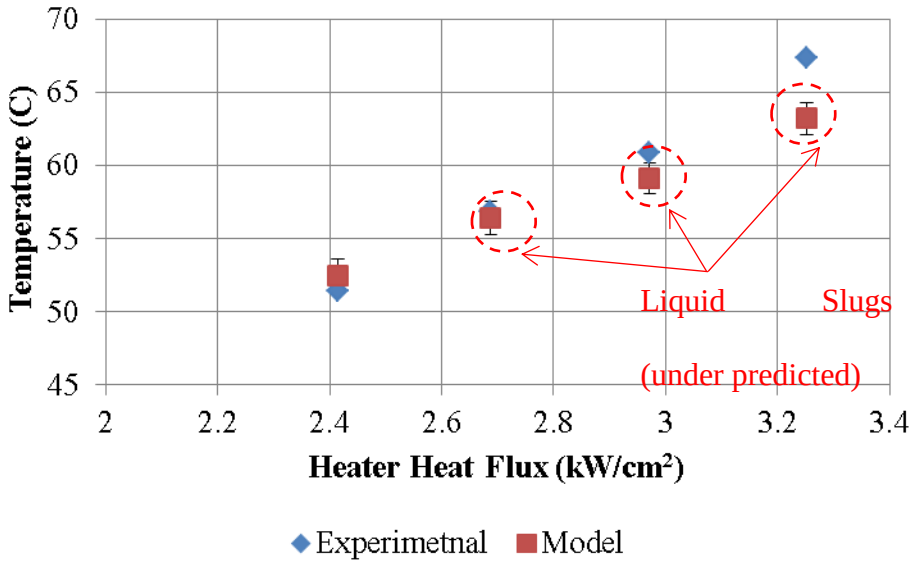

(a)

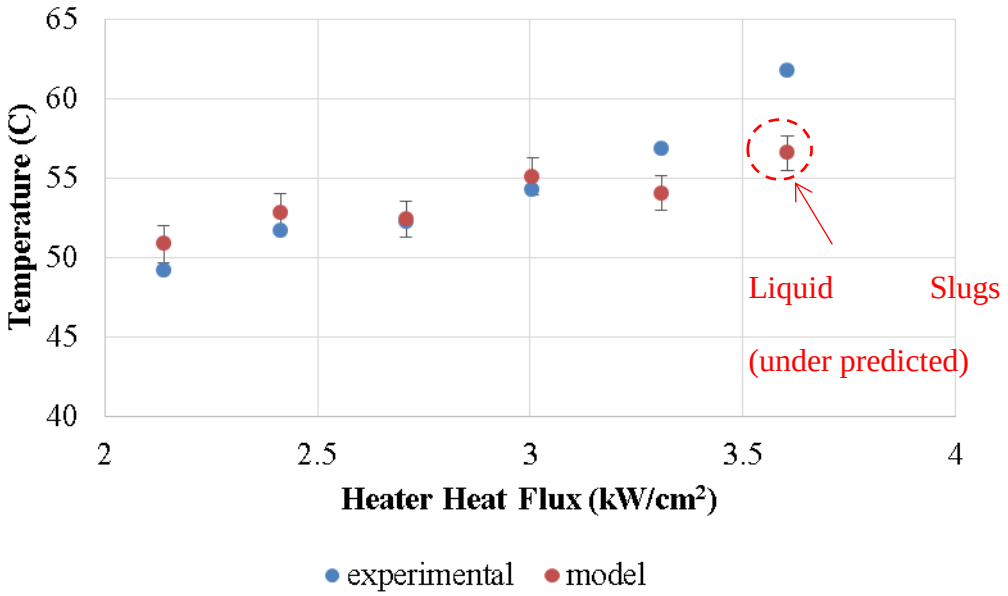

(b)

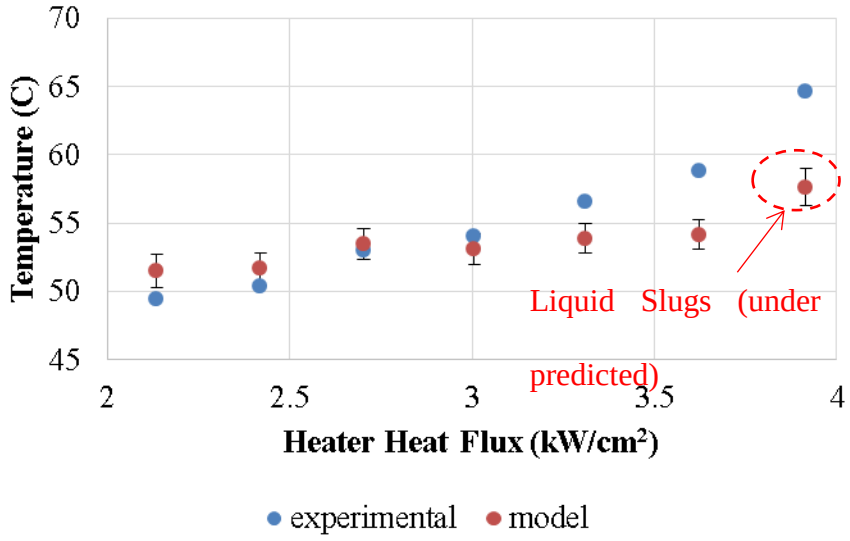

(c)

Fig. 5.4 Comparison between experimental RTD temperature and model vs heater heat flux: (a) G=1,000 kg/m^{2}s experiment (b) G=2,000 kg/m^{2}s experiment (c) G=3,000 kg/m^{2}s experiment

5.2 Gen 3 Device Modeling

5.2.1 Two Phase Heat Transfer Coefficient vs Heater Heat Flux

Two phase heat transfer coefficient as a function of heater heat flux at mass fluxes up to 3,000 kg/m^{2}s for 10 μm tall micrgoap Gen 3 devices (pin fin devices) are shown in Fig. 5.5 with flow boiling visualization. Since the finite element model used for these simulations did not include pin fin geometry in the microgap, the iteratively varied heat transfer coefficient applied to the convective boundary condition of microgap walls is not the actual two phase heat transfer coefficient because pin fin surface area enhancement is not accounted for. A 1-D steady-state adiabatic tip fin equation and Newton's law of cooling were used to determine two phase heat transfer coefficient in the microgap for Gen 3 devices according to eq 5.4-5.6,

$$\dot{Q} = h_{tp}\left(\eta A_{fins} + A_s - A_{c,fins}\right)(\overline{T_s} - T_{sat}) \tag{5.4}$$

$$\eta = \frac{tanh(m_f H)}{m_f H} \tag{5.5}$$

$$m_f = \sqrt{\frac{h_{tp} P_{fin}}{k_{fin} A_{c,fin}}} \tag{5.6}$$

Where $\dot{Q}$ is the heat rate going into the microgap, h_{tp} is the two phase heat transfer coefficient, η is the fin efficiency, A_s is the microgap surface area, $A_{c,fins}$ is the cross section area of the pin fins, $\overline{T_s}$ is the average temperature of the microgap surface, T_{sat} is the saturation temperature of the coolant in the microgap, and H is the microgap height. The heat input and average surface temperature of the microgap are found in post processing simulation results. Eq. 5.4 is a transcendental equation, where h_{tp} appears in the hyperbolic tangent term of eq 5.5, and solved iteratively.

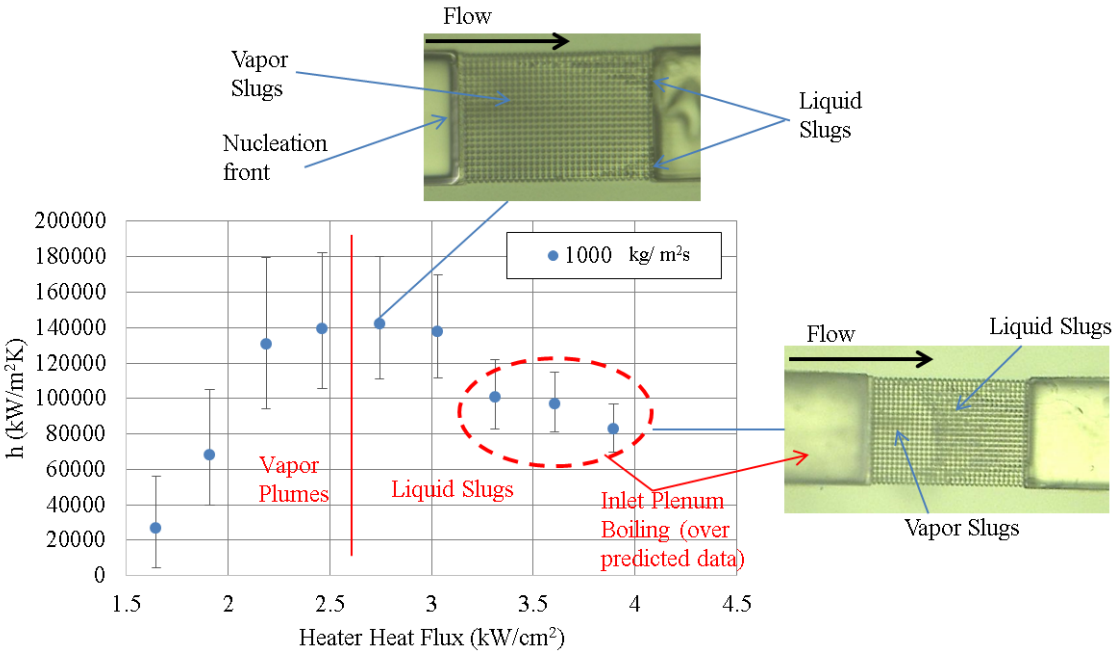
Flow
Vapor Slugs
Nucleation front
Liquid Slugs
1000 kg/ m²s
h (kW/m²K)
Heater Heat Flux (kW/cm²)
Vapor Plumes
Liquid Slugs
Inlet Plenum Boiling (over predicted data)
Flow
Liquid Slugs
Vapor Slugs

(a)

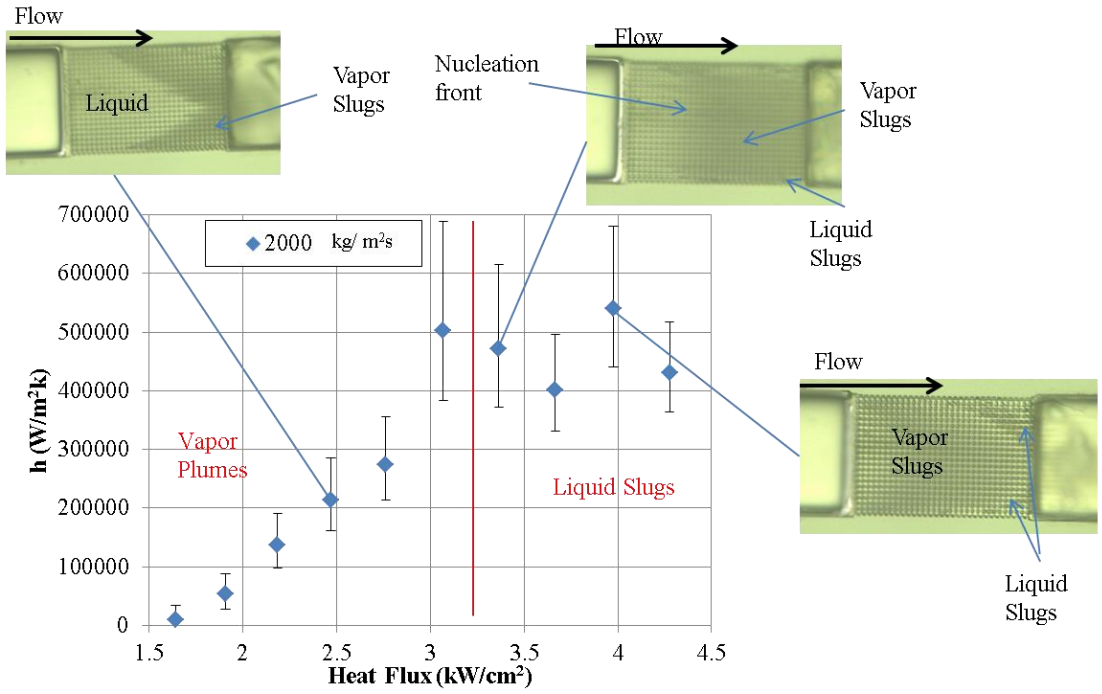
Flow
Liquid
Vapor Slugs
Nucleation front
Flow
Vapor Slugs
Liquid Slugs
2000 kg/ m²s
h (W/m²k)
Heat Flux (kW/cm²)
Vapor Plumes
Liquid Slugs
Flow
Vapor Slugs
Liquid Slugs

(b)

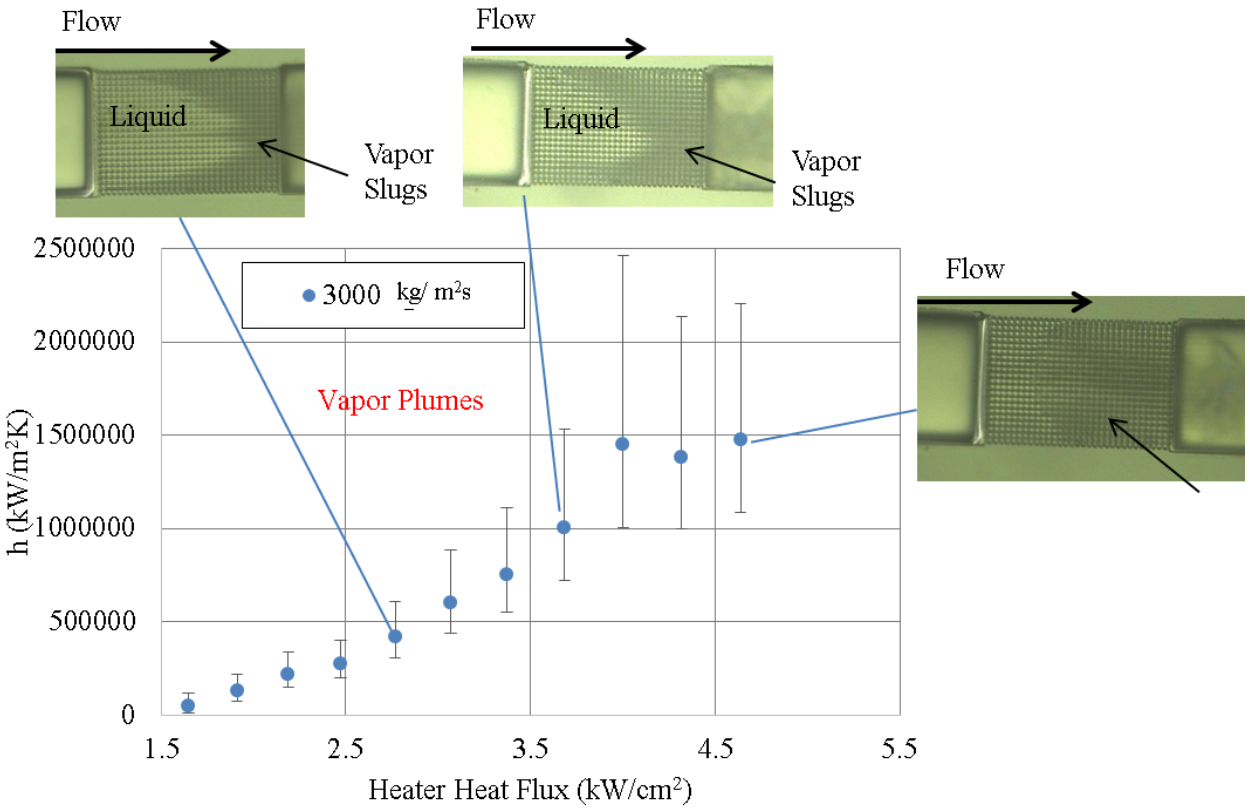
Flow
Liquid
Vapor
Slugs
Flow
Liquid
Vapor
Slugs
Flow
2500000
2000000
1500000
1000000
500000
0
h (kW/m²K)
3000 kg/ m²s
Vapor Plumes
1.5
2.5
3.5
4.5
5.5
Heater Heat Flux (kW/cm²)

(c)

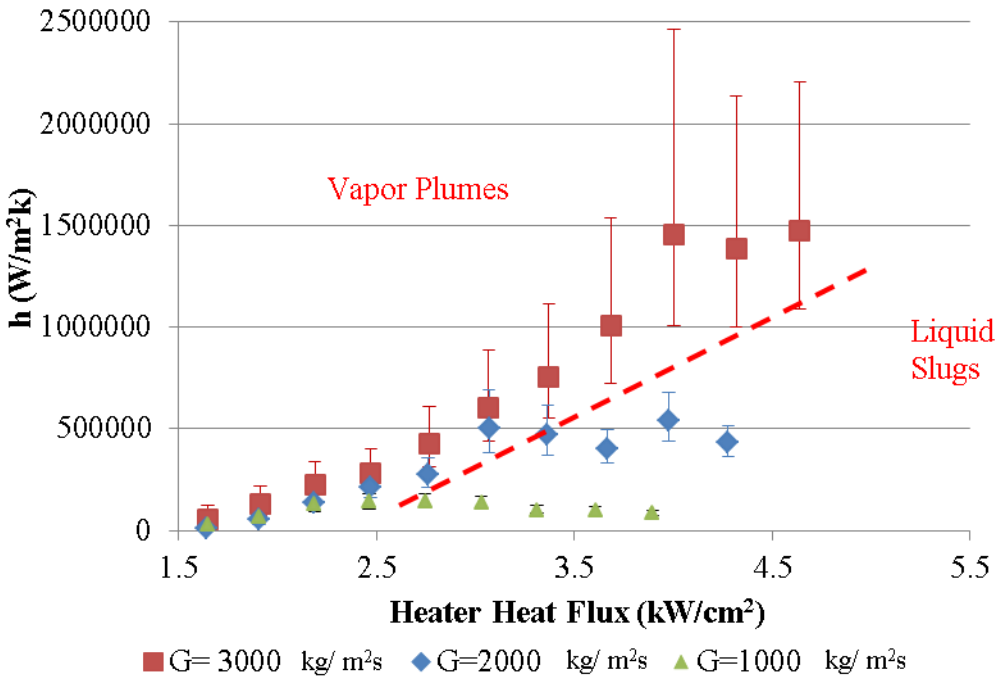

(d)

Fig. 5.5 Two phase heat transfer coefficient vs heater heat flux in 10um pin fin microgap of Gen3 Device with flow visualization at: (a) 1,000 kg/m^{2}s, (b) 2,000 kg/m^{2}s (c) 3,000 kg/m^{2}s (d) all mass fluxes combined.

Two phase heat transfer followed a similar trend to the non-pin fin Gen 2 device where heat transfer coefficient increased with increases in heater heat flux in the vapor plumes regime and decreased in the liquid slug regime. The trend of increasing heat transfer coefficient in Gen 3 devices is consistent with Gen 2 devices because the boiling process is similar. The nucleation front moved towards the inlet of the microgap with increasing heat flux as shown in the flow visualization of Fig 5.5-b and 5.5-c, with thin film boiling dominating a greater region within the microgap as the nucleation front moved closer to the inlet plenum. The onset of local dryout in the liquid slug regime resulted in a subsequent reduction in heat transfer coefficient.

Only at the highest heat fluxes of the liquid slug regime at a mass flux of 1,000 kg/m^{2}s was boiling observed in the inlet plenum. The introduction of pin fins constricting the coolant flow raised the inlet pressure of the microgap by an order of magnitude over the non-pin fin Gen 2 devices as shown in Fig 3.9. The large inlet pressure required substantially more heat to be rejected to the inlet plenum for the fluid inside it boil. Since the assumption of single phase heat transfer coefficient is reasonable in the liquid slug regime, when boiling in the inlet plenum is not observed, two phase heat transfer coefficients found in liquid slug regime are not expected to be significantly over predicted as was the case in Gen 2 devices. The data points where inlet plenum boiling occurred in Gen 3 devices are noted in Fig 5.5-a. The indicated data points are over predicted because heat rejection to the microgap is over predicted when boiling in the inlet plenum is observed because the model applied a single phase convective boundary condition in the inlet plenum. Experiments at a mass flux of 3,000 kg/m^{2}s were not tested at high enough heat fluxes to observe a transition to the liquid slug regime to avoid catastrophic failure of system components approaching their static pressure limit.

Comparing magnitudes of two phase heat transfer coefficients in fig 5.5 for Gen 3 devices to corresponding mass fluxes in Gen 2 devices in Fig 5.1 shows up to ~3x increase in magnitude with the introduction of pin fins at a mass flux of 3,000 kg/m^{2}s. Recall from section 3.3 that the Gen3 device showed only a 3.5% reduction in minimal value of overall thermal resistance compared to the Gen 2 device but substantially delayed the transition to liquid slug regime to higher heat fluxes. It may seem counter intuitive to achieve a ~3x increase in heat transfer coefficient and only 3.5% reduction in overall thermal resistance from Gen 2 to Gen 3 device performance, however comparing overall thermal resistance between devices does not provide a fair comparison of microgap performance. The calculation of overall device thermal

resistance does not distinguish between heat dissipated by spreading and heat dissipated by the microgap. In reaching a 3x improvement in maximum two phase heat transfer coefficient, the pin fin microgap of the Gen 3 device is expected to dissipate a significantly larger fraction of heat generated at the heaters compared to the bare microgap of Gen 2 devices where spreading is expected to play a more dominant role in dissipating an applied heat flux. It is also important to note that at the highest heat fluxes in Gen 3 devices, where heat transfer coefficient exceeds a value of 1,000,000 W/m^2K, small variations in heater temperature result in substantial variation in two phase heat transfer coefficient resulting in a large uncertainty band.

5.2.2 Two Phase Heat Transfer Coefficient vs Quality

Two phase heat transfer coefficient as a function of heater heat flux at mass fluxes ranging up to 3,000 kg/m^2s for Gen 3 devices are shown in Figure 5.6. Quality was calculated according to eq. 5.1-5.3 with enthalpy at the inlet of the microgap defined by the subcooled temperature of fluid in the inlet plenum at inlet pressure since the coolant did not enter the microgap at saturation conditions as seen in the Gen 2 Device. The general trend of increasing heat transfer coefficient with increasing quality in the vapor plume regime followed by a decrease in heat transfer coefficient at the transition to the liquid slug regime is consistent with flow boiling observations and Gen 2 device performance. With higher saturation temperatures and subcooled coolant entry into the microgap, flow regime transitions in the Gen 3 devices occurred at a higher quality than flow regime transitions of Gen 2 device (Fig 5.2).

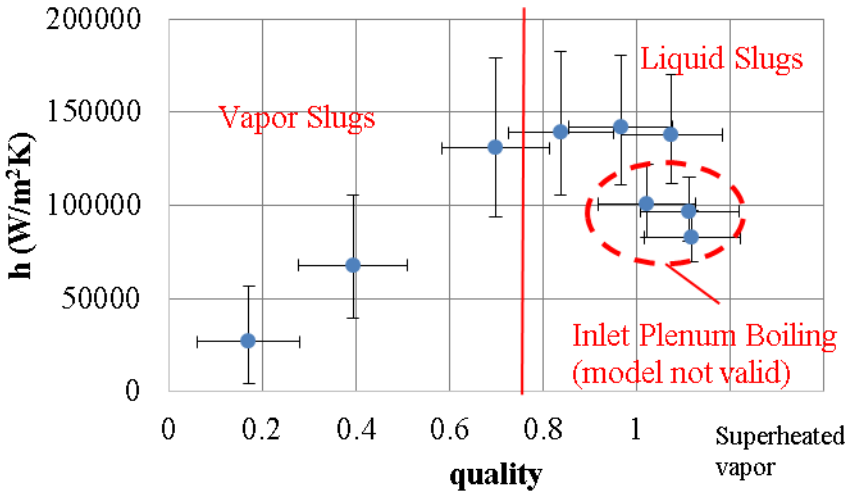
200000
150000
100000
50000
0
h (W/m²K)
Vapor Slugs
Liquid Slugs
Inlet Plenum Boiling
(model not valid)
0
0.2
0.4
0.6
0.8
1
Superheated
vapor
quality

(a)

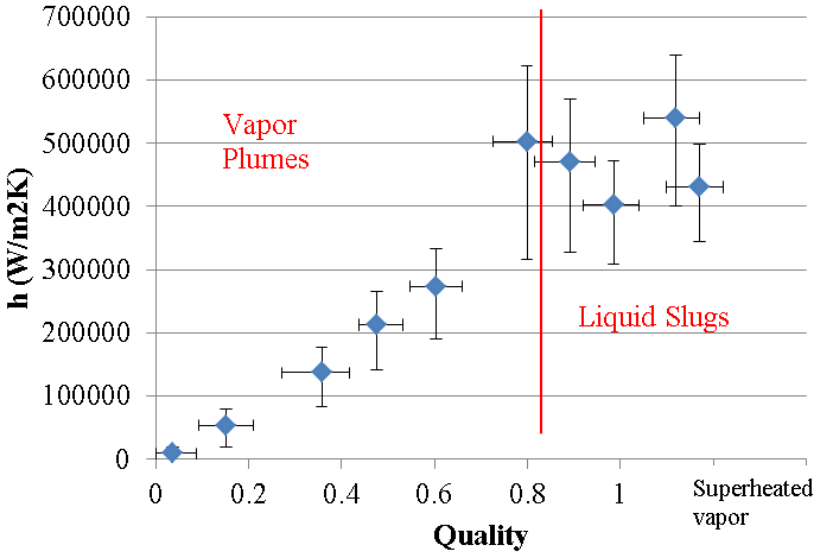
700000
600000
500000
400000
300000
200000
100000
0
h (W/m2K)
Vapor
Plumes
Liquid Slugs
0
0.2
0.4
0.6
0.8
1
Superheated
vapor
Quality

(b)

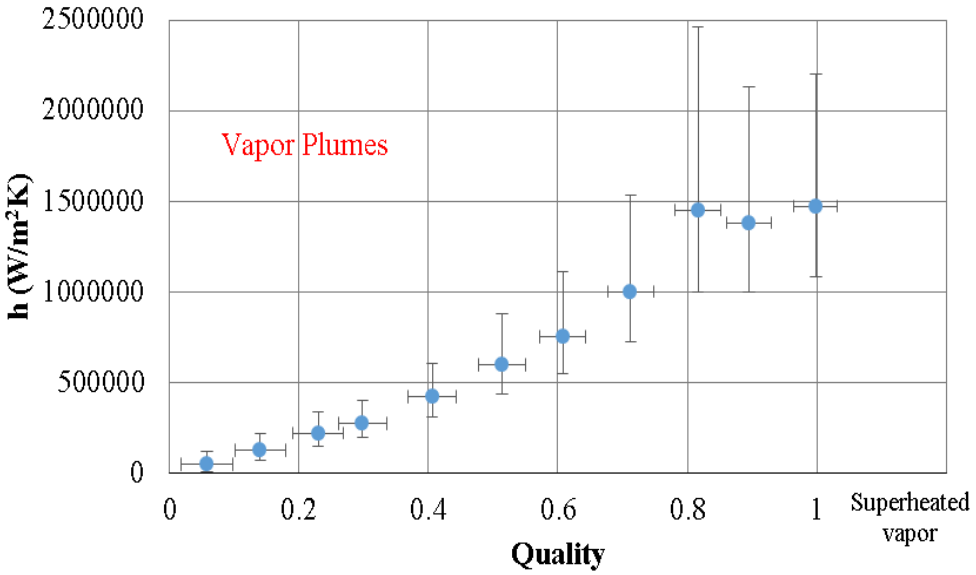
2500000
2000000
1500000
1000000
500000
0
h (W/m²K)
Vapor Plumes
0
0.2
0.4
0.6
0.8
1
Superheated vapor
Quality

(c)

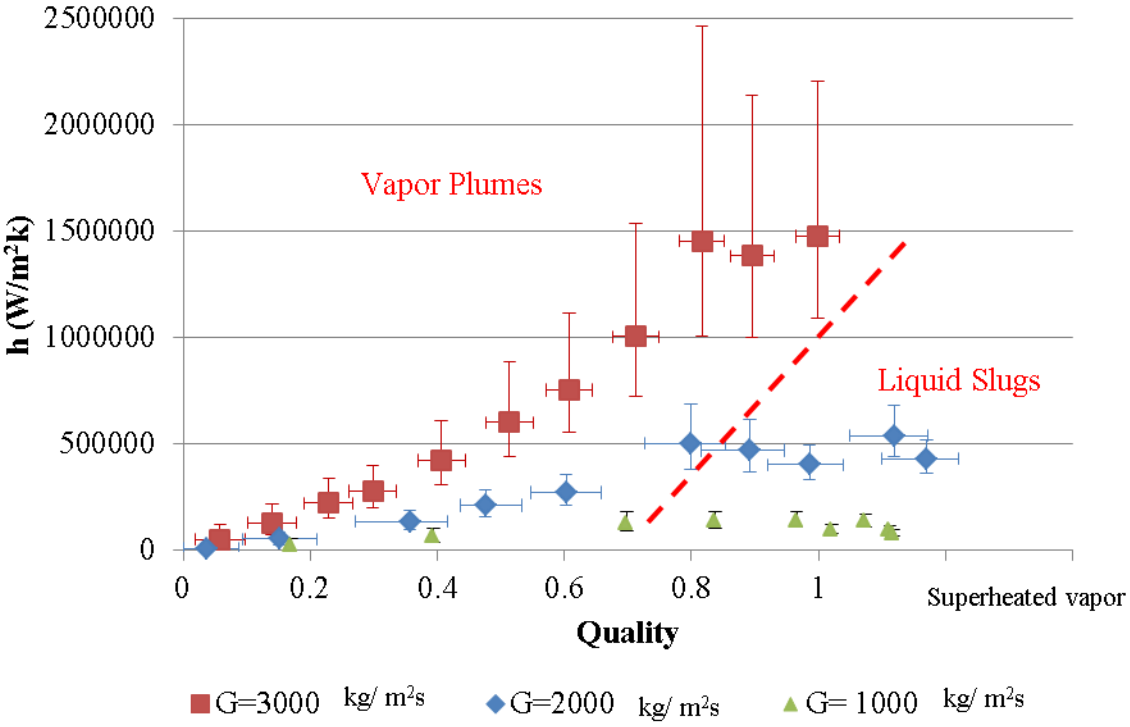
2500000
2000000
1500000
1000000
500000
0
h (W/m²k)
Vapor Plumes
Liquid Slugs
0
0.2
0.4
0.6
0.8
1
Superheated vapor
Quality
G=3000 kg/ m²s
G=2000 kg/ m²s
G= 1000 kg/ m²s

(d)

Fig. 5.6 Two phase heat transfer coefficient vs quality in 10um pin fin microgap of Gen3 Device: (a) 1,000 kg/m^{2}s, (b) 2,000 kg/m^{2}s (c) 3,000 kg/m^{2}s (d) all mass fluxes combined. Note: horizontal error bars on quality for 1,000 kg/m^{2}s data points are ±0.1 for each and are removed for ease of visibility of data.

The trend of heat transfer coefficient as a function of quality shown in Fig. 5.6 exceeded unity for all mass fluxes even though local dryout was not observed at 3000, kg/m^{2}s. This is expected to be an inaccuracy of the model in which quality is over predicted due an overestimate in heat transfer coefficient. The 1-D heat transfer formulation used to calculate two phase heat transfer coefficient in the microgap assumed that heat only enters the microgap from one direction, its bottom surface. However quantification of power rejected into the microgap using the finite element model takes into account the heat flowing into the microgap from the side walls and the glass surface above it in addition to the bottom surface because in reality this is a 3-D problem. By not accounting for the surface areas of the side walls and glass surface, two phase heat transfer coefficient is over predicted 1-D analysis but still within reasonable approximation. Although the heat transfer coefficient is over predicted, the inaccuracy is not expected to be large and quality is expected to approach unity for the experimental heat fluxes tested.

5.2.3 Wall Temperature vs Microgap Heat Flux

The average wall temperature as a function of heat flux at the bottom surface of the microgap for mass fluxes up to 3,000 kg/m^{2}s for Gen 3 devices is shown in Fig.5.7. The two phase heat transfer coefficient calculated in eq. 5.5 is used to calculate the heat flux at the microgap surface according to Newton's law of cooling,

$$q" = h_{tp}\,(\overline{T_s} - T_{sat}) \tag{5.7}$$

Where $q"$ is the heat flux at the microgap surface. For all mass fluxes tested, the microgap wall temperature was stable and consistently in the range of 45-50ºC in the vapor plume regime. The wall temperature sharply increased at the transition to the liquid slug regime. Heat fluxes up to 1.5 kW/cm^2 were dissipated at the microgap surface at a temperature of 51 ºC. The ability to dissipate heat fluxes in excess of 1 kW/cm^2 at temperatures well below the standard operating limit of 85 ºC for electronic devices provides compelling evidence for use of extreme microgap based heat sink geometry as a solution for hotspot mitigation. While the device tested dissipated heater heat fluxes up to 4.6 kW/cm^2, a large fraction of the generated heat was lost by heat spreading through the silicon. The best indicator of the microgap heat sink performance in terms of heat fluxes it can dissipate are those presented in Fig. 5.7.

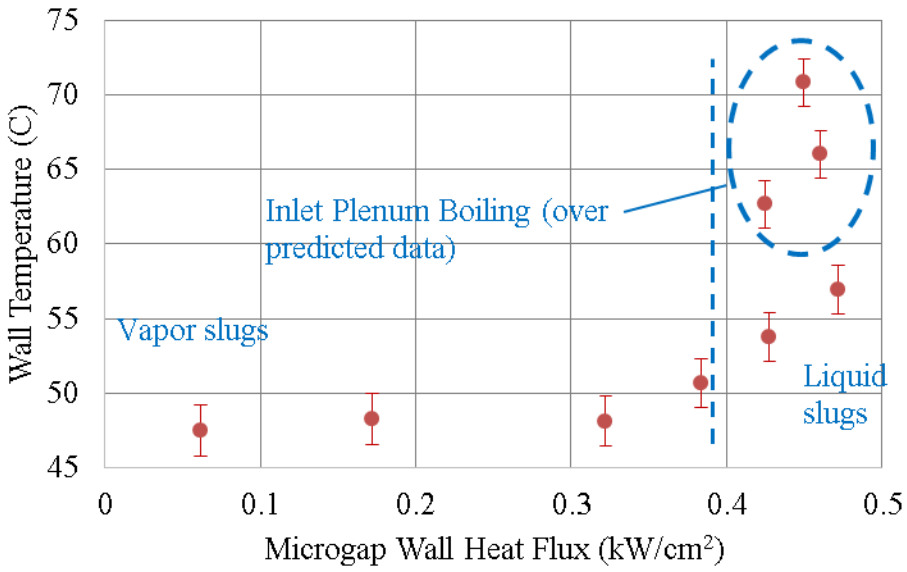

(a)

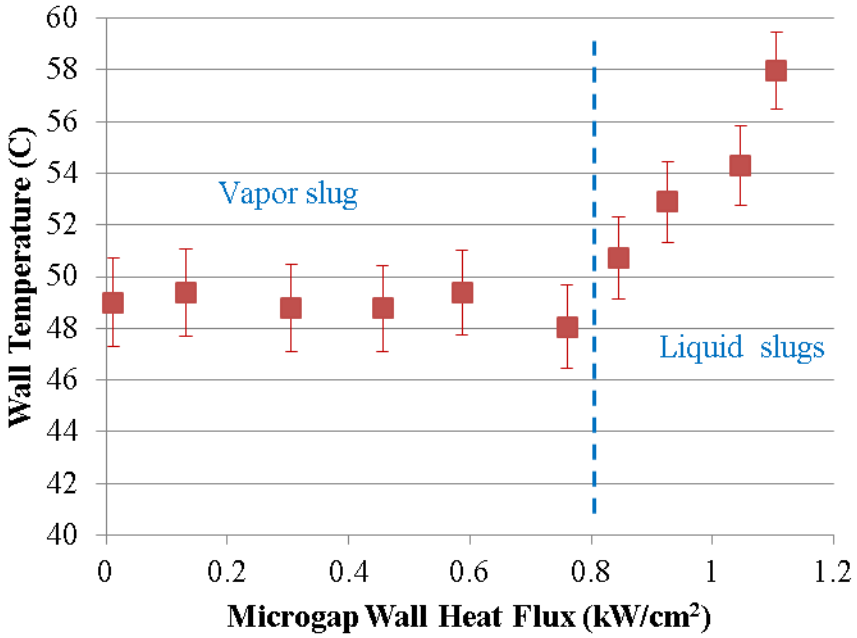
Wall Temperature (C)
60
58
56
54
52
50
48
46
44
42
40
Vapor slug
Liquid slugs
0
0.2
0.4
0.6
0.8
1
1.2
Microgap Wall Heat Flux (kW/cm²)

(b)

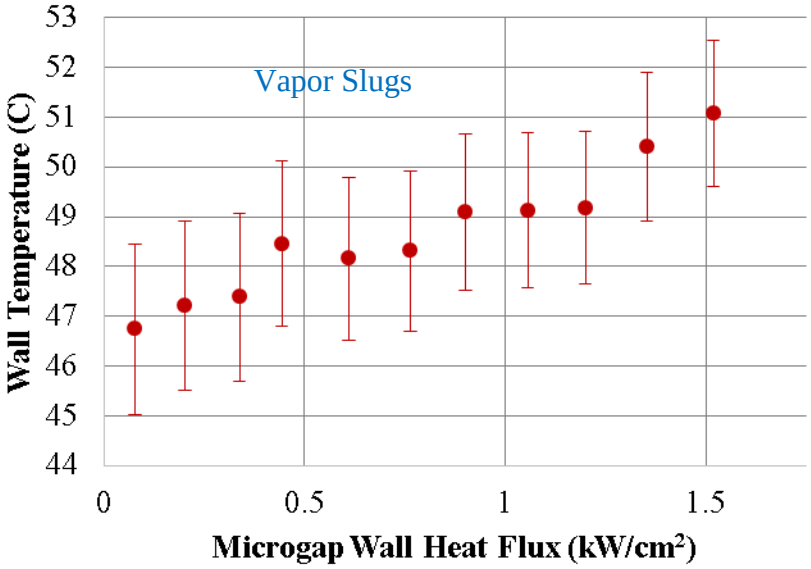
Wall Temperature (C)
53
52
51
50
49
48
47
46
45
44
Vapor Slugs
0
0.5
1
1.5
Microgap Wall Heat Flux (kW/cm²)

(c)

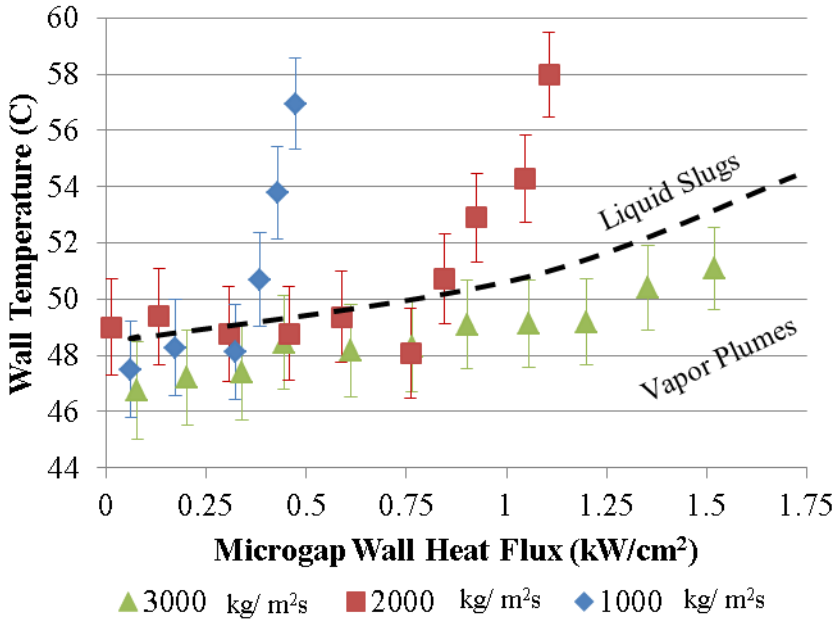

(d)

Fig. 5.7 Microgap wall temperature vs heat flux at the surface of the microgap for Gen 3 pin fin devices at: (a) 1,000 kg/m^{2}s, (b) 2,000 kg/m^{2}s (c) 3,000 kg/m^{2}s (d) all mass fluxes combined. Note: horizontal error bars on microgap heat flux are within ±0.1 kW/cm^2 for each and are removed for ease of visibility of data.

5.2.4 Flow Pattern Map

Figure 5.8 is a flow pattern map for Gen 3 devices reported in terms of mass flux as a function of quality. Over predicting two phase heat transfer coefficient lead to overestimate in quality. While meaningful predictions cannot be made for flow regime transitions based on the model inaccuracies, it is clear that quality did not decrease in the transition to the liquid slug domain as found in Gen 2 devices. A potential transition curve for the liquid slug regime is shown in Fig 5.8 . More data points with transition the liquid slug regime are needed to validate this proposed shape.

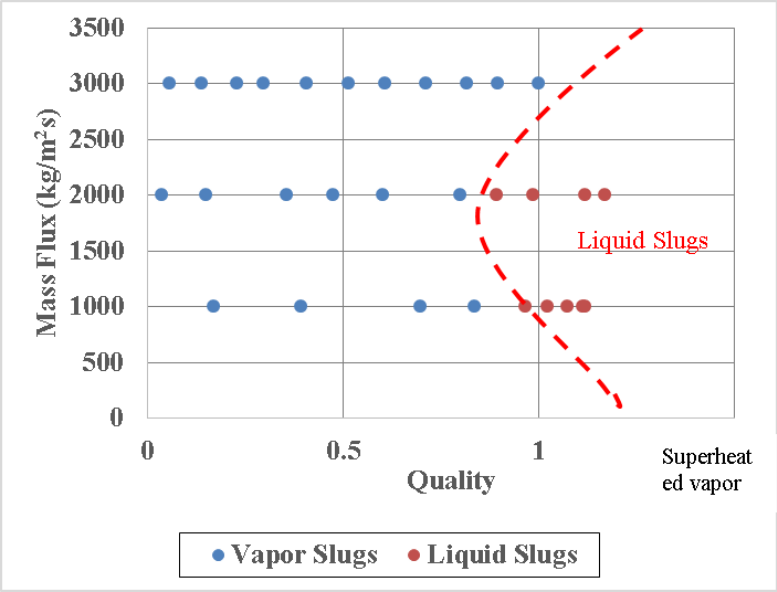

Fig. 5.8 Flow pattern map for Gen 3 devices

5.2.3 RTD Validation

A comparison between RTD temperature and model temperature as a function of heat flux for all modeled mass fluxes in Gen 3 device is presented in Fig 5.9.The model very closely approximated RTD temperature at low heater heat fluxes and deviated with increasing heat fluxes. The deviation between model and experiment is expected to occur for two reasons: first, the 1-D adiabatic fin analysis is known to over predict the overall two phase heat transfer coefficient in the microgap by not accounting for the surface area of side walls contributing to heat input to the microgap as discussed in section 5.2.2. Second, lateral variation in heat transfer coefficient was not accounted for in the model. Flow boiling visualization in Fig 5.5 shows that the transition of to the liquid slug regime occurred at the side walls of the microgap wall while the center remained in the vapor slug regime. This suggests that the local heat transfer coefficient near the side walls could be significantly lower than in the center of the microgap thereby raising RTD temperature above the value predicted by the model.

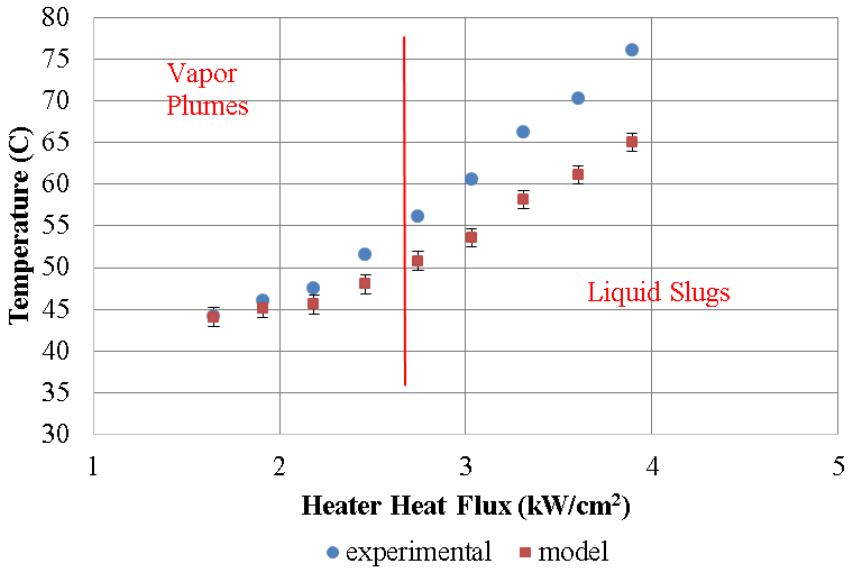
Vapor
Plumes
Liquid Slugs
Temperature (C)
Heater Heat Flux (kW/cm²)
experimental
model

(a)

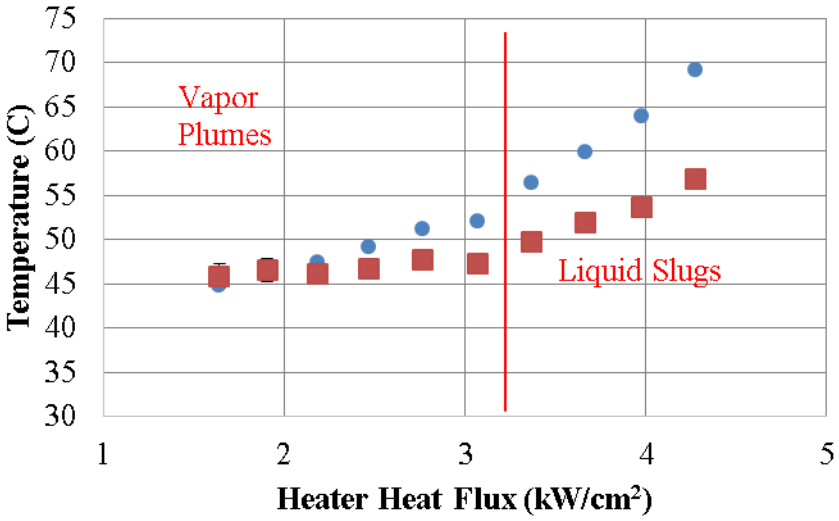
Vapor
Plumes
Liquid Slugs
Temperature (C)
Heater Heat Flux (kW/cm²)

(b)

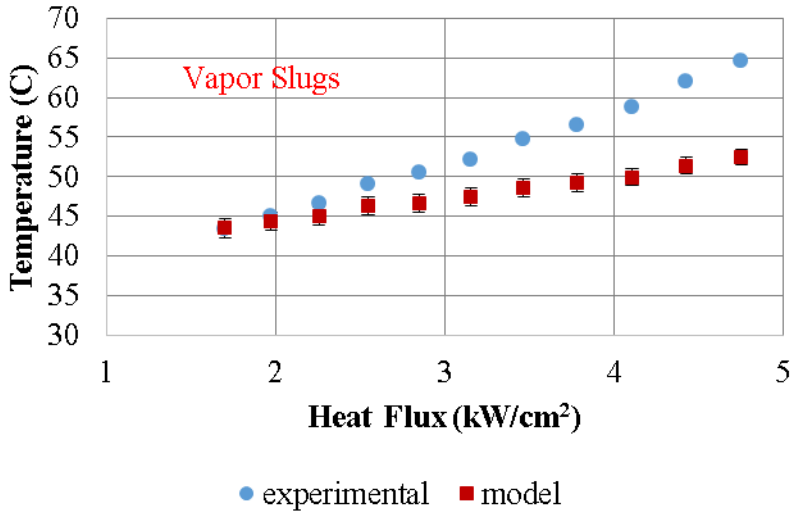

(c)

Fig. 5.9 Comparison between model temperatures at the location of the RTD and experimental temperatures for: (a) G=1,000 kg/m^{2}s experiment (b) G=2,000 kg/m^{2}s experiment (c) G=3,000 kg/m^{2}s experiment

5.3 Gen3 vs Gen 2 Performance

A plot of two-phase heat transfer coefficient as a function of heater heat flux for Gen 3 and Gen 2 devices at a mass flux of 3,000 kg/m^{2}s is shown in Fig. 5.10. Two heat transfer coefficients are presented for Gen 3 devices. The 'Gen 3 overall' heat transfer coefficient was calculated as the heat flux rejected to the microgap divided by the temperature difference between the microgap surface and coolant, without correcting for the surface area enhancement of the fins as done in Eq. 5.4-5.6. This heat transfer coefficient represents total heat rejection to the microgap, while the 'Gen 3 area correction' data points show the heat transfer coefficient with surface area correction as calculated according to Eq 5.4-5.6.

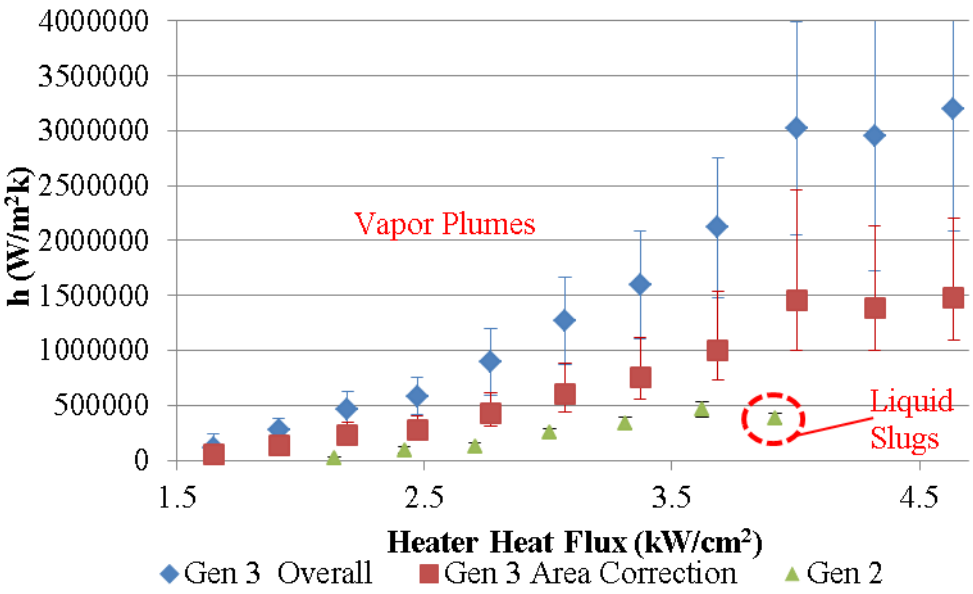

Fig. 5.10 Two-phase heat transfer coefficient vs heater heat flux between for Gen 2 and Gen 3 devices at 3,000 kg/m^{2}s. 'Gen 3 Overall' refers to an effective heat transfer coefficient which does not account for the surface area enhancement of the fins. 'Gen 3 Area Correction' refers to two phase heat transfer coefficient of the coolant.

Figure 5.10 shows that two phase heat transfer coefficient increased by ~ 3X with introduction of a dense array of fins in the microgap and up to 6X when the fin surface area enhancement is not accounted for. The data presented in Fig 5.10 was for the highest mass flux tested in each device (3,000 kg/m^{2}s) representing the maximum observed thermal performance. The key takeaway from this comparison is that the pin fins substantially increase heat rejection to the microgap not only by surface area enhancement, but also by increasing the coolant's two-phase heat transfer coefficient. By constantly interrupting hydrodynamic and thermal boundary layer growth, the pin fin enhanced microgap increases two phase heat transfer coefficient which is inversely proportional to the thermal boundary layer length. Additionally, recirculation zones

behind the fins which are advected by bulk flow in the microgap are expected to enhance heat transfer coefficient through better mixing of the coolant.

A comparison of pumping power as a function of heater heat fluxes for Gen2 and Gen 3 devices is shown in Fig 5.11. The improvement of thermal performance in Gen 3 devices comes at the cost of an order of magnitude increase in pumping power over the bare microgap Gen 2 device. This large increase in pumping power occurs due to fluid flow constriction resulting from tight spacing of the fins (10 μm apart) which increases pressure drop by an order of magnitude as was shown in section 3.4. Although the pumping power increased by an order of magnitude, the total power needed is less than 4 mW at the highest heat fluxes and the Coefficient of Performance (COP) values are in the range of 36-262 for Gen 3 device showing a strong overall performance. Gen 2 devices showed COP values in the range of 200-1800 due to the low pumping power required. COP was calculated as the ratio of heat dissipated by the microgap to the pumping power required.

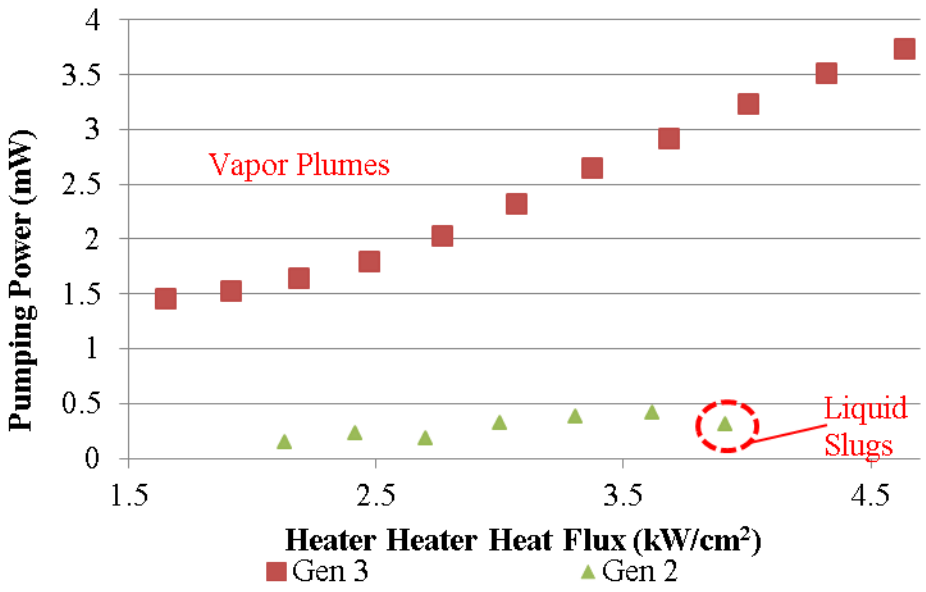

Fig. 5.11 Pumping power vs heater heat flux for Gen 2 and Gen 3 devices.

5.4 Comparison of Two Phase Heat Transfer Coefficient vs Quality to Literature

Two-phase heat transfer coefficients obtained in this study were compared to four published correlations, outlined in Table 5.1. Correlations 1-3, developed from flow boiling experiments in tubes, were compared to both bare microgap (Gen2 device) and pin fin devices (Gen 3 device). Correlation 4, developed for pin fin enhanced microgap boiling, has been additionally compared to the pin fin device.

Table 5.1 Two-phase heat transfer correlations

Correlation Number	Reference	Shape /Geometry	Working Fluid(s)	Correlation	MAE
1	Gungor-Winterton [36]	Saturated boiling in vertical and horizontal tubes	Water,R11 R12,R22, R113,R114, ethylene glycol	$h = h_l[1 + 3000Bo^{0.86} + \left(\frac{x}{1-x}\right)^{0.75}\left(\frac{\rho_l}{p_v}\right)^{0.41}$	Bare Microgap: 250% Pin fin Microgap: 189%
2	Kandlikar [10]	Saturated boiling in vertical and horizontal tubes D=0.19-2.92 mm G= 50-570 kg/m2s	R-113, R-141b, HCFC 123	For 100≤Re≤410 $h_{TP,NBD} = 0.6683Co^{-0.2}(1-x)^{0.8}h_{LO} + 1058Bo^{0.7}(1 - x)^{0.8}F_{Fl}h_{LO}$ $h_{TP,CBD} = 1.136Co^{-0.9}(1-x)^{0.8}h_{LO} + 667.2Bo^{0.7}(1 - x)^{0.8}F_{Fl}h_{LO}$ $h_{LO} = Nu\left(\frac{k}{D_h}\right)$ h_{TP} is the larger of $h_{TP,NBD}$ and $h_{TP,CBD}$	Bare Microgap: 255% Pin fin Microgap: 358%
3	Shah [37]	Saturated boiling in vertical and horizontal tubes	Water, R11, R12, R113, cyclohexane	$\psi = \frac{h_{TP}}{h_l} = f(Co, BO, Fr_{le})$ $N_s = Co\ if\ Fr_{le} \geq 0.04$ $Ns = 0.038Fr_{le}^{-0.3}Co\ if\ Fr_{le} \geq 0.04$ $F_{sh} = 14.7\ \ for\ Bo \geq 11x10^{-4}$ $F_{sh} = 15.4\ \ for\ Bo < 11x10^{-4}$ $\psi_{CBD} = 1.8N_s^{-0.8}$ For $N_s > 1$: $\psi_{NBD} = 230Bo^{0.5}$ for Bo>0.3x10^{-4} $\psi_{NBD} = 1 + 46Bo^{0.5}$ for Bo≤0.3x10^{-4} For $0.1 < N_s \leq 1$:	Bare Microgap: 91% Pin fin Microgap: 100%

Table 5.1 Continued

				$\psi_{BS} = F_{sh} Bo^{0.5} \exp(2.74 N_s^{-0.1})$ For $N_s \leq 0.1$: $\psi_{BS} = F_{sh} Bo^{0.5} \exp(2.74 N_s^{-0.15})$ ψ = greater of ψ_{CBD} and ψ_{NBD} or ψ_{BS}	
4	Krishnamurthy and Peles [38]	Rectangular microgap(1800 μm wide x 1cm long x250 μm deep) with circular, staggered pin fins G=346-794 kg/m2s $0<x_e<0.18$	Water	$h_{TP} = \zeta(\phi_l^2)^{0.2475} Pr^{0.333} h_{sp}$; $\zeta = 1$ $h_{sp} = Nu \left(\frac{k}{d}\right)$ $Nu = 0.76 \left(\frac{S_t}{d}\right)^{0.16} \left(\frac{S_l}{d}\right)^{0.2} \left(\frac{L}{d}\right)^{-0.11} Re^{0.33}$ $\phi_l^2 = 1 + \frac{0.24}{X_{vv}} + \frac{1}{X_{vv}^2}$ $X_{vv} = [(\Delta P_f/\Delta Z)_f/(\Delta P_f/\Delta Z)_v]$ $(\Delta P_f)_f = \frac{fN(G(1-x))^2}{2\rho_f}$ $(\Delta P_f)_v = \frac{fN(Gx)^2}{2\rho_v}$ $f = 63.246(Re_d)^{-0.7797}$	Bare Microgap: N/A Pin fin Microgap: 69%

Fig. 5.12 compares two-phase heat transfer coefficient as a function of quality at mass fluxes of 2,000 and 3,000 kg/m^{2}s in the bare microgap (Gen 2) device to correlations 1-3. Only data points within the vapor plume regime were presented to avoid modeling inaccuracy in the liquid slug regime due to boiling in the inlet plenum. It is clear that the Shah Correlation best predicted experimental two-phase heat transfer coefficients at the mass fluxes tested with an increasing level of accuracy at higher quality. The Kandlikar and G-W correlations tend to predict dry out at lower qualities than were experimentally observed at a mass flux of 2,000 kg/m^{2}s as indicated by a decrease in heat transfer coefficient shown in fig 5.12-a. Although the authors of the Kandlikar correlation suggest using the larger value of two-phase heat transfer coefficient between a correlation for nucleate boiling heat transfer and another for convective boiling heat transfer, we report the convective boiling heat transfer coefficient. The prediction of two-phase heat transfer coefficient based on convective boiling yielded better approximations to experimental values and is more consistent with boiling observations than the nucleate boiling heat transfer coefficient which was several times larger than the reported value.

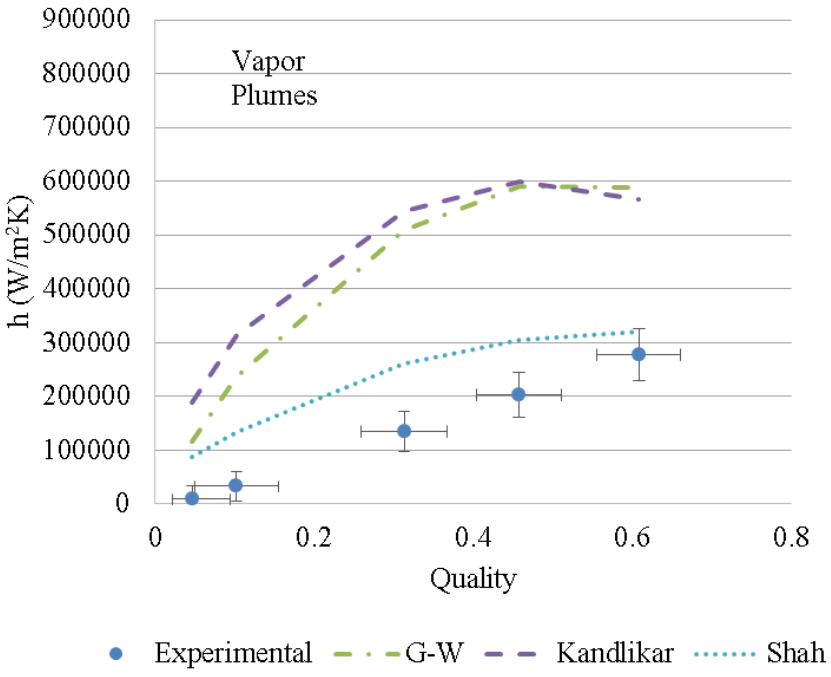
900000
800000
700000
600000
500000
400000
300000
200000
100000
0
h (W/m²K)
Vapor
Plumes
0
0.2
0.4
0.6
0.8
Quality
Experimental
G-W
Kandlikar
Shah

(a)

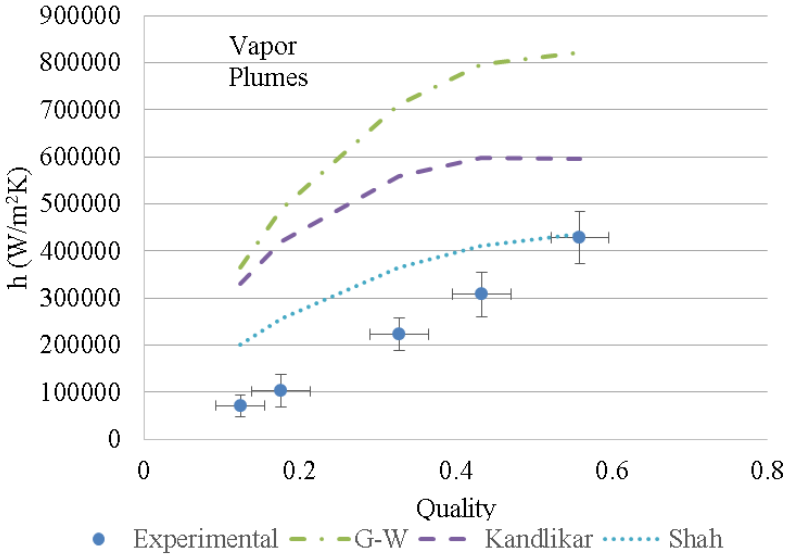
900000
800000
700000
600000
500000
400000
300000
200000
100000
0
h (W/m²K)
Vapor
Plumes
0
0.2
0.4
0.6
0.8
Quality
Experimental
G-W
Kandlikar
Shah

(b)

Fig 5.12**.** Comparison of two-phase heat transfer coefficient vs quality to correlations 1-3 in Table 2 at (a) 2,000 kg/m^{2}s (b) 3,000 kg/m^{2}s.

In general, correlations found in literature largely over predict two-phase heat transfer coefficient for the bare microgap device because the gap height tested (10 μm) is at least an order of magnitude smaller than the diameter for which the correlations were developed. This suggests that the rate at which two-phase heat transfer coefficient increases with decreasing gap height is lower at smaller gap heights. Furthermore, the correlations investigated tend to neglect the role of convective boiling dominant heat transfer in the microscale as we saw in the Kandlikar correlation. The Shah correlation, which performed best, predicted that the boiling mechanism corresponded to a bubble suppressed regime containing contributions from both nucleate and convective boiling. This suggests that correlations should be based on the dominant boiling mechanism observed.

Fig 5.13 compares two-phase heat transfer coefficient as a function of quality at mass fluxes up to 3,000 kg/m^{2}s in the pin fin microgap device to correlations 1-4. The Krishnamurthy and Peles correlation, developed for flow boiling of water in a staggered micro pin fin microgap, best captured the overall experimental trend in this study. The introduction of pin fins into the microgap impacts the boiling physics by interrupting thermal boundary layer growth and homogenizing coolant flow through recirculation zones, resulting in a monotonically increasing heat transfer coefficient as a function of quality which differs from the concave function predicted by bare microgap correlations. A limitation of the Krishnamurthy and Peles correlation is that the prediction of heat transfer coefficient asymptotically grows as quality approaches unity and therefore does not account for dryout. Furthermore, the experimental data shows a stronger dependence on mass flux than was predicted by the Krishnamurthy and Peles

correlation which over-predicted heat transfer coefficient at 1,000 kg/m^{2}s and under predicted results at 3,000 kg/m^{2}s.

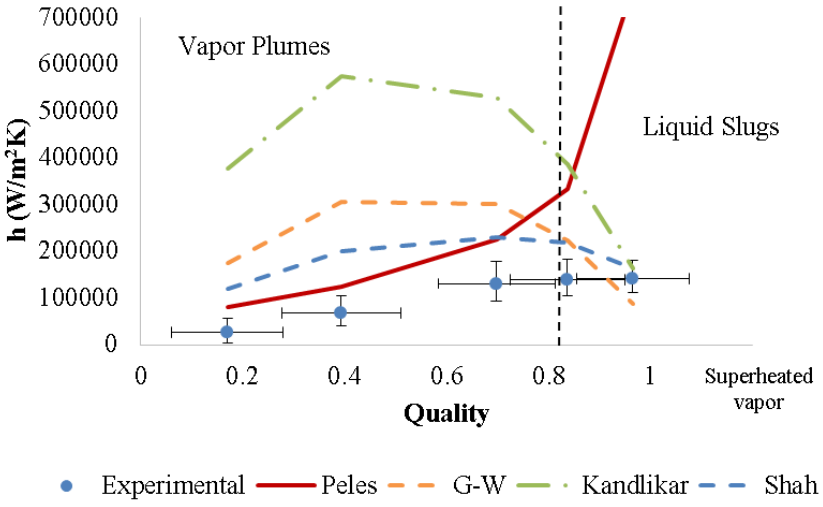

(a)

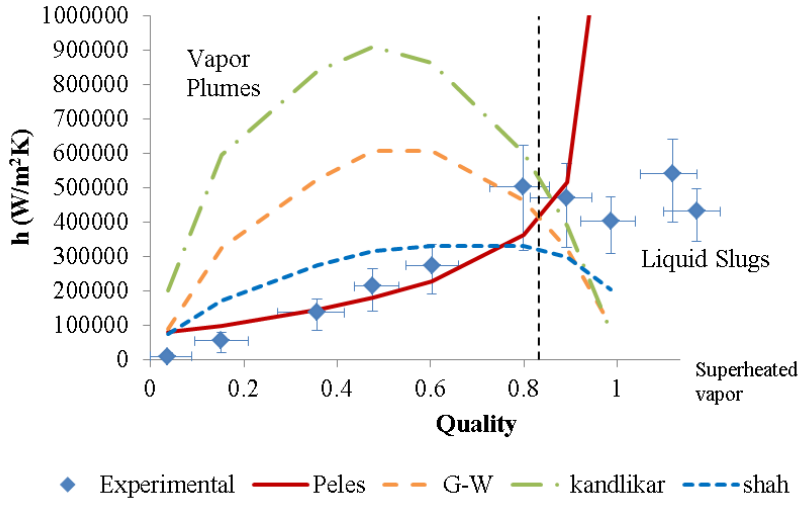

(b)

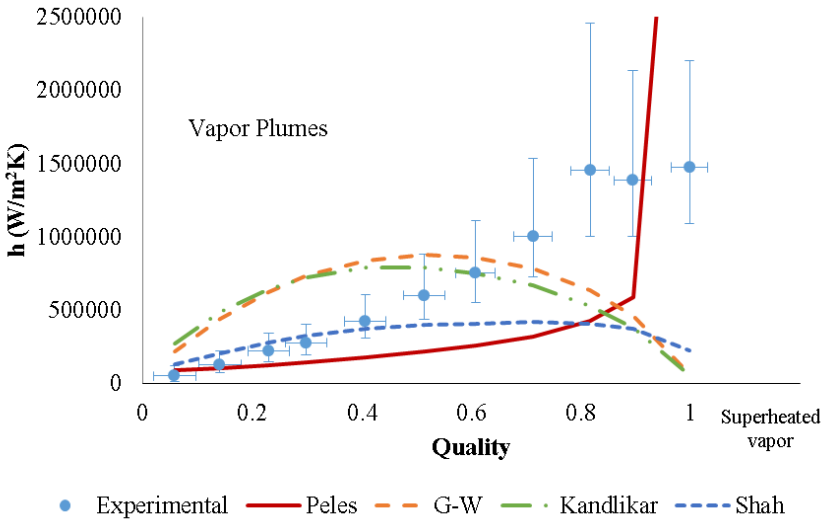

(c)

Fig 5.13. Comparison of two-phase heat transfer coefficient vs quality to correlations 1-4 in Table 2 at (a) 1,000 kg/m^{2}s (b) 2,000 kg/m^{2}s (c) 3,000 kg/m^{2}s.

5.5 Heat Spreading in Gen 2 and Gen 3 Devices

Heat spreading through various surfaces of Gen 2 and Gen 3 devices was investigated in simulations corresponding to experiments at 3,000 kg/m^{2}s (highest mass flux and best thermal performance) for several heat fluxes. The objective was to determine heat dissipated by the microgap and heat losses in the device/packaging. The surfaces measured for heat losses are highlighted in Fig. 5.14 and the heat leaving a surface was obtained by post processing simulation results. The heat dissipated by flow boiling in the microgap is shown in Fig 5.14-e. Heat leaving through the remaining surfaces of Fig 5.14 are losses. Note that even heat rejected to the coolant in the inlet and outlet plenums are considered losses.

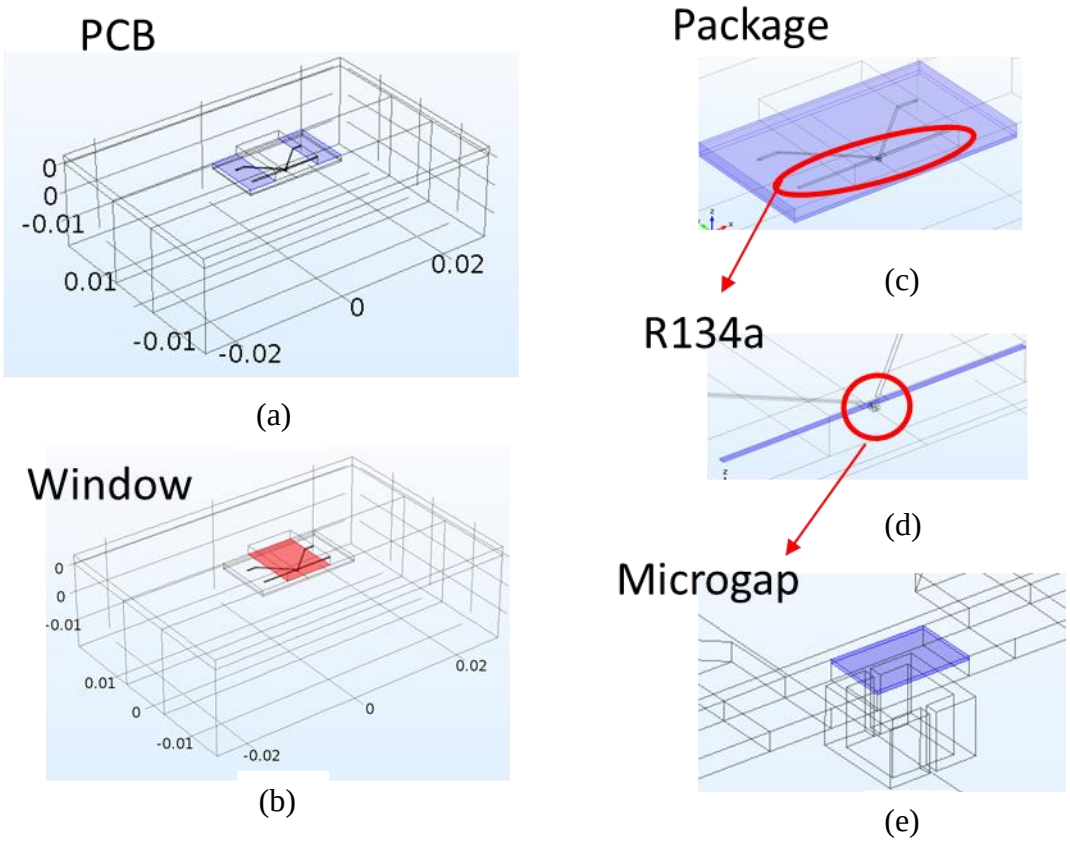

Fig. 5.14 Heat dissipated from various surfaces of computational domain: (a) Glass surface excluding visualization window (b) Glass surface used for flow visualization (c) Silicon sides and bottom (d) Microchannel surfaces (e) microgap surfaces.

Fig 5.15 shows the fraction of total power generated at the heater leaving the surfaces shown in Fig. 5.14 at several heat fluxes for the Gen 2 and Gen 3 device at 3,000 kg/m^{2}s. Heat rejected from the glass surface is divided into heat rejected to the PCB board (Fig. 5.14-a) and heat rejected to the ambient through the visualization window (Fig.5.14-b). Heat dissipated by the coolant is divided into heat dissipated by coolant in the microgap (Fig 5.14-e) and heat dissipated by coolant in the rest of the microchannel (Fig 5.14-d). Heat leaving the bottom and sides of the device (Fig5.14-c) are identified as package losses. In both devices the fraction of total power dissipated by the microgap increases with increases in heat flux because two-phase

heat transfer coefficient increases due to thinning of the liquid layer wetting the microgap surface. As the fraction of heat dissipated by the microgap increases, losses to the packaging and ambient are subsequently reduced with increases in heater heat flux. The coolant in the microgap dissipated a maximum of 37% of total power in the Gen 2 device and 53% of total power in the Gen 3 device. The Gen 3 device was able to dissipate a larger fraction of heater power than Gen 2 device due to the 4x increase in two-phase heat transfer coefficient over Gen 2 device. The largest source of heat losses came from heat rejected to the PCB and ambient through the glass surface of both devices.

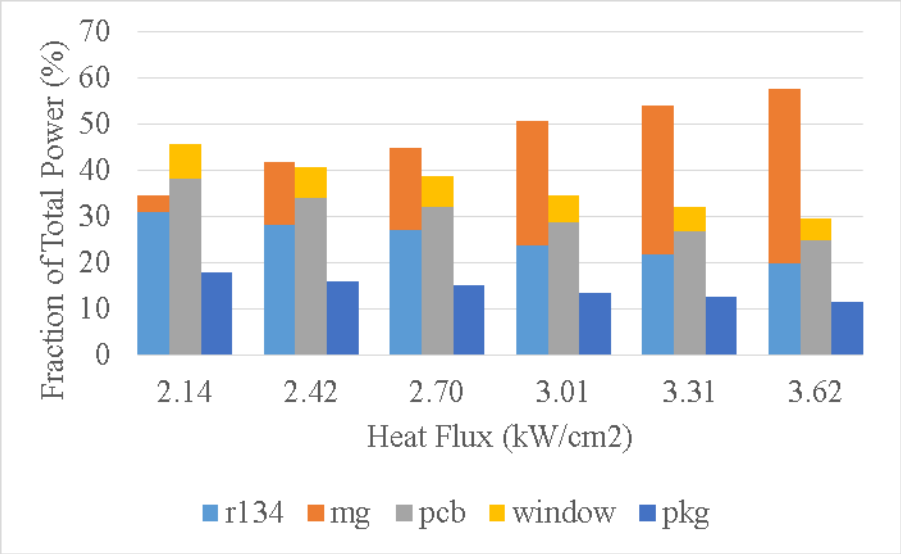

(a)

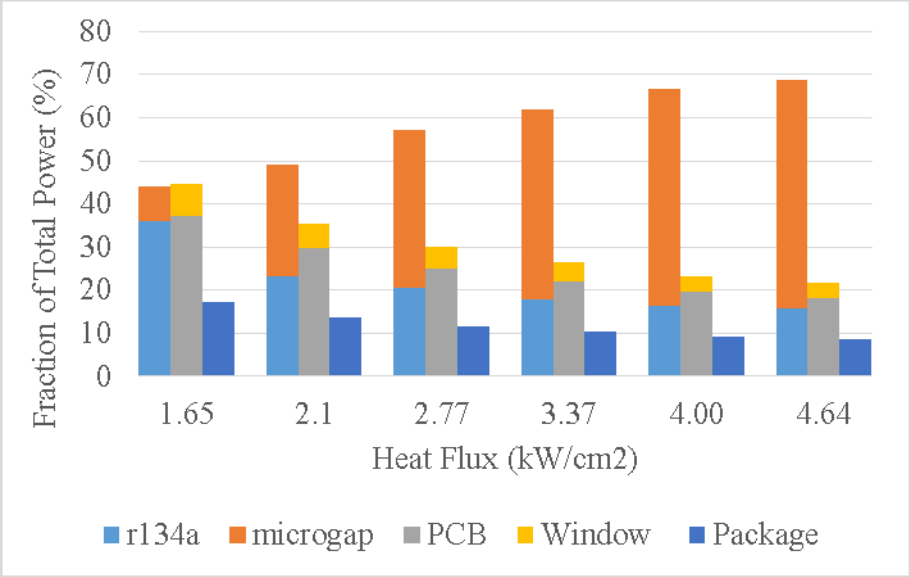

(b)

Fig. 5.15 Fraction of power leaving surfaces shown in Fig 5.14 for several heat fluxes at 3,000 kg/m^{2}s in: (a) Gen 2 device (b) Gen 3 Device.

Chapter 6

Conclusions & Future Work

An investigation of heat transfer performance of three dedicated microgap coolers for hotspot thermal management was presented in this work. The microgap coolers investigated exploited high heat removal rates by two phase convective boiling of refrigerant to dissipate ultra-high heat fluxes on the order of multiple kW/cm^2 targeting high power density computing application. An experimental system was built to pump subcooled R134a into the following microgap based heat sink devices:

- 'Gen 1 Device': 200 μm wide x 300 μm long x 5 μm tall microgap without pin fins. Device did not contain pressure ports or air trenches.
- 'Gen 2 Device': 200 μm wide x 300 μm long x 10 μm tall microgap device without pin fins. Included pressure ports to allow direct pressure measurement at the microgap inlet/outlet and air trenches to reduce heat spreading.
- 'Gen 3 Device': Identical to Gen 2 device in microgap, pressure port and air trench features with the addition of inline cylindrical pin fins in the microgap

Chapter 2 provided a comprehensive description of each device and presented the microfabrication process used to create them. Bosch process was used to batch fabricate each microgap device and provided high precision and accuracy features. The experimental closed loop system, with top-down flow visualization by microscope and integrated temperature and pressure sensors, was defined. Experimental procedures and uncertainties were also provided.

Chapter 3 presented the results of an experimental thermal characterization of the investigated devices in terms of overall device thermal resistance and pressure drop trends as a

function of heater heat flux. Heat transfer results, expressed in terms of overall thermal resistances within the devices, were mapped to flow regimes using high resolution optical visualization. All devices showed ability to dissipate ultra-high heat fluxes, up to 4 kW/cm^2 at the heater surface. Gen 1 devices with 5 μm gap height and no fins performed best in the ultra-thin film boiling regime with thermal resistances as low as ~0.045 cm^2-K/W. Conduction heat spreading in Gen 1 devices was reduced in Gen 2 and Gen 3 devices by introducing air isolation trenches around the heaters. Gen 2 devices with 10 μm gap and no fins showed a decreasing thermal resistance in the vapor plume regime and an increasing thermal resistance in the liquid slug regime due to reduced wetting of the heated surface. At mass fluxes below 3,000 kg/m^{2}s local dryout occurred in the liquid slug flow regime without an efficient thin film boiling regime that was observed at higher mass fluxes. Gen 3 devices, with a dense array of pin fins in a 10 um gap height, also showed decreasing thermal resistance in the vapor plume boiling regime. Thermal resistances increased in the liquid slug regime and no liquid film regime was observed, likely due to film disruption by the pins. Gen 3 devices showed only a 3.5% reduction in minimal thermal resistance compared to Gen 2 devices however the minimal resistance was reached at a significantly higher heat flux for high mass flux tests.

Pressure drop increased with onset of vapor slug boiling in the microgap for all devices. Flow instabilities observed in these devices were minimal and included infrequent flow reversals in the outlet plenum, boiling hysteresis in Gen 1 device, and vapor slug regime flash boiling in Gen 2 devices before transition to liquid slug regime.

Based on the experimental characterization performed, the following future work is recommended:

1. To obtain a broader understanding of the convective boiling mechanism in the extreme microgap geometry investigated and verify that observed flow boiling regimes and thermal resistance trends are not unique to the coolant tested, more coolants at a wider range of mass fluxes should be tested. The mass fluxes in Gen 3 devices were limited to an upper limit of 3,000 kg/m^2s due to the high saturation pressure of R134a, however other coolants that have shown potential for high heat removal performance with lower saturation pressures such as water or FC-72 could be used as alternatives to expand the tested range.
2. The inlet conditions of the coolant to the microgap should be varied to better understand its impact on thermal performance. Energy balance showed that the coolant entered the microgap at saturation conditions in Gen 2 (non-pin fin) devices and at subcooled condition in the Gen 3 (pin fin device). While this occurred solely due to the inlet pressure at the micrgap and heat supplied by the inlet plenum due to spreading, the coolant temperature can be controlled by introducing a heat sink or heat source upstream of the test section. Gen 2 devices showed lower overall thermal resistances at lower heat fluxes than Gen 3 devices for the same mass fluxes, likely due to a higher quality in Gen 2 devices resulting from the coolant entering the microgap at saturation temperature. It would be valuable to understand whether it is possible to shift trends in heat coefficient/ thermal resistance as a function of heater heat flux by varying coolant inlet conditions.
3. Air trench depth should be increased to further minimize heat spreading in the microgap. The air trench depth etched into the Silicon wafer in Gen 2 and Gen 3 devices is 180 μm but can be easily be extended up to 240 μm to further minimize heat spreading and bypass of the microgap. Pressure ports and air trenches should be added to Gen 1 devices

to better understand thermal performance in the ultra-thin wavy liquid film regime which may potentially have the highest heat removal rates of the tested devices. This would also allow development of a finite element model for estimating heat transfer coefficient and quality in the Gen 1 device with reasonable accuracy. An additional modification would be to apply background heaters to the hotspot device eliminating the need for air trenches and heat spreading mitigation. This would allow more practical microgap based cooling evaluation in an environment that is representative of an actual IC chip with multiple heat sources around the hotspot.

4. The Gen 1 device with 5 μm tall microgap and ultra-thin wavy liquid film boiling is still of high interest with potential to produce extremely high heat removal rates and considerably more room for thermal characterization work to be done. Local dryout was not observed in Gen 1 devices even at heat fluxes as high as 5 kW/cm^2. Although heat spreading is expected to be substantial due to the absence of air trenches, the heat transfer coefficient and quality should be quantified by making the modifications to the devices suggested in the previous point. In addition, optical methods should be employed to measure the ultra-thin wavy liquid film thickness and roughness and related to heat transfer coefficient and thermal resistance.
5. It was not clear whether the existence of a bubbly regime was linked to the surface roughness of the plenum in Gen 3 devices. The surface roughness of Gen 3 devices should be measured for consistency and more devices should be tested to better understand the potential existence of a bubbly flow regime in these devices.

In Chapter 4, a 3D steady state heat transfer model was developed in COMSOL to predict heat transfer coefficient and quality in the microgap for Gen 2 and Gen 3 devices. The geometry

modeled consisted of the entire package, PCB board and Gen 2 device. Volumetric heat generation loading conditions were applied at the heater layer, represented as a thermal resistance, to simulate experimental tests. Convective boundary conditions were applied to the microchannel walls to model convection in the microgap. A temperature distribution in the fluidic channel was assumed based on linear temperature variation along the channel, energy balance in the plenums, and saturated fluid in the microgap. Single phase convection was assumed in the inlet and outlet plenums. Two phase heat transfer coefficient was iteratively varied in the microgap until the model heater temperature converged on the experimentally measured value for each experiment performed within an uncertainty band of ±1.6ºC.

In chapter 5, the modeling results for Gen 2 and Gen 3 devices were presented. Trends in heat transfer coefficient as a function of heater heat flux and quality were found to increase in the vapor plume regime and decrease in the liquid slug regime due to the onset of local dryout. The model was found to be valid for all boiling points except for those at which boiling in the inlet plenum was observed. Since two-phase heat transfer coefficient was not included in the convective boundary condition of the inlet plenum due to the absence of an accurate prediction method, two phase heat transfer coefficient and quality in the microgap were expected to be over predicted. A 1-D adiabatic fin tip analysis in conjunction with Newton's law of cooling was used to calculate two phase heat transfer coefficient in Gen 3 devices to account for surface area enhancement of pin fins which were not included in the computational domain. Two phase heat transfer coefficients up to 450,000 W/m^2K and qualities up to 0.72 were found for Gen 2 devices. Two phase heat transfer coefficients up to 1,500,000 W/m^2K and qualities up to unity were found for Gen 3 devices. At the highest heat transfer coefficients of Gen 3 devices small variations in heater temperatures resulted in large variations in predicted heat transfer coefficient.

Two phase heat transfer coefficient in Gen3 devices increased by a factor of ~4 over Gen 2 devices due to thermal boundary layer interruption of the coolant by the pin fins. This improvement in thermal performance came at the cost of a 10x increase in inlet pressure of Gen3 device compared to Gen2. However, since the flow rates in both devices are very low the COPs are as high as 262 and 1,800 in Gen 3 and Gen 2 devices respectively.

Less heat is dissipated by spreading due to the large magnitude of heat transfer coefficients in Gen 3 device as compared to Gen 2 devices. Gen 3 devices were found to dissipate heat fluxes as high as 1.5 kW/cm^2 at the microgap surface at wall temperatures as low as 51°C. Validation of modeling results was done by comparing temperature of an RTD located orthogonal to the flow direction to the model temperature at the same location. The model showed strong agreement with the experimental temperature at low heat fluxes and began to deviate at higher heat fluxes. Local variation in two phase heat transfer coefficient evident in curved profile of flow boiling visualization, not accounted for in the modeling, was expected to factor into the modeling inaccuracy between the model and RTD.

Correlations found in literature for two-phase heat transfer coefficient as a function of quality generally over predicted experimental results for the Gen 2 device. The concave trend of experimental data was well captured by existing correlations however only the Shah correlation well approximated the magnitude. The Shah correlation was effective in predicting the experimentally observed two-phase heat transfer coefficient because a combination of nucleate and convective boiling terms was used in the correlation. Other correlations highly over predict two-phase heat transfer coefficient when only nucleate boiling terms are used. Both trend shape and magnitude of two–phase heat transfer coefficient in the Gen 3 devices were well captured by the Krishnamurthy and Peles correlation, which was developed for flow boiling of water in a pin

fin microgap. Correlations developed for a bare microgap with no fins did not capture the monotonic increase of two-phase heat transfer coefficient that was observed.

Overall thermal performance of microgap based heat sinks investigated in this thesis provides compelling evidence for their use as a powerful tool for hotspot thermal management. Heat transfer coefficients up to 1,500,000 W/m^2K in Gen 3 devices with heat fluxes as high as 1.5 kW/cm^2 dissipated at the microgap surface and qualities approaching unity. Heater heat fluxes as high as 4 kW/cm^2 were dissipated by each investigated device with very limited flow boiling instabilities. There is still much more to learn about extreme two-phase microgap based heat sinks and the purpose of this thesis was to better understand the fundamental physics of boiling and push the limits of the highest achievable thermal performance with this technology.

Appendix

A. Preparing Hotspot Device for Experiments

General Guidelines:

A. Always wear gloves when touching hotspot devices. Best to use tweezers for handling device as much as possible to avoid touching it.

B. Never touch the ports (inlet/outlet or pressure).

1. Examine wafer of batch fabricated hotspot devices using the Keyence microscope to find a suitable device to test. Carefully examine the microchannel/microgap of the devices under microscope to check for any defects or debris. If there are large defects from fabrication, choose a different sample. If dust or small particulates appear in the microgap/ channel they can often be removed by sonicating the device as explained in the step 3.
2. To detach a chosen device from the wafer, heat the blue tape with a heat gun until the tape easily peels off (usually takes 5-10s of heating). Keep the heat gun at a sufficiently far distance so that the heat is warm to the touch at the location of the tape.

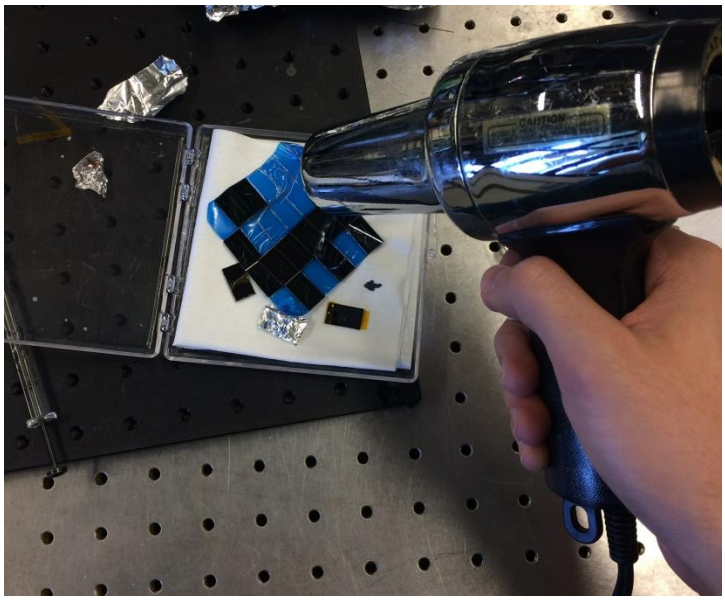

3. Sonicate the device for 10 mn in an acetone bath regardless of whether the channel is clean or dirty (instructions from fabricators of device). If you've observed any particulates in the device in step 1, then orient the device in the following tilted position when sonicating (dirty side down so gravity can assist in pushing it out):

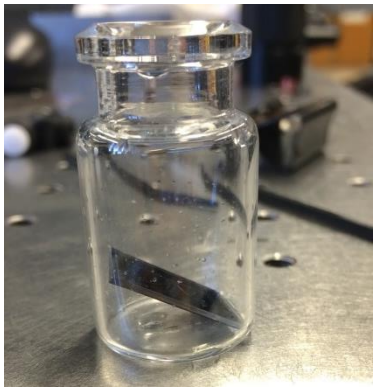

4. Re-examine the microchannel by microscope to make sure the channel is still clean. If there were initially particulates in the device carefully examine the entire channel to see if the particulates are gone. If the particulates have moved to a different location repeat step 2 as needed until the particulates have left the device.

5. Once the microchannel is clean (a good device will have no particulates anywhere in the device) and ready for tests, cover the inlet/outlet and pressure ports of the device with double sided tape so that no particulates enter the channel during the remaining preparation steps.
6. Attach the hotspot device to the PCB by placing two rectangular pieces of double sided tape on either side of the visualization window in the PCB as shown

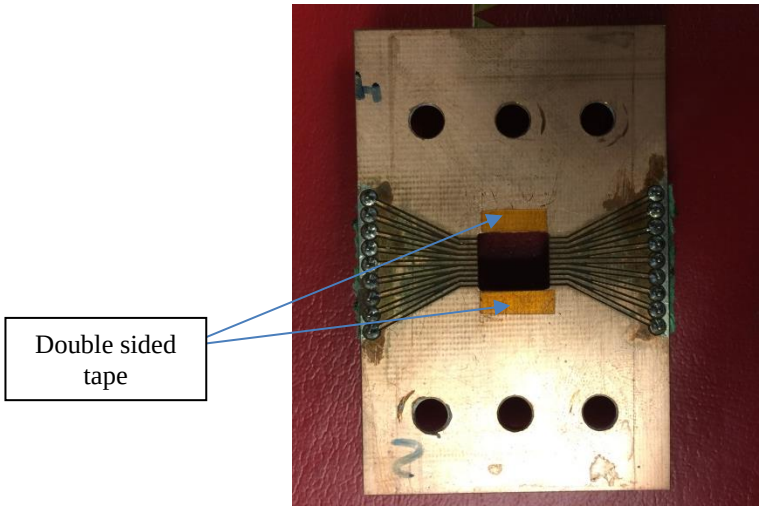

Press the hotspot device onto the double sided tape firmly for ~1 mn with the microchannel facing down. Align the platinum electrical pads to the PCB electrical paths as closely as possible on both sides. This is important to ensure that all pads can be easily wire bonded and that the device is best aligned with the ports in the package to avoid leaking.

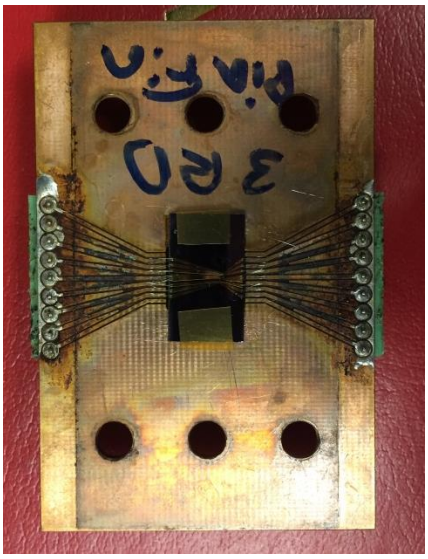

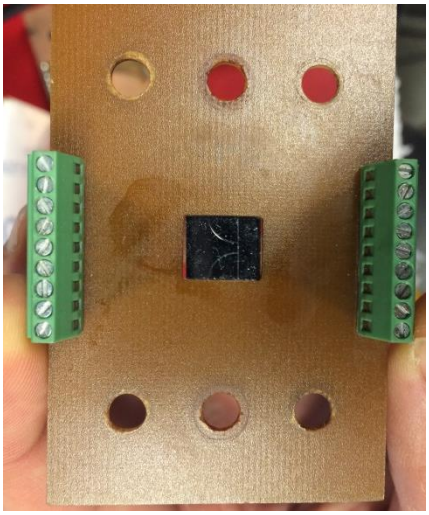

7. Wire bond the device with two bonds per pad for RTDs and three bonds per pad for heaters.
8. Obtain a linear calibration or temperature as a function of resistance for each heater and RTD using the following steps:
    a. Tape a wire thermocouple (WTC) to the hotspot device and PCB. Make sure the tip of the thermocouple is firmly pressed onto the surface of the device because when placed in the oven, parts of the tape will come off and if the WTC tip is not touching the device the calibration will be inaccurate.

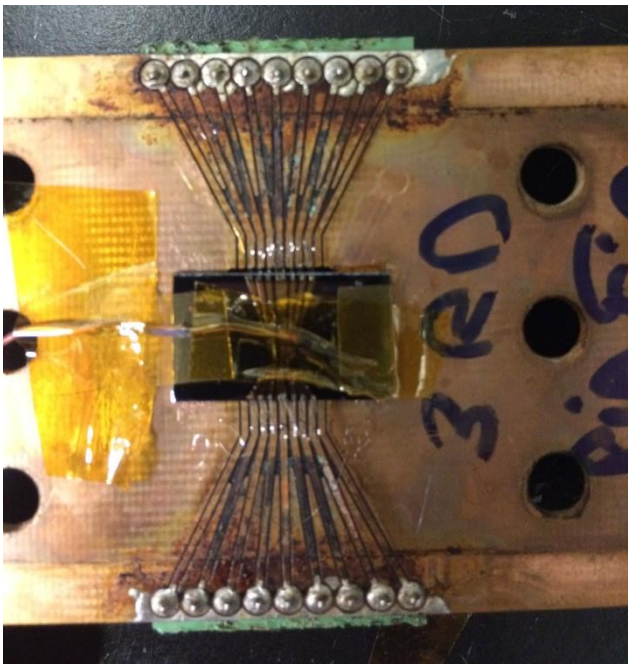

b. Connect the PCB to the national instruments data acquisition (NIDAQ) circuit board using wires going from the screw terminals (on the PCB) to the breadboard (shown below) and from the breadboard to the NIDAQ. Connect the WTC to channel 12 of the NIDAQ circuit board. Additionally, remove the power source wires.

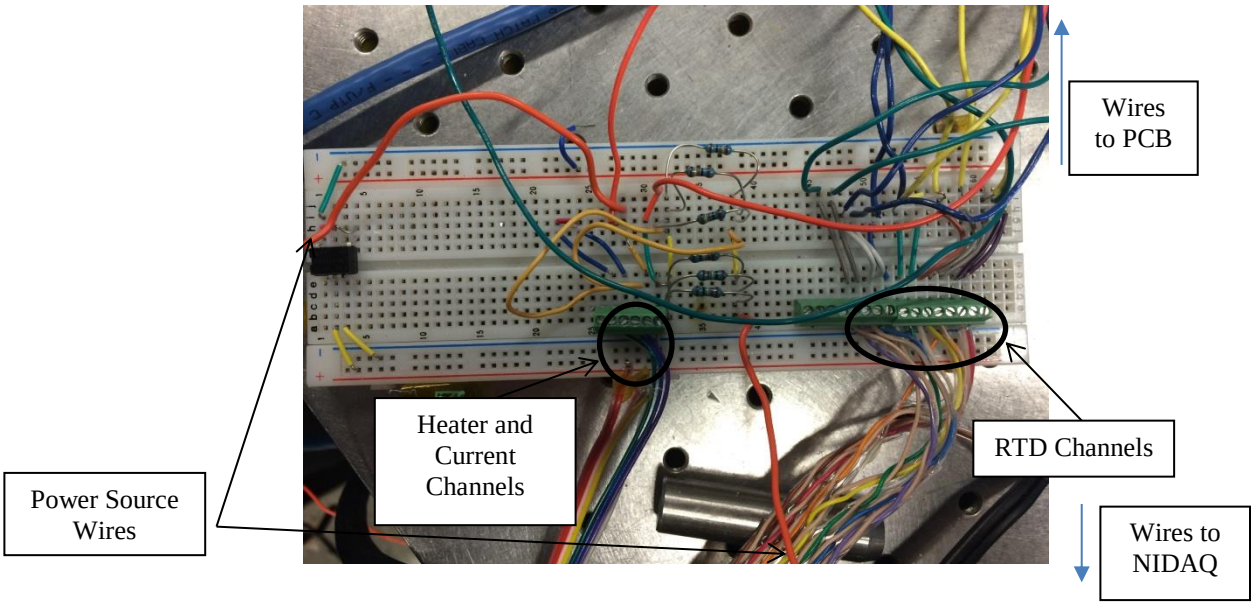

c. Take the NIDAQ circuit board out of the NIDAQ device and unscrew the wires connecting the pressure transducers to the NIDAQ board.

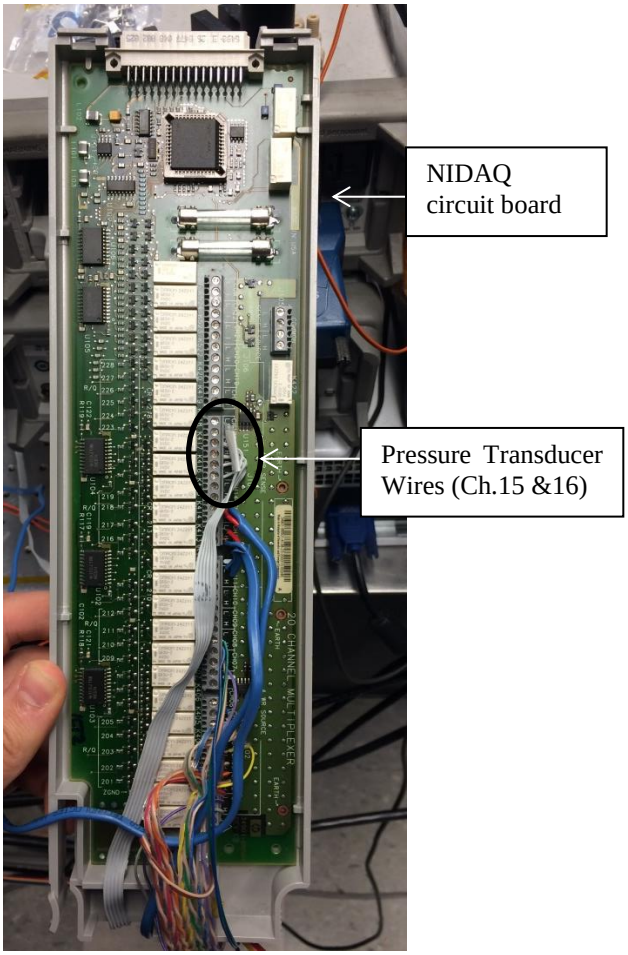

d. Set the oven to the desired calibration temperature (recommended temperatures are 200, 160, 120, 90, 60°C). It may take the oven up to an hour or longer to reach set temperature. Beyond 200C the wires and PCB melt quickly.

e. Once the oven has reached the set temperature, connect the NIDAQ circuit board to the NIDAQ next to the oven. Use the Benchlink data Logger program on the calibration computer to monitor resistance and temperature of the device. Make sure to use the calibration "2nd gen calibration nasr" and note that the channel numbers correspond to the wiring on the circuit board.

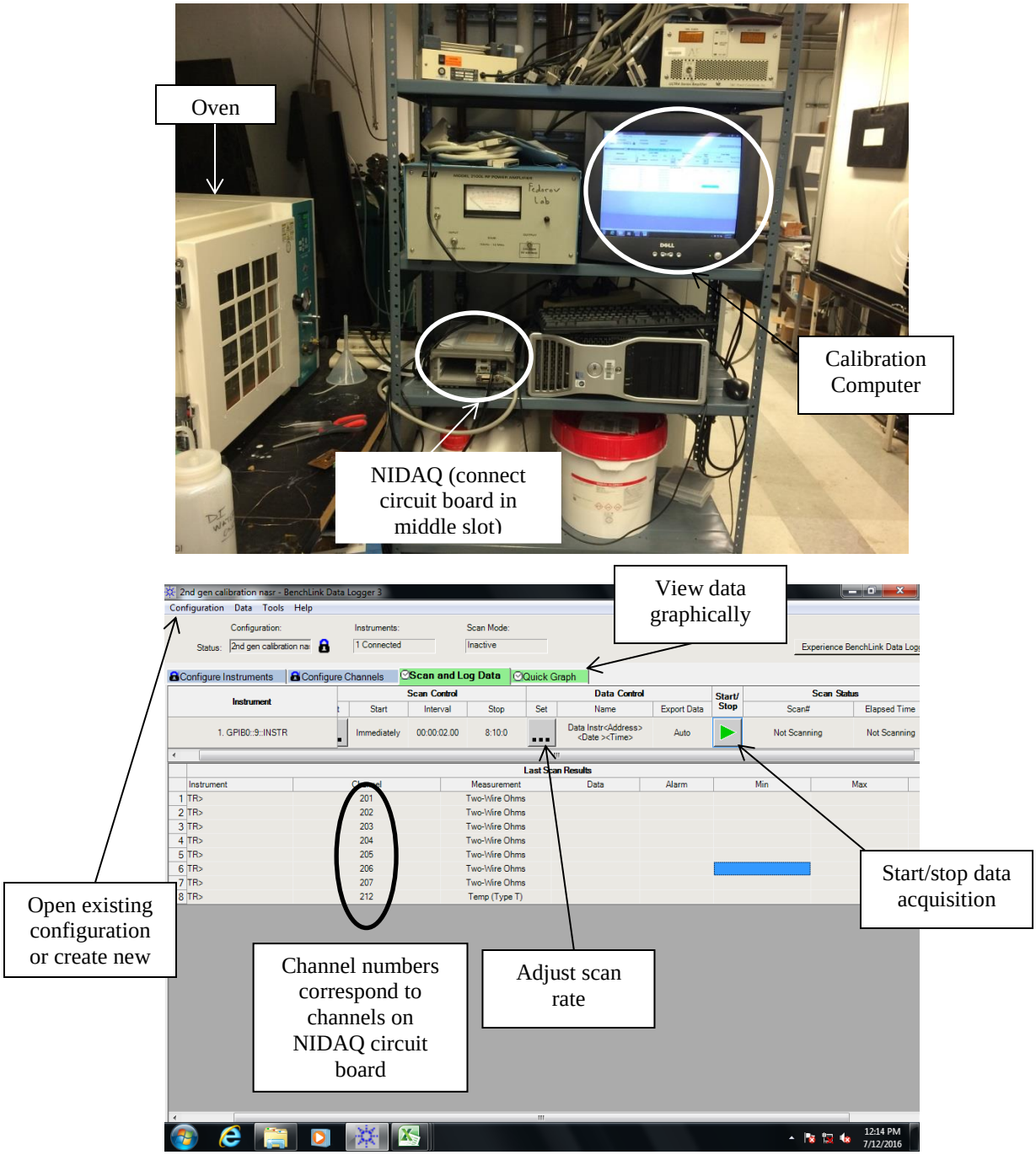

place the PCB and hotspot device in the oven. Monitor the temperature of the hotspot device using the NIDAQ. Once the hotspot device temperature has reached steady state (usually takes 15-20mn) obtain 10-15 data points of heater/RTD resistance and device temperature.

f. Take the hotspot device out of the oven and set the oven to the next calibration temperature. Do not keep the device in the oven for longer than 20-25 mn at high temperatures (>120C) to avoid melting the PCB.

g. Repeat the process for the remaining calibration temperatures. It is recommended to start from the highest temperature and work down to the lowest temperature.

h. Obtain a linear fit of temperature as a function of heater temperature for each RTD and heater using collected data.

Heater Calibration

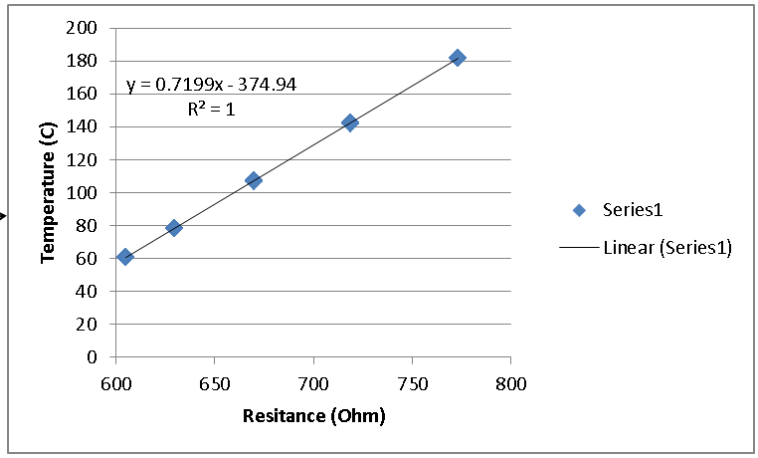

RTD calibrations

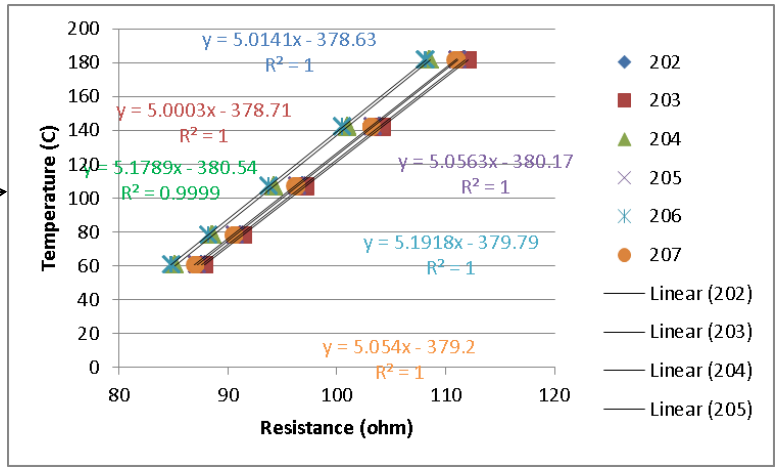

9. Remove TC and double sided tape covering hotspot device ports. Attach PCB and hotspot device to package using screws and nuts. Make sure the ports of the hotspot device are centered with the package O-ring groves so that the device hermetically seals.

10.

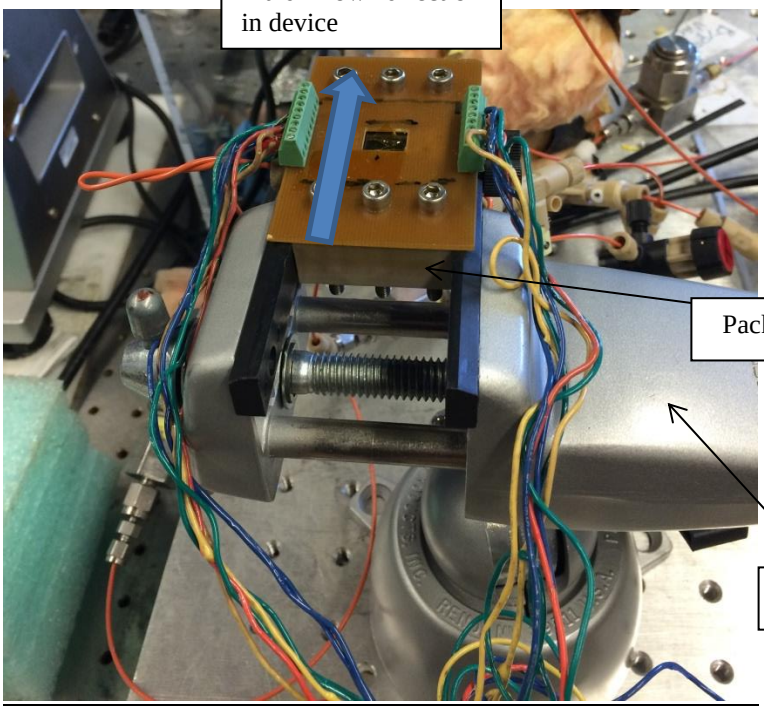
Fluid flow direction in device
Package
Clamp

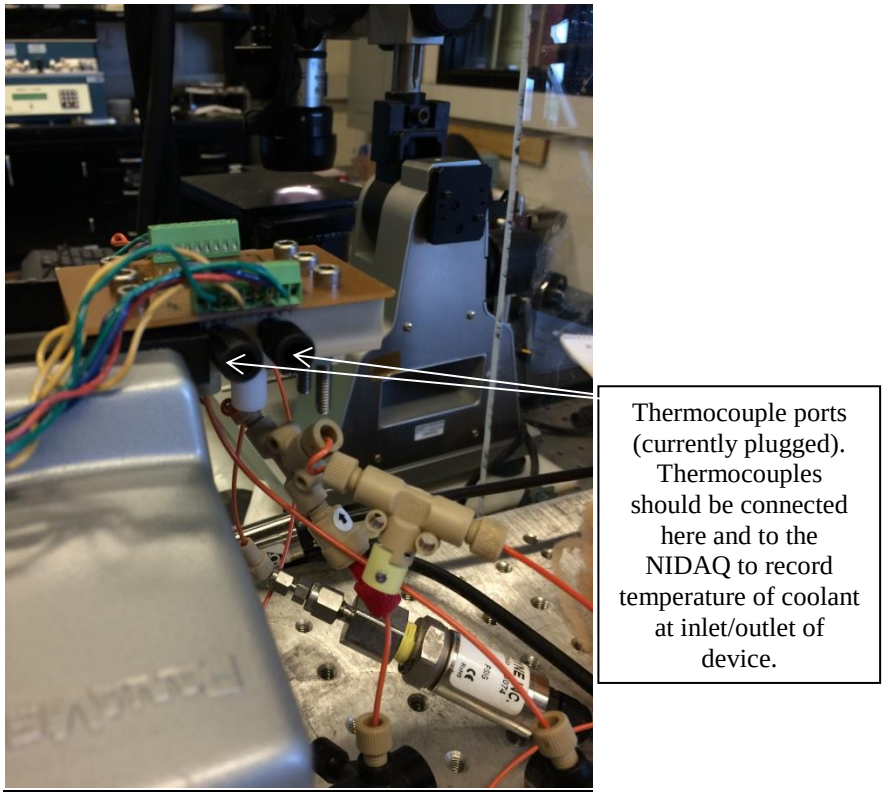
Thermocouple ports (currently plugged). Thermocouples should be connected here and to the NIDAQ to record temperature of coolant at inlet/outlet of device.

B. Work Station

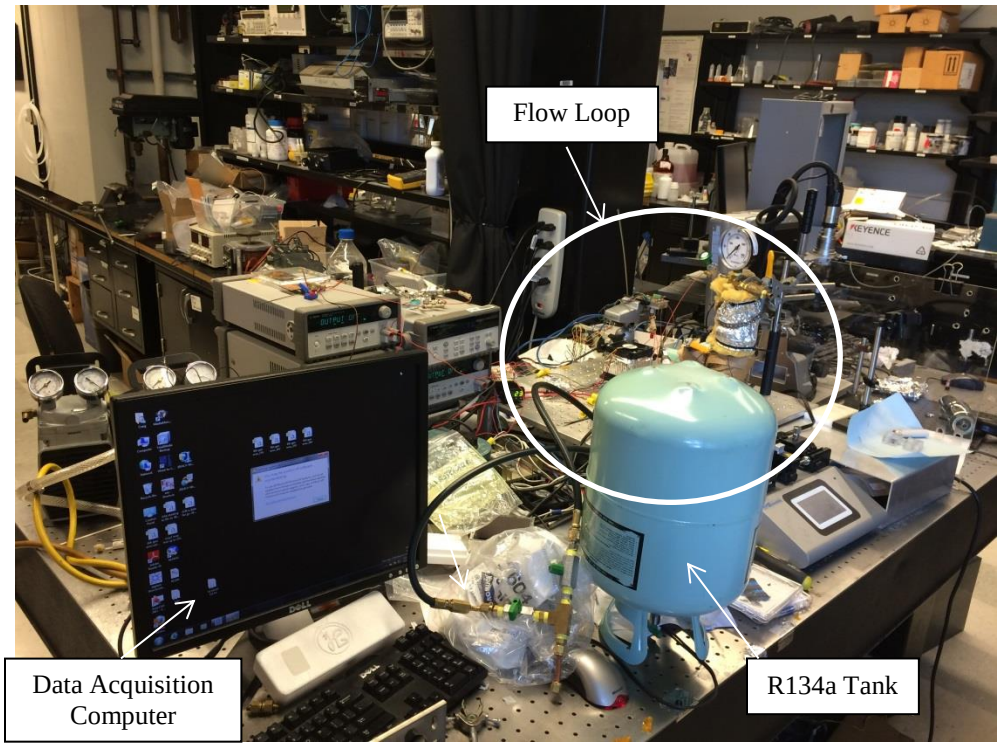

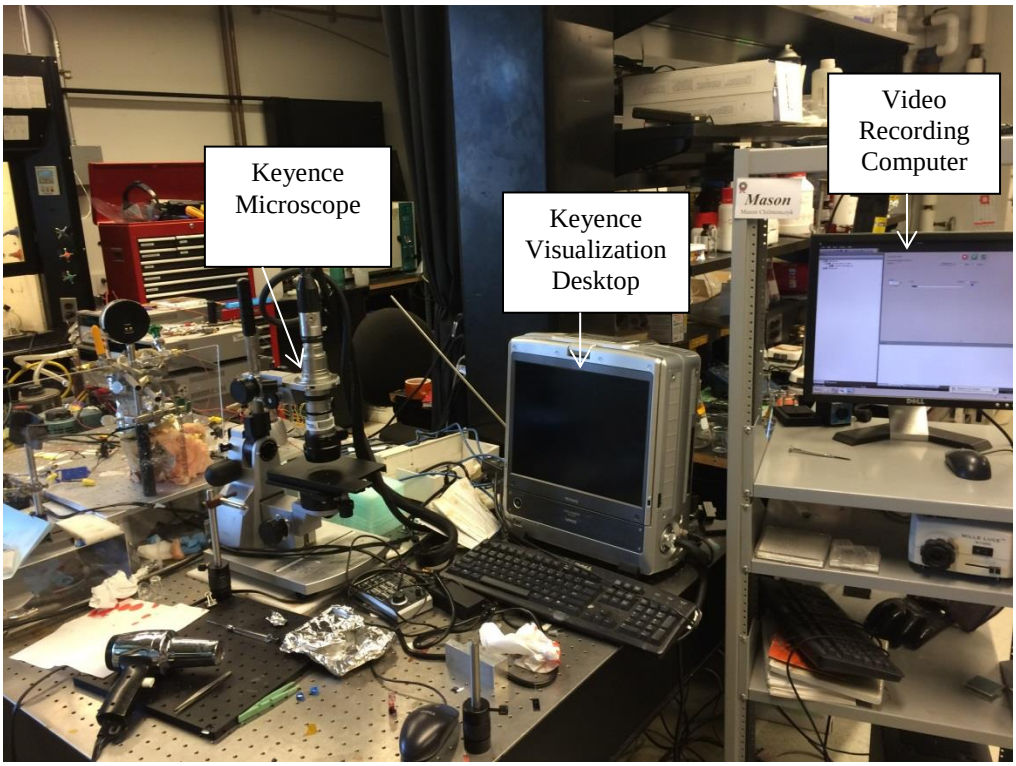

C. System Configuration

Two Types: One Syringe (Limited Pumping) or Two Syringes (Continuous Pumping)

<u>One Syringe</u>:

Advantage: more robust than two-syringe continuous pumping, which requires more piping and valves which frequently entrap air bubbles.

Disadvantage: Limited pumping time per infusion. Infusion time depends on flow rate and syringe volume.

System Setup:

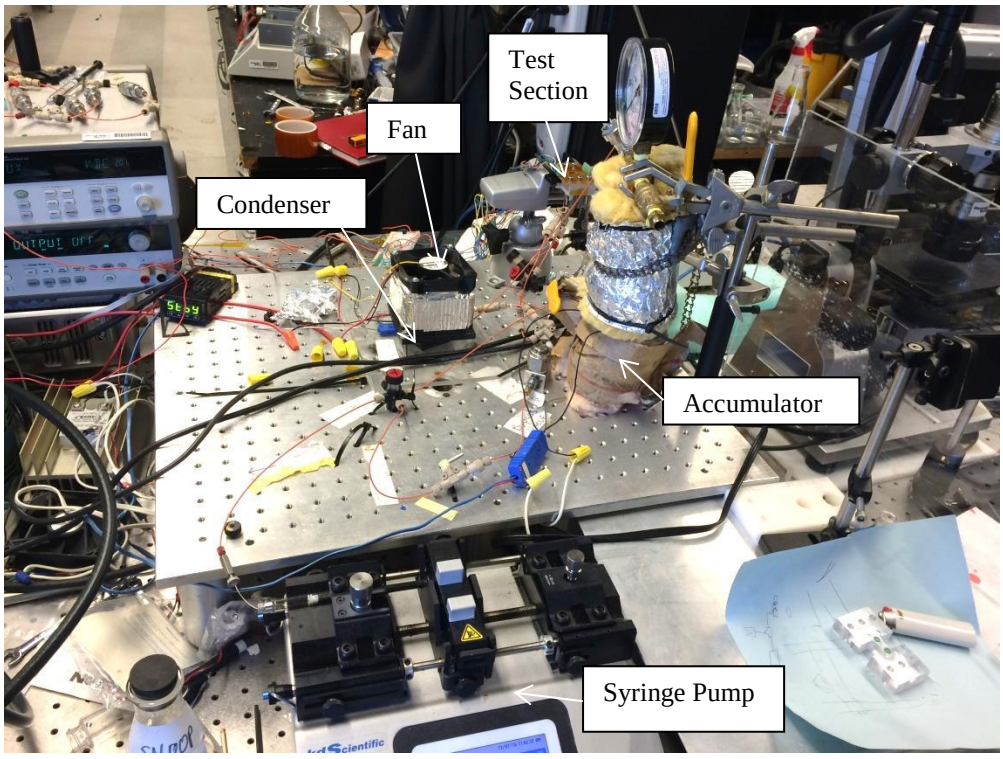

To withdraw coolant from accumulator into the syringe, arrange T-valve as shown below. To infuse coolant to the test section rotate-valve head 90° CCW before turning on pump.

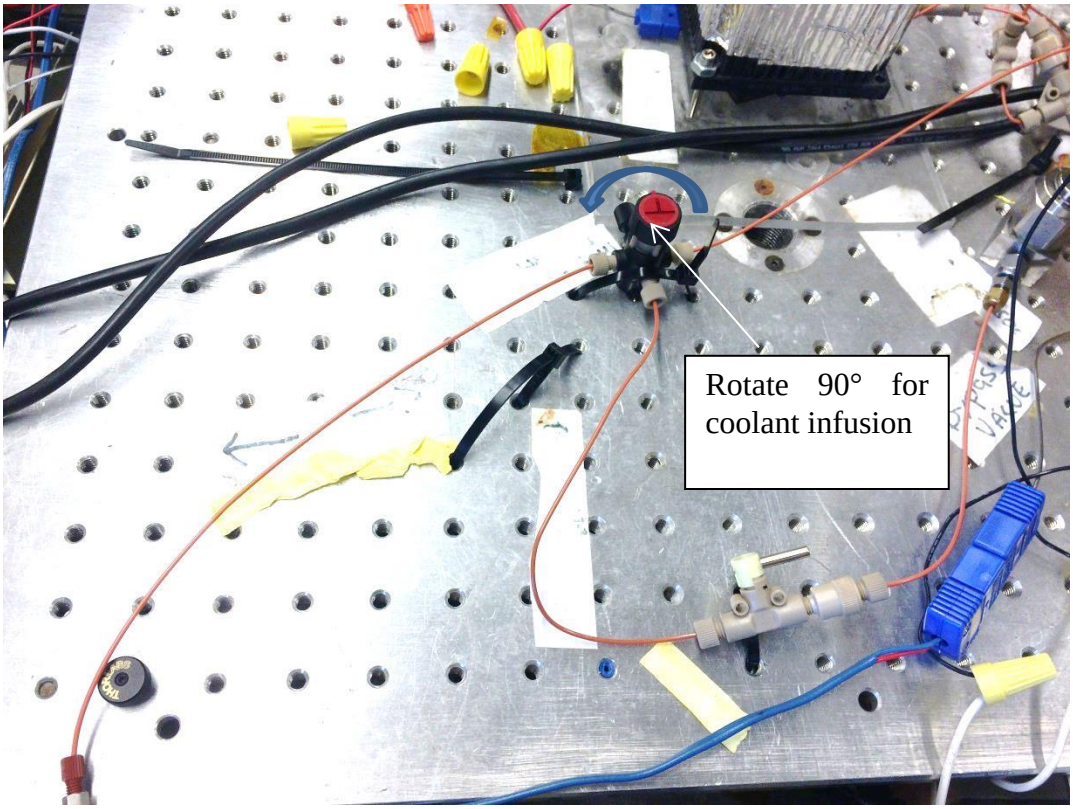

Two Syringes:

Advantage: Allows continuous pumping.

Disadvantage: Air in the system will eliminate the continuous pumping advantage and usually results in only one syringe infusing liquid into the test section while the other compresses or expands a bubble.

System Setup:

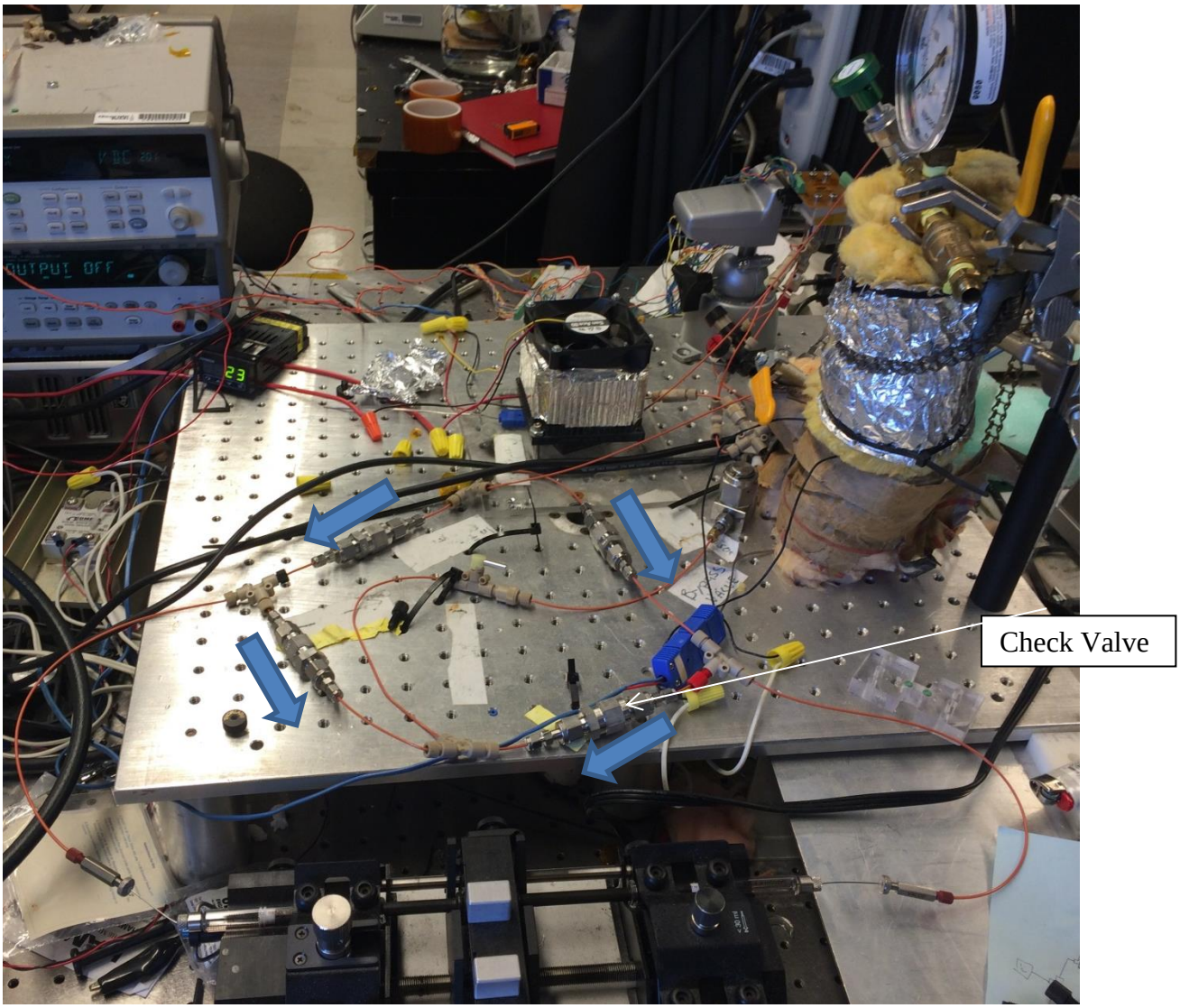

Orient the check valves such that the arrows on the valves are aligned with the blow arrows shown above to ensure fluid is continuously infused into the test section.

D. Leak Test

1. Once test section is sealed, attach air hose to accumulator as shown below.

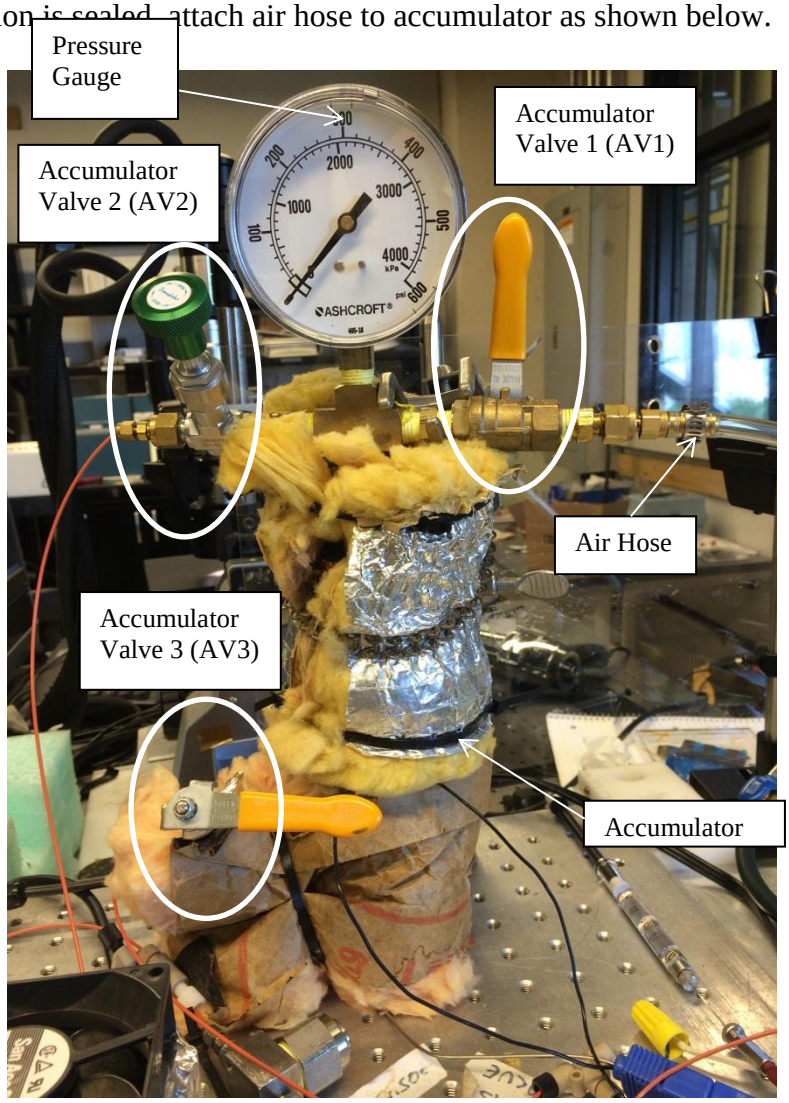

2. Open AV1, AV2 and AV3 to allow air to flow through the entire system. Make sure the test section is also open to air flow by configuring T-valves as shown below.

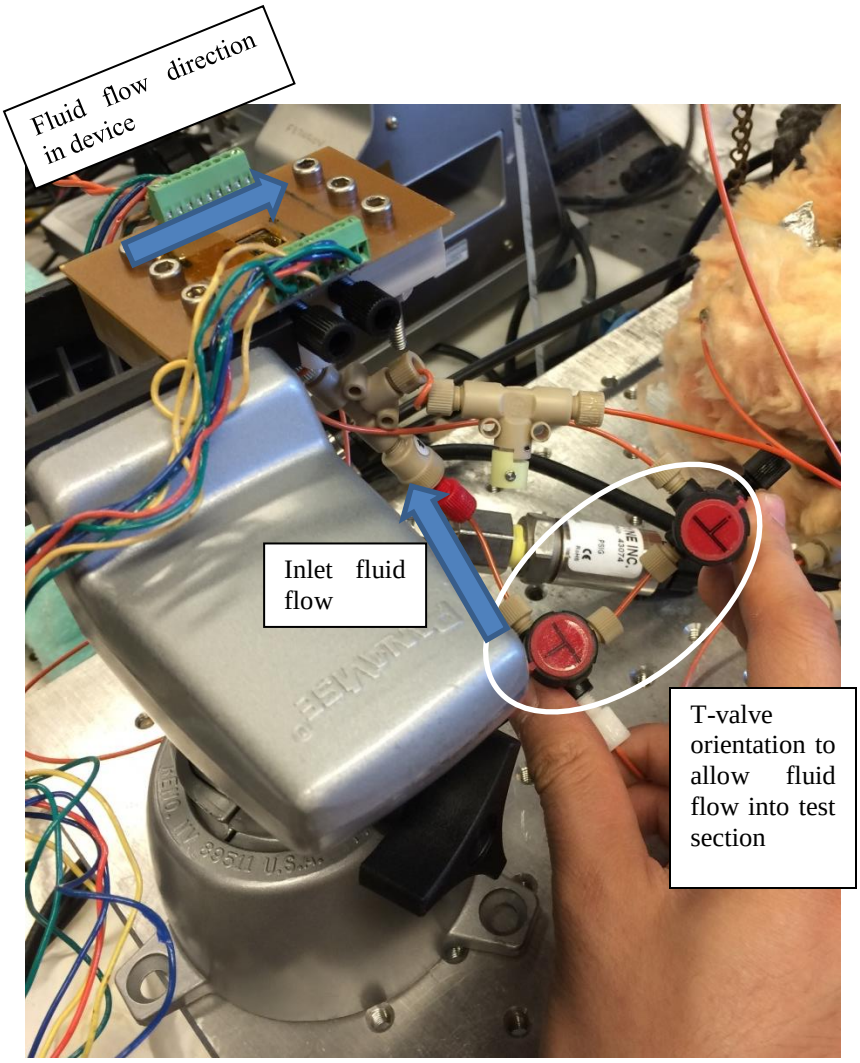

3. Connect the pressure transducers to the NIDAQ circuit board (channels 15 &16) as shown in step 8-c of the "Preparing Hotspot Device for Experiments" section and put the circuit board in the NIDAQ.
4. Apply +/- 12V power to the pressure transducers with the power source shown below.

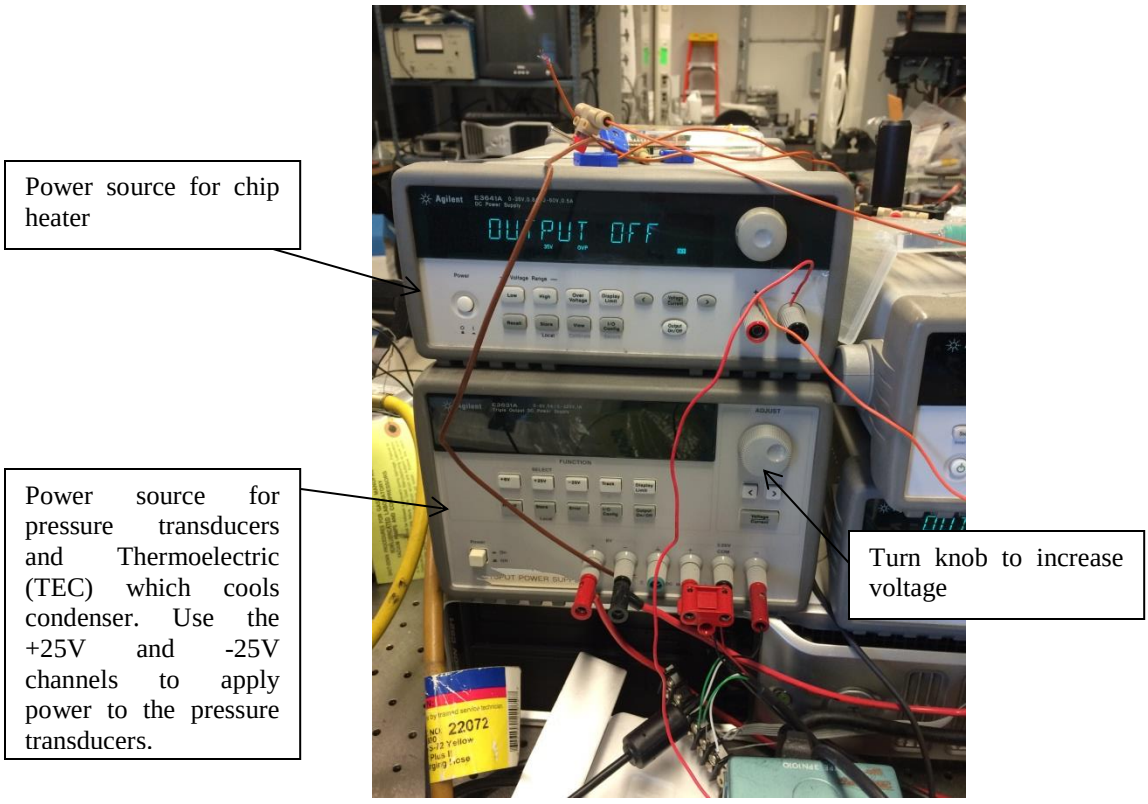

5. Turn on air flow and increase air pressure until the pressure gauge on the accumulator reads 1000 kPa or higher.
6. Close AV1 and turn off air flow.
7. Monitor pressure gauge and pressure transducer readings on NIDAQ through the Bench link Data logger program on Data Acquisition Computer (shown in "work station" section) to make sure the pressure does not decrease.
8. If pressure is decreasing systematically apply SNOOP to compression fittings with syringe to determine leak source.
9. The most likely source of leaking is the test section/package. Check inlet / outlet fluid piping to the package, pressure transducer ports and chip sealing thoroughly. Pressure transducers should read steady static pressure during leak test. Make sure the system can

hold static air pressure up to 1000 kPa for up to 30mn before charging the system with refrigerant.

10. If a leak is found tighten loose compression fittings (sometimes they may need to be replaced). If package is not able to hold pressure check to see that the hotspot device ports are properly aligned with O-ring grooves in package. Pressure port and fluid port piping need to be very tightly attached to package.

E. Evacuating Experimental System

After system has been checked for leaks evacuate the system as follows

1. Open Agilent Benchlink Data Logger on DAQ computer.
2. Attach copper tubing to accumulator as shown below. Open AV1, AV2 and AV3. Make sure T-valves are configured such that the system can be evacuated as shown in step 2 of "Leak Test" section. Additionally, open the valves on the hose shown below.

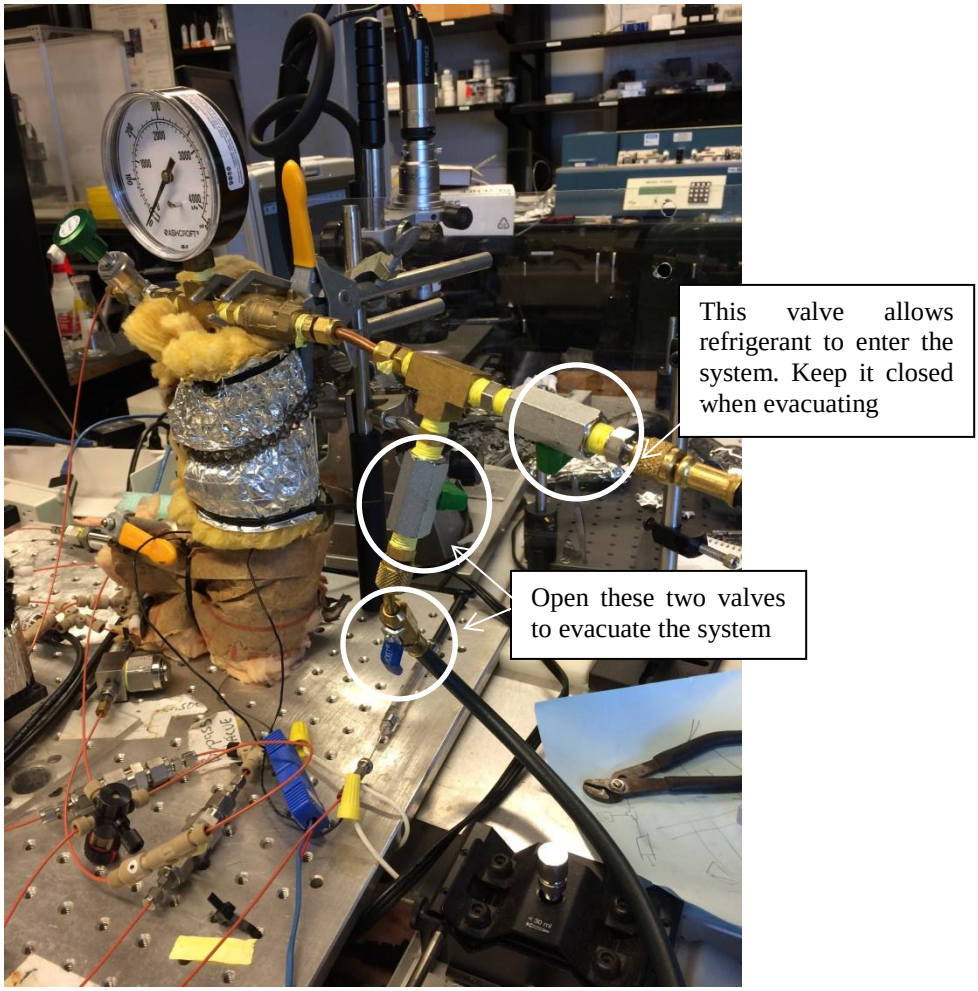

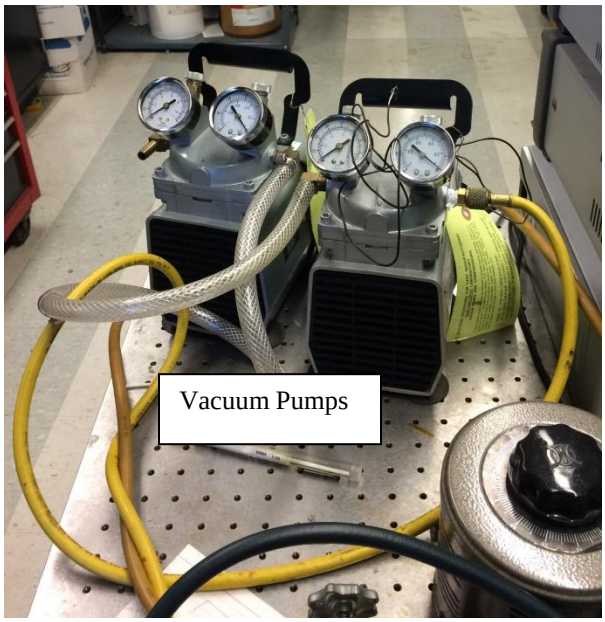

3. Turn on vacuum pumps and monitor pressure transducer reading through DAQ Computer.
4. Inlet and outlet pressure transducer readings should decrease down to at least 40 kPa (absolute) or -60 kPa (gage, which is what pressure transducer reads).
5. Close AV1 once the pressure stops decreasing at the test section. Turn off the vacuum pumps. Make sure the pressure transducers are not recording a rapidly increasing pressure because this would indicate a leak in the system.

F. Charging System

Before charging the system make sure it is evacuated per the instructions in the previous section. Additionally, **make sure AV1 is shut**.

1. Place copper tubing in water bath and freeze. The result should look like the image shown below.

2. Make sure all valves that were opened in step 3 of "Evacuating Experimental system" section are closed. Additionally close T-valves and isolation valve to bypass test section as shown below.

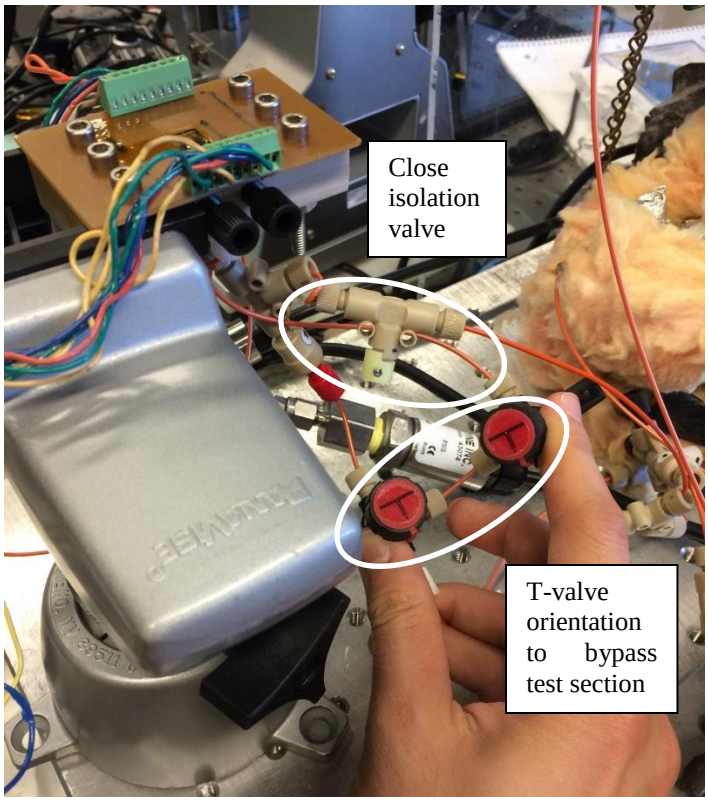

3. Connect one side of the tubing to the accumulator and the other to the r134a tank hose as shown.

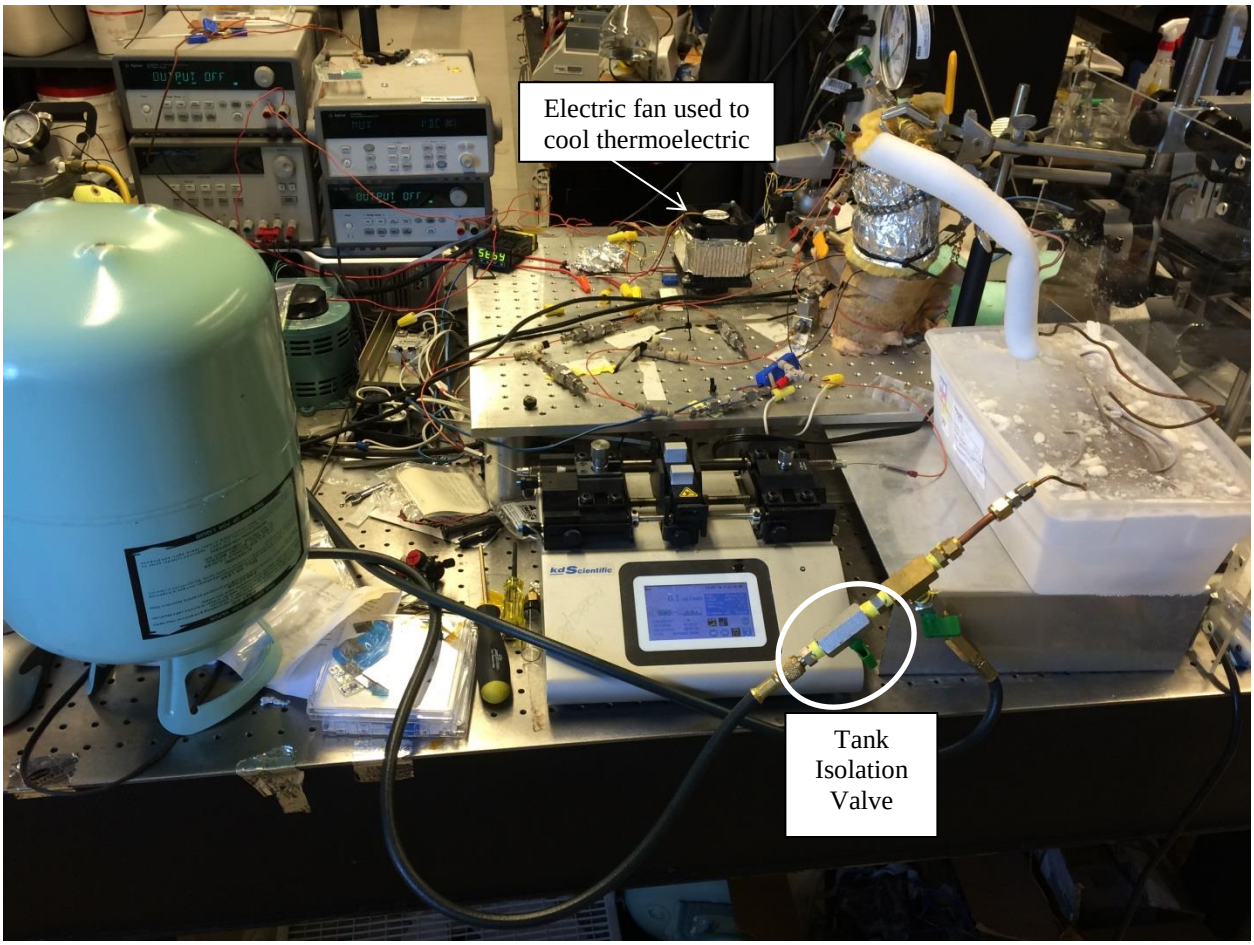

4. Apply +/-6V to the thermoelectric cooler and connect the electric fan power cord to the outlet to turn it on.

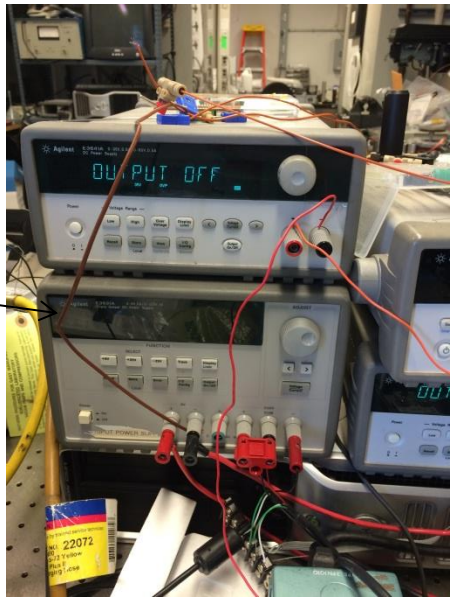

5. Warm r134a tank with heat gun. When the tank feels warm by touch open the tank isolation valve to allow refrigerant to flow through the hosing and copper tubing up to AV1. This takes about 1-2 mn and you should hear the ice crack as refrigerant flows through the copper tubing.
6. Open AV1 and let refrigerant fill the tank. Allow the accumulator to fill until the pressure gage stabilizes in the 600-700 kPa range (should not take more than a few minutes).
7. Close AV1 first then the tank isolation valve.

   Note: You can detach the copper tubing and hosing at any point after the tank isolation valve is shut. Make sure to slowly untighten the tubing to allow refrigerant to leave at a low flow rate. Put the copper tubing in the ice block back into the freezer.
8. Open AV2 and allow refrigerant to flow into the system. Allow pressure to stabilize on the accumulator pressure gauge.
9. Open AV3 to allow refrigerant to fill the syringes. Heat up the accumulator by setting the PID controller to a desired temperature to force liquid refrigerant to fill the system (see controller manual for instructions on interface: http://www.omega.com/pptst/CN8590.html):

   - Quick instructions for programing controller to heat the tank to a set temperature: Hit B2 and when 'SP' flashes use the arrows to set the temperature to the desired set point. Hold B1 for a few seconds and when 'FOP' flashes use the arrows to set the controller to 'Atun' and hit B1 again.

   Choose a temperature of at least 36C for the syringe pump syringes to fill with liquid. I usually set the system to 40C corresponding to an inlet pressure of 820 kPa, the tank temperature will dictate the system pressure and should be chosen accordingly.

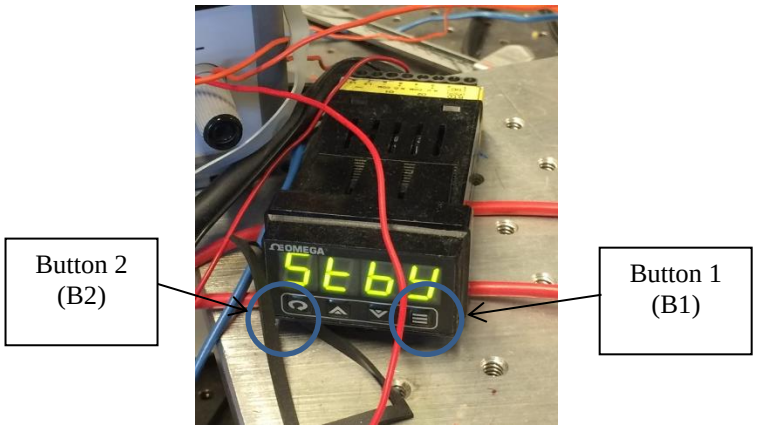

10. The syringes (if made of glass) can be visually inspected to check for liquid filling. The liquid level will rise until the entire syringe is full at which point the system has filled with liquid with the exception of the test section which has been isolated by the 4-way valve.

    If non-transparent syringes are used the system will be full of liquid when the inlet and outlet pressure of the test section reach steady state value (which should both be equal to accumulator pressure).

11. Turn on the Keyence microscope and focus on the microgap test section in the PCB cutout.
12. Valve in the test section by configuring T-valves to allow liquid to flow into the test section (see step 2 of "Leak Test"). Observe the microgap to monitor clogging and monitor the pressure at the chip inlet and outlet with the DAQ. The system will be full of liquid once the pressure at chip inlet and outlet are the same and at the tank pressure. Follow the procedure for "Removing a clog in chip by reverse flow" section if the test section clogs while charging.

G. Running Experiments

1. Input RTD and heater calibrations into the Data logger at corresponding channels as shown.

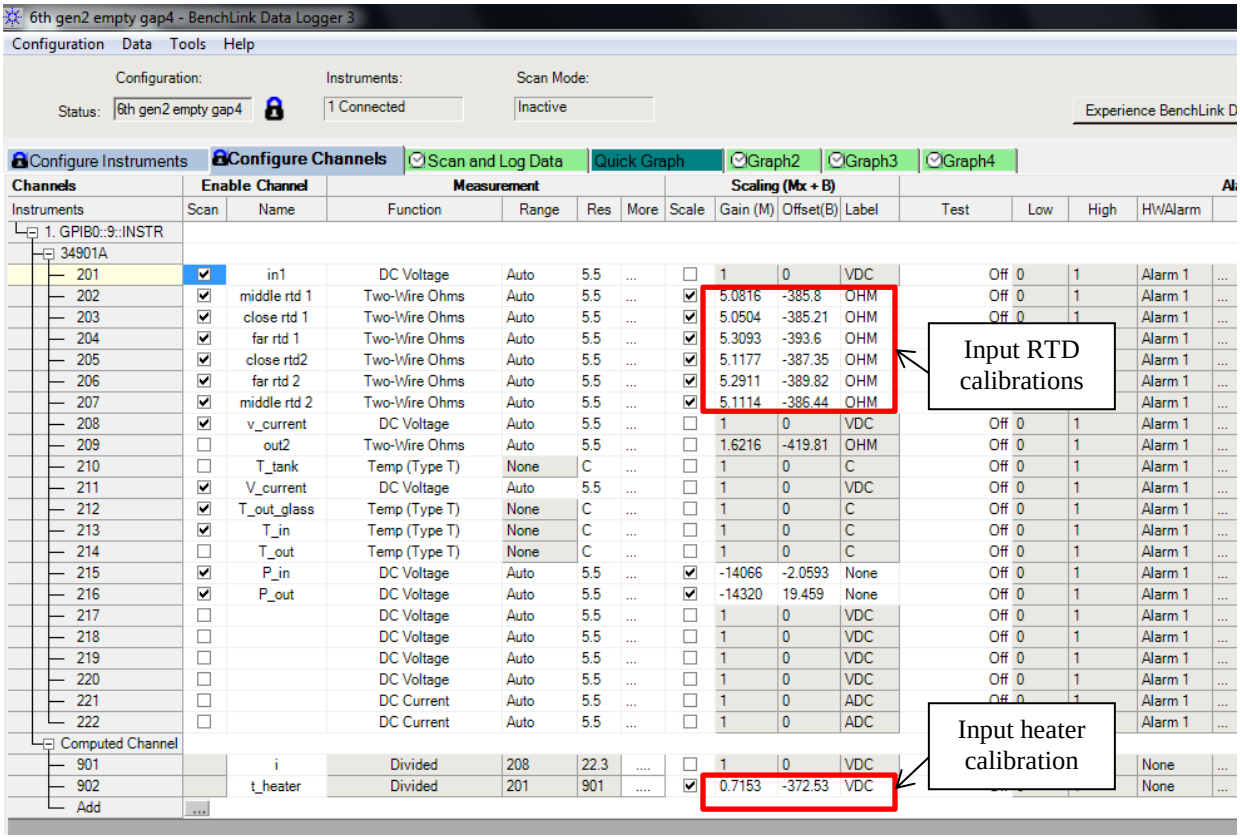

2. Attach power source wires to breadboard (shown in 8-b of "preparing hotspot device" section).
3. Set the syringe pump to the desired flow rate.
4. Configure-valves as shown in step 2 of "leak test section".
5. Turn on pump with valve configuration based on system configuration. Be mindful of infusion time if operating in single syringe setup to ensure heaters are turned off before syringe is out of liquid. Follow steps for infusing and withdrawing in single syringe mode described in "System Configuration Section".

6. Apply 15V to heater with power source and record heater temperature as a calibration point to check for heater degradation.
7. Set heaters to desired heat flux by applying a voltage with the power sources shown below.

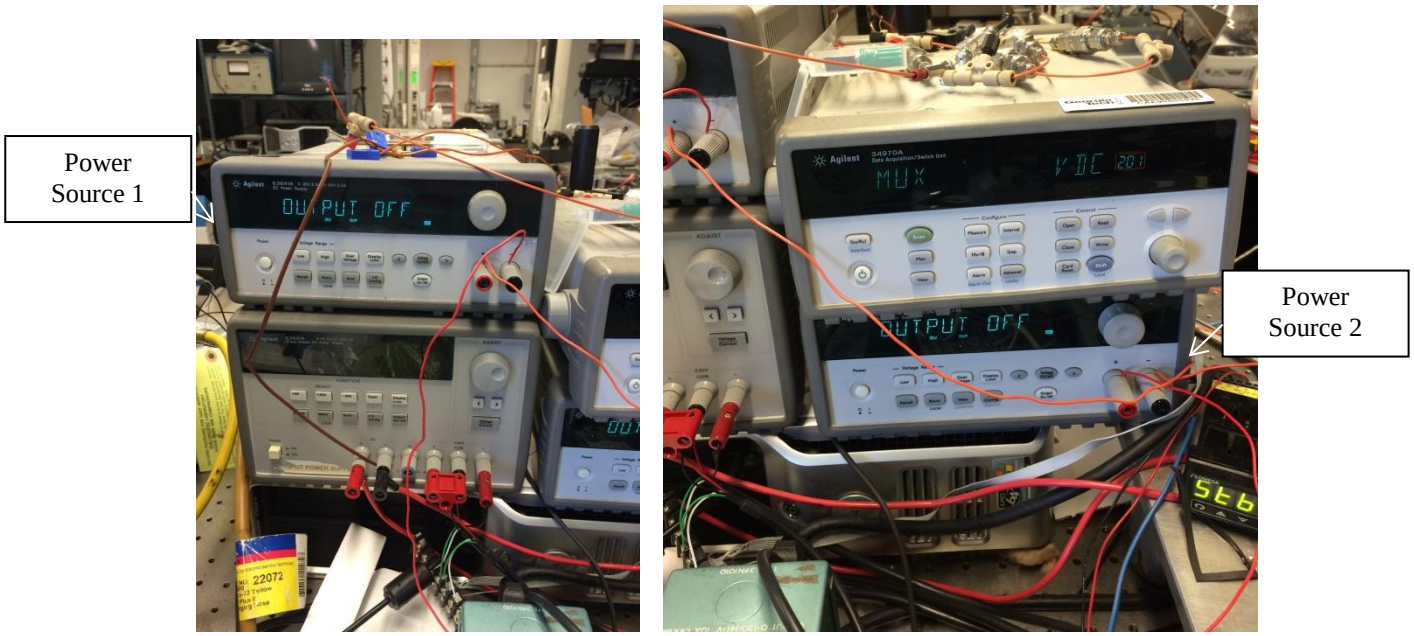

8. The power source displays voltage and current, so heat flux can be approximated based on Power (P=IV) displayed on power source and heater area (200 um x 200um). The two power sources are connected in series and each is able to output 36V. At heat fluxes approaching 5kW/cm2 both power sources need to be operated to produce voltages > 36V. The actual heat flux should be calculated based on the power applied to the heater which is calculated from the current (channel 901 of NIDAQ) and the heater resistance (back calculated with heater calibration from the temperature displayed on channel 902 of NIDAQ).
9. Allow the heater temperature to reach steady state condition before turning off heater by using the "output on/off" button on the power source.

10. Take images with the Keyence or use the video recording computer (shown in “work station” section)
11. Check heater calibration after each heat flux tested to ensure the heater calibration does not drift. Recalibrate heater or change device if the difference in temperature is greater than 2°C. It is recommended to test each mass flux of interest starting at low heat fluxes before moving to higher heat fluxes incase the heater calibration drifts.

H. Removing a clog in chip by reverse flow

If the chip clogs during an experiment, such that a piece of debris blocks the part of the inlet plenum as shown below, use the following procedure to reverse flow in the microchannel and push debris out:

1. Open isolation valve and configure outlet t-valve as shown below to reverse flow in device. Make sure the pump is not actively infusing into the test section before changing valve configuration. Additionally make sure heaters are turned off.

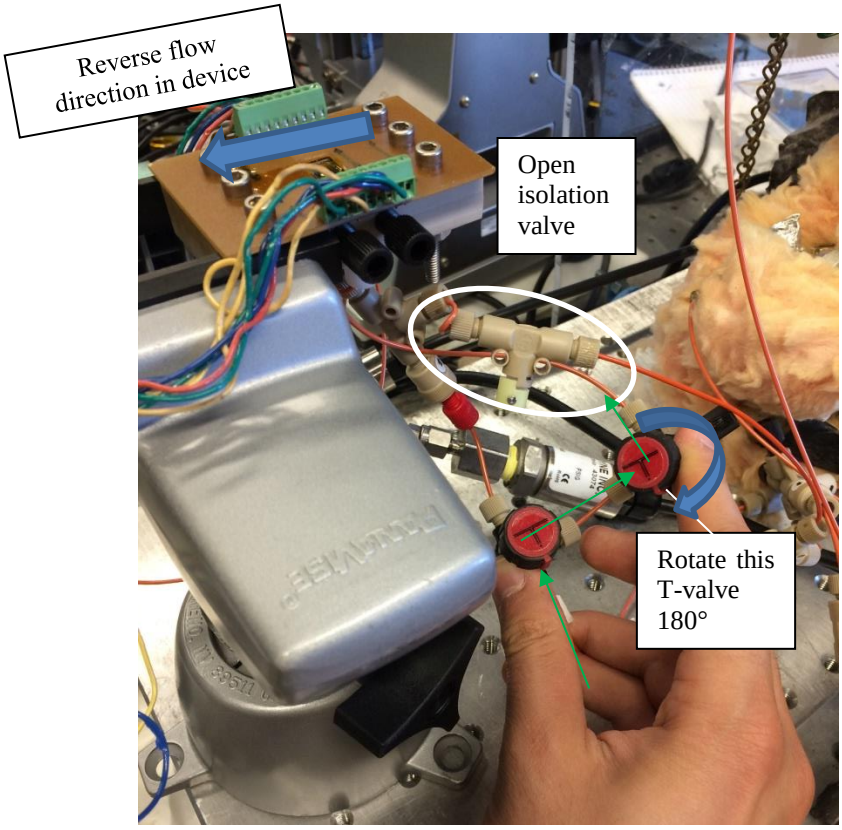

2. Turn on pump starting at a low flow rate (start at 0.1 ml/mn) and observe the microgap with the Keyence. If the debris is not pushed out of the inlet side within a few seconds of turning on the pump, stop the pump and increase the flow rate (increments of 0.1 ml/mn) and start it again. Make sure the pressure reaches steady state condition before increasing pump flow rate. Be careful of clogging on the outlet side due to reverse flow in the

device. If this happens, return the valves to the original flow direction and push out the clog on the outlet side.

I. Package cleaning (<u>follow this procedure on an as-needed basis only</u>)

Note: This procedure can be carried out after the system has been evacuated or after isolating the test section. To Valve out just the test section while keeping the rest of the system charged orient the t-valves as shown below and remove the plug:

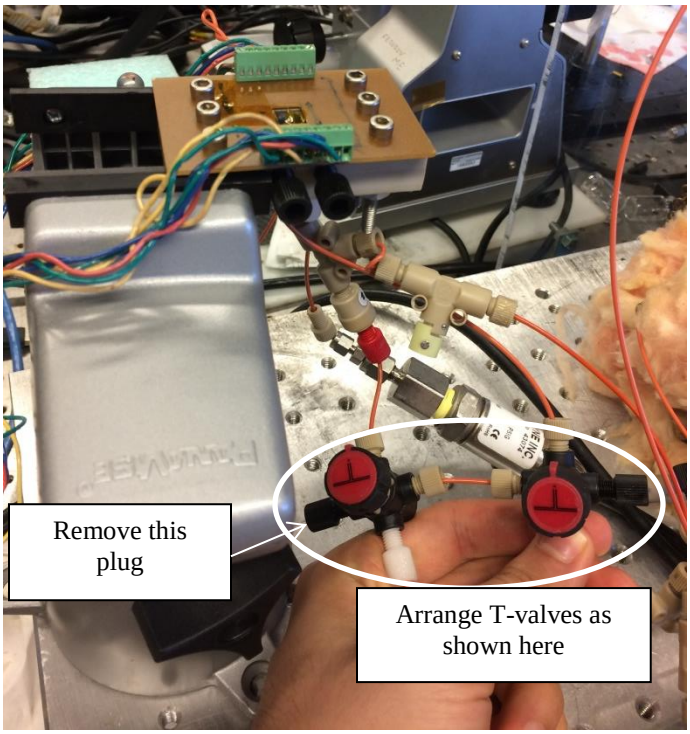

1. If any of the channels where liquid flows in the channel is clogged (i.e. light shined on one side can't be seen from the opposite side) the following steps are recommended:
    a. Blow high pressure air through the clogged channel from different directions until the particulates come out and the channel is clear. Often a pressure of up to 1000 kPa is needed.
    b. Sonicating the package in a solution of soap and water can also be helpful for varying amounts of time depending on extent of clogging.

c. If the above methods don’t work, the fluidic channels should be re-drilled with a high precision mill. It is best to have the machine shop do this to avoid damaging the small diameter channels. It is best to avoid this solution if possible because there is a risk of needing to machine a new package if a channel is damaged. Also machining tends to cause more clogging due to left over chips of PEEK.

J. Engineering Drawings

Gen 2/3 Package (dimensions in inches)

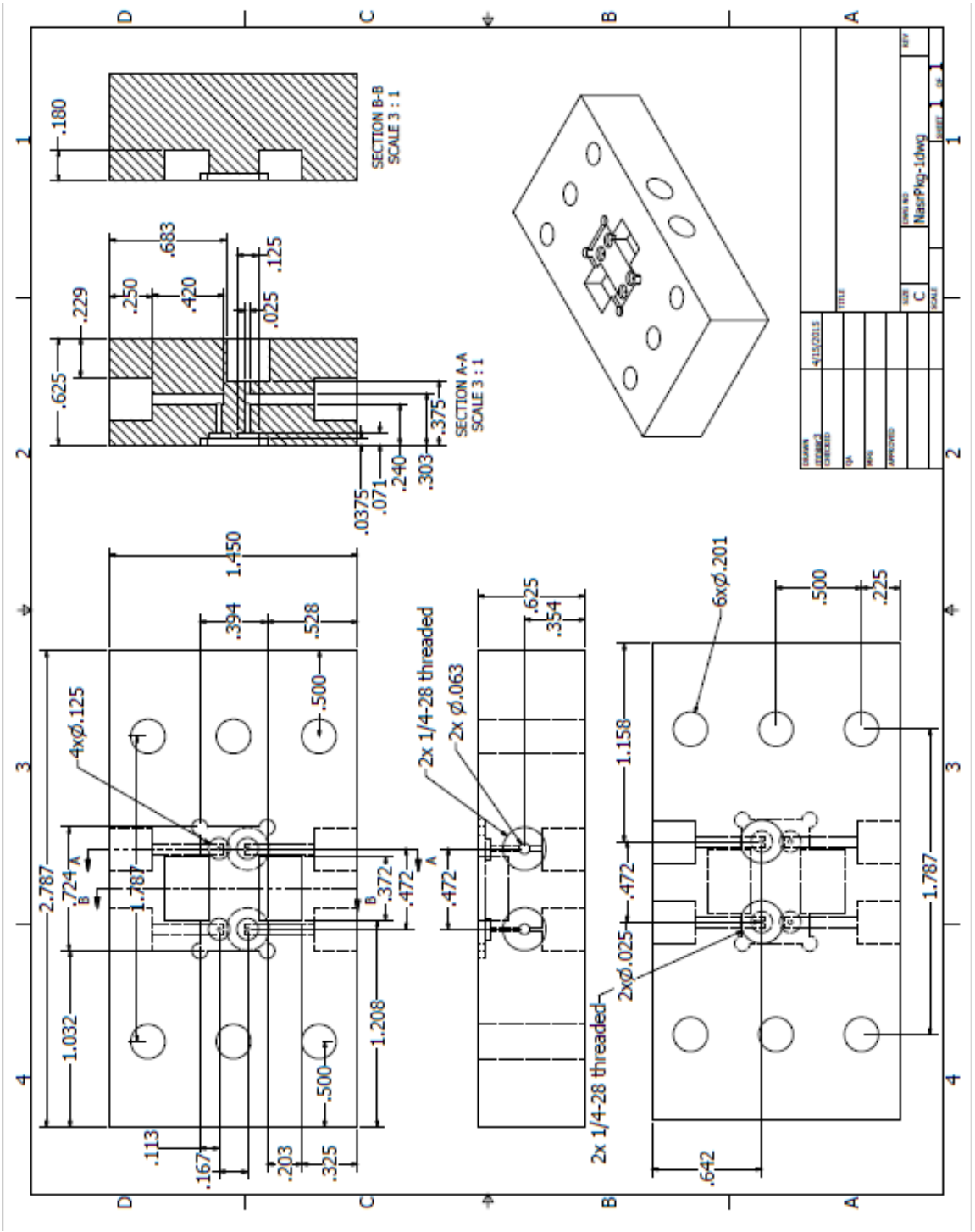

Gen 2/3 package flushing piece (dimensions in inches)

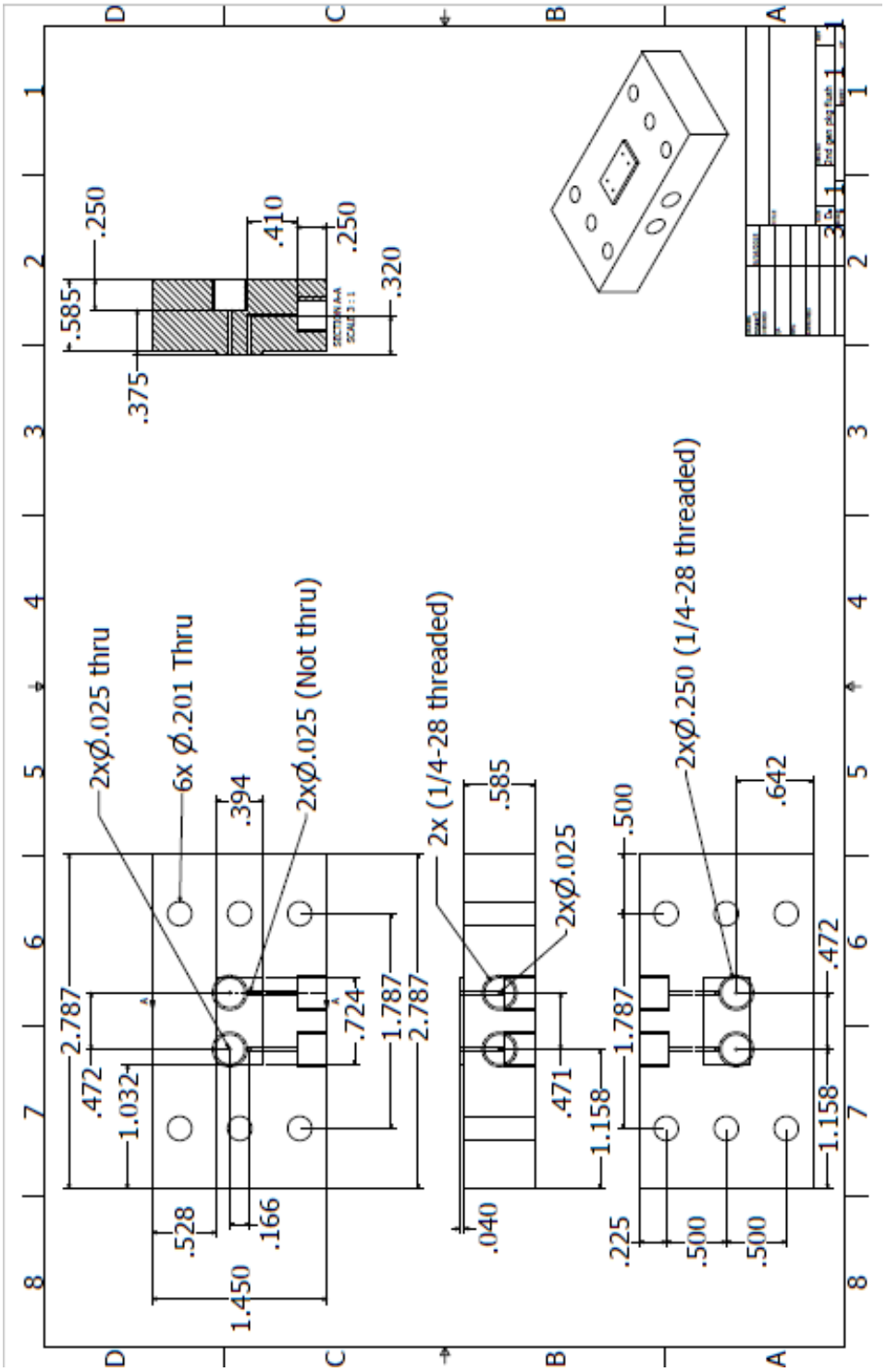

PCB Board (dimensions in meters)

- Drawing corresponds to Gen1 package
- The same design can be used for Gen 2 & Gen 3 device but the cut out in the PCB should be in the middle of the six screw holes. (It is offset from the center in the drawing below to match the holes in the package for Gen 1 devices)

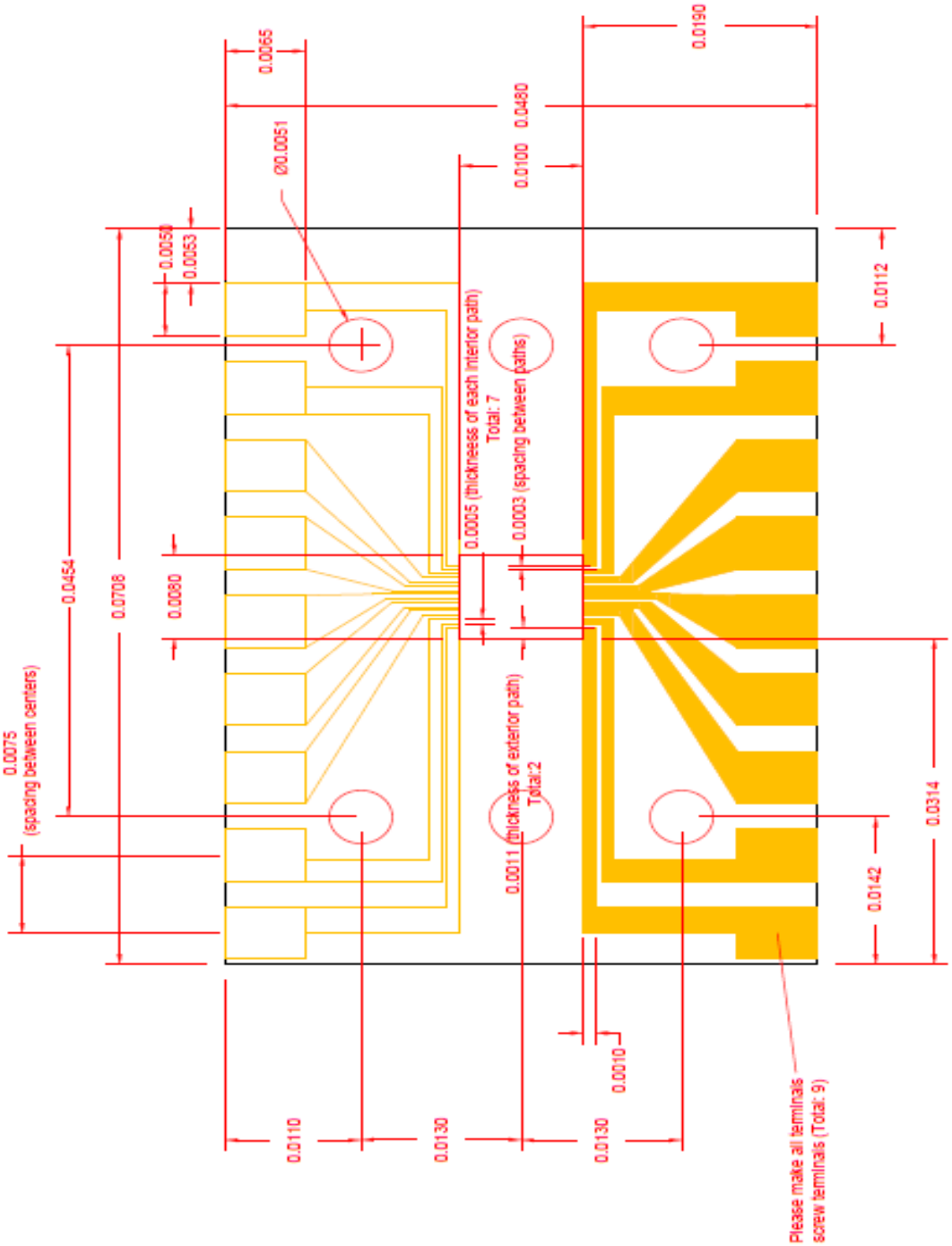

Gen 1 Package (measurments in inches)

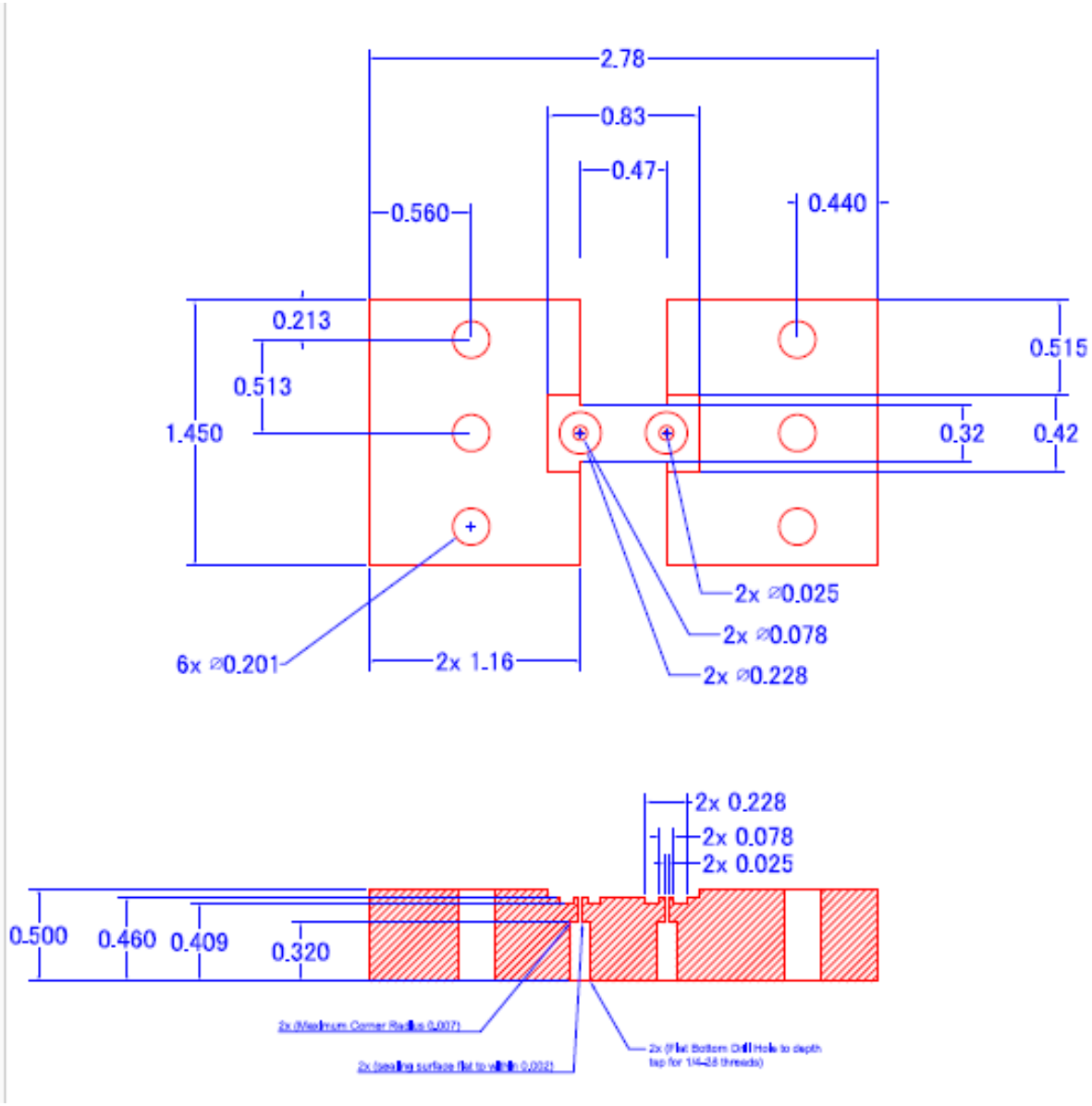

Gen 1 Package flushing piece (measurements in inches)

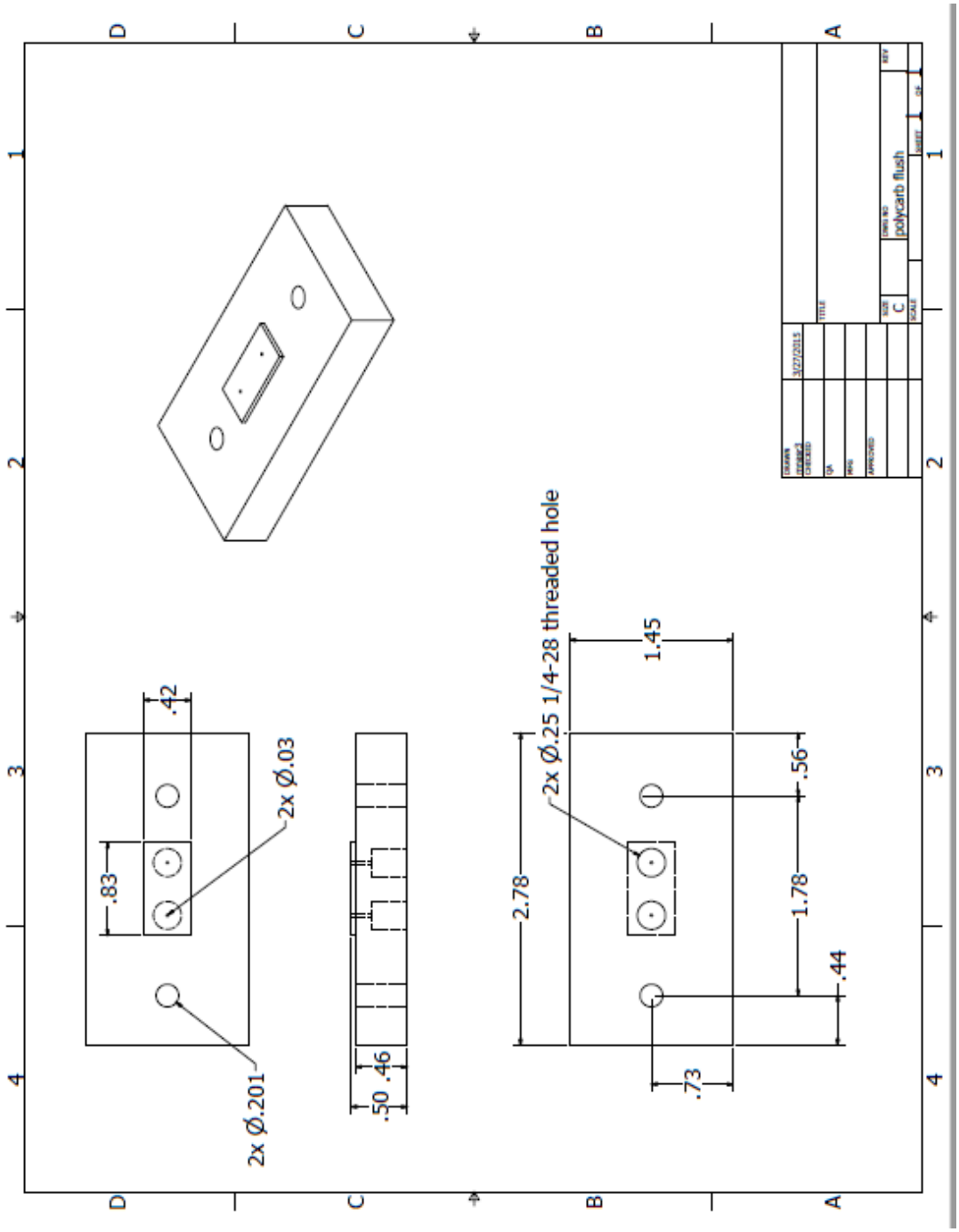

References

[1] Hamann, H. F., Weger, A., Lacey, J. A., Hu, Z., Bose, P., Cohen, E., and Wakil, J., Hotspot-limited microprocessors: Direct temperature and power distribution measurements. *Solid-State Circuits, IEEE Journal of*,*42*(1), 56-65 (2007).

[2] Alam, T., Lee, P. S., Yap, C. R., and Jin, L., Experimental investigation of local flow boiling heat transfer and pressure drop characteristics in microgap channel. *International Journal of Multiphase Flow*, 42, 164-174 (2012).

[3] Tuckerman, D. B., and Pease, R. F. WHigh-performance heat sinking for VLSI. *Electron Device Letters, IEEE*, *2*(5), 126-129 (1981).

[4] Peles, Y., Koşar, A., Mishra, C., Kuo, C. J., & Schneider, B. , Forced convective heat transfer across a pin fin micro heat sink. *International Journal of Heat and Mass Transfer*, *48*(17), 3615-3627 (2005).

[5] Brunschwiler, T., Paredes, S., Drechsler, U., Michel, B., Cesar, W., Töral, G., ... and Leblebici, Y. (2009, September). Validation of the porous-medium approach to model interlayer-cooled 3D-chip stacks. In *3D System Integration, 2009. 3DIC 2009. IEEE International Conference on* (pp. 1-10). IEEE.

[6] Bar-Cohen, A., Sheehan, J. R., and Rahim, E., Two-phase thermal transport in microgap channels—theory, experimental results, and predictive relations. *Microgravity Science and Technology*, 24(1), 1-15 (2012).

[7] Bar-Cohen, A., and Rahim, E., Modeling and prediction of two-phase microgap channel heat transfer characteristics. *Heat Transfer Engineering*, 30(8), 601-625 (2009).

[8] Thome, J. R., and Hajal, J. E., Two-phase flow pattern map for evaporation in horizontal tubes: latest version. *Heat Transfer Engineering*,*24*(6), 3-10 (2003).

[9] Grauso, S., Mastrullo, R., Mauro, A. W., Thome, J. R., and Vanoli, G. P. ,Flow pattern map, heat transfer and pressure drops during evaporation of R-1234ze (E) and R134a in a horizontal, circular smooth tube: Experiments and assessment of predictive methods. *International Journal of Refrigeration*,*36*(2), 478-491 (2013).

[10] Kandlikar, S. G., and Balasubramanian, P. , An extension of the flow boiling correlation to transition, laminar, and deep laminar flows in minichannels and microchannels. *Heat Transfer Engineering*, *25*(3), 86-93 (2004).

[11] Thome, J. R., Dupont, V., and Jacobi, A. M., Heat transfer model for evaporation in microchannels. Part I: presentation of the model. *International Journal of Heat and Mass Transfer*, *47*(14), 3375-3385 (2004).

[12] Kandlikar, S. G., and Grande, W.J., Evolution of Microchannel Flow Passages—Thermohydraulic Performance and Fabrication Technology, *Heat Transfer Engineering*, 25(1), 3–17, (2003).

[13] Mehendale, S.S., and Jacobi, A.M. , Evaporative heat transfer in mesoscale heat exchangers, Transactions-*American Society of Heating Refrigerating and Air Conditioning Engineers*, 106(1), 446-452, (2000).

[14] Bar-Cohen, A., and Rahim, E., Modeling and prediction of two-phase microgap channel heat transfer characteristics. *Heat Transfer Engineering*,*30* (8), 601-625 (2009).

[15] Jacobi, A. M., and Thome, J. R. Heat transfer model for evaporation of elongated bubble flows in microchannels. *Journal of Heat Transfer, 124*(6), 1131-1136 (2002).

[16] Qu, W., and Mudawar, I., Flow boiling heat transfer in two-phase micro-channel heat sinks––I. Experimental investigation and assessment of correlation methods. *International Journal of Heat and Mass Transfer*, *46*(15), 2755-2771 (2003).

[17] Koşar, A., Kuo, C. J., & Peles, Y. , Boiling heat transfer in rectangular microchannels with reentrant cavities. *International Journal of Heat and Mass Transfer*, *48*(23), 4867-4886 (2005).

[18] Lee, J., and Mudawar, I. ,Two-phase flow in high-heat-flux micro-channel heat sink for refrigeration cooling applications: Part II—heat transfer characteristics. *International Journal of Heat and Mass Transfer*, *48*(5), 941-955 (2005).

[19] Chang, K. H., and Pan, C. Two-phase flow instability for boiling in a microchannel heat sink. *International Journal of Heat and Mass Transfer*,*50*(11), 2078-2088 (2007).

[20] Hetsroni, G., Mosyak, A., Pogrebnyak, E., and Segal, Z. , Periodic boiling in parallel micro-channels at low vapor quality. *International Journal of Multiphase Flow*, *32*(10), 1141-1159 (2006).

[21] Kandlikar, S. G., Fundamental issues related to flow boiling in minichannels and microchannels. *Experimental Thermal and Fluid Science*,*26*(2), 389-407 (2002).

[22] Alam, T., Lee, P. S., Yap, C. R., and Jin, L. , A comparative study of flow boiling heat transfer and pressure drop characteristics in microgap and microchannel heat sink and an evaluation of microgap heat sink for hotspot mitigation. *International Journal of Heat and Mass Transfer*, *58*(1), 335-347 (2013).

[23] Rahim, E., and Bar-Cohen, A. (2010, January). Parametric dependence of annular flow heat transfer in microgaps. In *2010 14th International Heat Transfer Conference* (pp. 263-272). American Society of Mechanical Engineers.

[24] Koşar, A., and Peles, Y. ,Boiling heat transfer in a hydrofoil-based micro pin fin heat sink. *International Journal of Heat and Mass Transfer*, *50*(5), 1018-1034 (2007).

[25] Kottke, P. A., Yun, T. M., Green, C., Joshi, Y. K. and Fedorov, A. G., Two-phase convective cooling for ultra-high power dissipation in microprocessors. *ASME Journal of Heat Transfer*, 138 (1), 011501-011507 (2015).

[26] Kabov, O. A., Lyulin, Y. V., Marchuk, I. V., and Zaitsev, D. V., Locally heated shear-driven liquid films in microchannels and minichannels. *International Journal of Heat and Fluid Flow*, 28(1), 103-112 (2007).

[27] Kabov, O. A., Zaitsev, D. V., Cheverda, V. V., and Bar-Cohen, A. ,Evaporation and flow dynamics of thin, shear-driven liquid films in microgap channels. *Experimental Thermal and Fluid Science*, *35*(5), 825-831 (2011).

[28] Gatapova, E. Y., and Kabov, O. A., Shear-driven flows of locally heated liquid films. *International Journal of Heat and Mass Transfer*, 51(19), 4797-4810 (2008).

[29] Craigie, C. J. D., Sheehan, T., Johnson, V. N., Burkett, S. L., Moll, A. J., & Knowlton, W. B. Polymer thickness effects on Bosch etch profiles.*Journal of Vacuum Science and Technology-Section B-Microelectronics Nanometer Structur*, *20*(6), 2229-2232 (2002).

[30] X. Zhang et al, "Design, Microfabrication and Thermal Characterization of the Hotspot Cooler Testbed for Convective Boiling Experiments in Extreme-micro-gap with Integrated Micropin-fins", 15th IEEE I-THERM, Las Vegas, NV, USA, May-June, 2016. (accepted)

[31] Kakaç, S., Vasiliev, L. L., Bayazitoglu, Y., and Yener, Y. (Eds.). (2006).*Microscale Heat Transfer-Fundamentals and Applications: Proceedings of the NATO Advanced Study Institute on Microscale Heat Transfer-Fundamentals and Applications in Biological and Microelectromechanical Systems,* Cesme-Izmir, Turkey, 18-30 July, 2004 (Vol. 193). Springer Science & Business Media.

[32] Alam, T., Lee, P.S., Yap, C.R., Jin, L., Balasubramanian, K., Experimental investigation and flow visualization to determine the optimum dimension range of microgap heat sinks, International Journal of Heat and Mass Transfer, 55, 7623-34 (2012).

[33] Lemmon, E. W., and Jacobsen, R. T. ,Viscosity and thermal conductivity equations for nitrogen, oxygen, argon, and air. *International journal of thermophysics*, *25*(1), 21-69 (2004).

[34] Glassbrenner, C. J., and Slack, G. A. , Thermal conductivity of silicon and germanium from 3 K to the melting point. *Physical Review*, *134*(4A), A1058 (1964).

[35] Chowdhury, I., Prasher, R., Lofgreen, K., Chrysler, G., Narasimhan, S., Mahajan, R., ... and Venkatasubramanian, R. On-chip cooling by superlattice-based thin-film thermoelectrics. *Nature Nanotechnology*, *4*(4), 235-238 (2009).

[36] Gungor, K. E. and Winterton, R. H. S., Simplified general correlation for saturated flow boiling and comparisons of correlations with data. *Chemical Engineering Research & Design*, *65*(2), 148-156 (1987).

[37] Shah, M. M., A New correlation for heat transfer during boiling flow through pipes, *ASHRAE Transactions*, vol. 82, no. 2, pp. 66–86, 1976.

[38] Krishnamurthy, S. and Peles, Y., Flow boiling of water in a circular staggered micro-pin fin heat sink. *International Journal of Heat and Mass Transfer*, *51*(5), 1349-1364 (2008).